Terahertz Spectroscopy of Quantum Spin Liquids

by

Daniel Victor Pilon

Submitted to the Department of Physics
in partial fulfillment of the requirements for the degree of

Doctor of Philosophy

at the

MASSACHUSETTS INSTITUTE OF TECHNOLOGY

June 2016

Author .....
Department of Physics
May 23, 2016

Certified by .....
Nuh Gedik
Associate Professor
Thesis Supervisor

Accepted by .....
Nergis Mavalvala
Associate Department Head for Education

Terahertz Spectroscopy of Quantum Spin Liquids

by

Daniel Victor Pilon

Submitted to the Department of Physics
on May 23, 2016, in partial fulfillment of the
requirements for the degree of
Doctor of Philosophy

Abstract

The optical properties of the spin-1/2 kagome lattice antiferromagnetic Herbertsmithite, $ZnCu_3(OH)_6Cl_2$, are studied by means of Terahertz Time-Domain Spectroscopy. Herbertsmithite is proposed to exhibit Quantum Spin Liquid behavior, in which electron spins have strong antiferromagnetic interactions, but quantum fluctuations inhibit magnetic order even at 0 K, instead giving way to a Resonating Valence Bond state. Quantum Spin Liquids host exotic fractionalized excitations called spinons, which carry spin 1/2 but no charge. The low-energy behavior of these excitations are proposed to be governed by emergent gauge fields that depend on the quantum order of the macroscopically entangled ground state wavefunction. The nature of the quantum order of the ground state in Herbertsmithite has been the subject of great debate in the past decade. While computational work has suggested that a gapped Z_2 spin liquid is realized in Herbertsmithite, experimental work has seen no evidence of a spin gap, suggesting that a U(1) Dirac spin liquid might be realized instead. Recent theory work has proposed that a signature of the quantum order of the ground state of Herbertsmithite is manifested in its low-frequency optical conductivity as a result of the coupling of the charge and spin degrees of freedom through an emergent gauge field. In this dissertation, Terahertz Time-Domain Spectroscopy measurements on single crystals of Herbertsmithite will be used to test these theories, and provide evidence for the existence of a U(1) Dirac spin liquid state in Herbertsmithite.

Thesis Supervisor: Nuh Gedik
Title: Associate Professor

To my parents

Acknowledgments

This thesis would not have been possible without the support of many people. While the persuit of science can be a lonely endeavor at times, it cannot happen without the help and support of colleagues, friends, and family, for whom I will always be grateful.

I would like to begin by thanking my thesis advisor Prof. Nuh Gedik, as well as Prof. Joe Checkelsky and Prof. David Pritchard for serving on my thesis committee. Over the years, Nuh has been a great source of knowledge and of insight into condensed matter physics as well as spectroscopic techniques. With his help, I became more confident in tackling problems that at first glanced seemed insurmountable. Importantly, Nuh also allowed me to persue my own ideas, which, even when an idea did not work out, taught me many valuable lessons on how to be a better scientist.

I would also like to thank the many graduate students and post docs I have had the pleasure of working with in the Gedik group over the years. I would especially like to thank Alex Frenzel, Ozge Ozel, and Joshua Lui for their help and support at all stages of my project. The help of Alex and Ozge was instrumental to the design, construction, optimization, and upkeep of the THz spectroscopy setup used in this thesis, as well as to the understanding of the physics involved in this project. Beyond that, however, their pleasant company made even the most stressful parts of my PhD more bearable. Joshua's help in the writing and refining of my first paper proved invaluable, and was a major contributor to the paper's success. MIT provided me with valuable opportunities to interact with other researchers, most notably Prof. Patrick Lee, Prof. Senthil Todadri, and Drew Potter, who provided valuable theoretical insight into the physics of spin liquids, and who were always willing and eager to answer my questions, no matter how naive they were.

Completing a PhD is, in my opinion, impossible without the support of one's family. My parents Peter and Charlene, my brother Matt, and his wife Kate, were always there to provide a sympathetic ear when things weren't going well, and to celebrate my successes when they worked out. I was fortunate enough to have my

family nearby, which provided me the opportunity to spend the occasional weekend at home to unwind. They have been the one constant during all of my hectic years of education, and for that I am grateful.

Last but certainly not least, I would like to thank all the friends I have made at MIT, as well as those that have stuck with me from earlier in my life, most notably Robin Chisnell, Lucia Marconi, Christina Ignarra, Simon Lee, and Chris Dedrick. I am firm believer in work-life balance, the concept of which sometimes gets thrown out in graduate school. The social outlet they provided on weekends and after work, as well as seeing friendly faces around campus, made my time at MIT that much more enjoyable. Sports have also played an important role in my life at MIT. I want to thank my colleague, friend, and regular squash partner Fahad Mahmood for all of our intense squash matches, as well as keeping me motivated to exercise regularly. Finally, I want to thank all the members of the Annihilation Operators, the physics intramural ice hockey team for which I served as captain for the last few years. I especially want to recognize Axel Schmidt and Brian Henderson, for their tireless effort and enthusiasm while building the team up from one team with barely enough players, to three teams with a full roster of enthusiastic players spanning the full range of ability. Go Hats Go!

Contents

List of Figures

Chapter 1

Frustrated Magnetism and Quantum Spin Liquids

1.1 Introduction

The study of condensed matter physics is the study of the structural, electronic, magnetic, and thermodynamic properties of systems of uncountably many particles, usually arranged in periodic structures called crystals. Despite the complexity of such systems, their electronic behavior can usually be understood by considering a single electron experiencing a potential landscape whose properties are determined by the symmetries that are either conserved or broken by the crystal, along with knowledge of the constituent parts forming the crystal. This approach has led to the Band Theory of Solids, which has been used to very effectively describe the behavior of metals, insulators, and semimetals, among other systems [1, 2].

The single-particle band theory picture breaks down, however, in materials with strong interactions, which often exhibit new and interesting electronic and magnetic phases with collective excitations. These new phases can usually still be understood in terms of phase transitions that break a certain symmetry, with an order parameter that characterizes the new phase. For example, electron-phonon interactions in metals can lead to effective electron-electron attraction resulting in BCS superconductivity that breaks the electromagnetic gauge symmetry and is characterized by

the superconducting gap order parameter [3] whose excitations are a direct analog to the Higgs boson in particle physics [4]. Electron spin interactions can lead to ordered magnetism, which can break the translational and rotational symmetries of the lattice as well as spin-rotation or time-reversal symmetry, and is characterized by the magnetization order parameter [1,2] whose excitations behave as chargeless spin 1 particles called magnons. The ubiquitousness of symmetry breaking in different phases of matter led Landau to develop the Landau Theory of Phase Transitions in the 1940's, in which phase transitions from one state of matter to another are characterized by an order parameter resulting from the spontaneous breaking of a symmetry.

While the Landau Theory of Phase Transitions seems at first glance to be general, it relies on the appearance of a classically observable order parameter to distinguish between phases of matter. This picture broke down in the 1980's with the discovery of the Fractional Quantum Hall Liquid [5,6]. Such a system cannot be understood in terms of classical symmetry breaking, but instead must be understood in terms of the topological order of the electronic wavefunction. Another such example is the Quantum Spin Liquid (QSL). In a QSL, the magnetic ground state breaks no symmetries, but is instead characterized by the quantum order of the ground state wavefunction. QSLs host exotic fractional quasiparticles, whose low-energy excitations are governed by emergent gauge fields resulting from the specific type of quantum order realized. It is the goal of the condensed matter physics community to develop new tools to understand these new kinds of phases of matter, and to experimentally characterize how these phases are realized in real systems. In this thesis, I will present spectroscopic studies of the QSL material Herbertsmithite, with an emphasis on experimentally characterizing the nature of its low-energy excitations.

1.2 Magnetism in insulators

In systems with strong electron-electron interactions, the crossover from metallic to insulating behavior can often be described by the Hubbard model [7], in which electrons are assumed to be localized on crystallographic sites, but are allowed to hop

from site to site and repel other electrons on the same site. The Hubbard model is given by the Hamiltonian

$$\mathscr{H}_{Hubbard} = -t \sum_{<i,j>} (c_i^\dagger c_j + h.c.) + U \sum_i (n_{i\uparrow} n_{i\downarrow}), \tag{1.1}$$

where <i,j> dictates summation over unrepeated pairs of lattice sites (sometimes nearest neighbor only), t is the hopping term, U is the electron-electron repulsion strength, c and $c^\dagger$ are the electron annihilation and creation operators, respectively, h.c. is the hermitian conjugate, and n_i is the electron occupancy on the ith site. In the case of a half-filled band, in the limit of U much greater than the electronic bandwidth W, a metal-insulator transition can occur [8], resulting in a Mott insulating state. In this state, the Hubbard hamiltonian reduces to the Heisenberg spin hamiltonian

$$\mathscr{H}_{Heisenberg} = \sum_{<i,j>} J_{ij} \vec{S}_i \cdot \vec{S}_j, \tag{1.2}$$

where J_{ij} is the site-to-site dependent exchange energy and $\vec{S}$ is the electron spin vector when treated classically, or the spin operator when treated quanum mechanically. In the simplest case, where J_{ij} is isotropic with nearest-neighbor-only interactions, the hamiltonian reduces to

$$\mathscr{H} = J \sum_{<i,j>} \vec{S}_i \cdot \vec{S}_j. \tag{1.3}$$

When J is negative, the system is ferromagnetic, with minimum energy when all spins point in the same direction. When J is positive, the system is antiferromagnetic, with minimum energy when neighboring spins point in the opposite direction.

At high enough temperature, the spin system behaves as a system of weakly interacting paramagnetic spins, or a spin gas (Figure 1.1). The magnetic susceptibility of this state obeys a Curie-Weiss law [1, 2]

$$\chi_m = \frac{C}{T - \Theta_{CW}}, \tag{1.4}$$

where χ_m is the magnetic susceptibility, C is the Curie constant, T is the temperature,

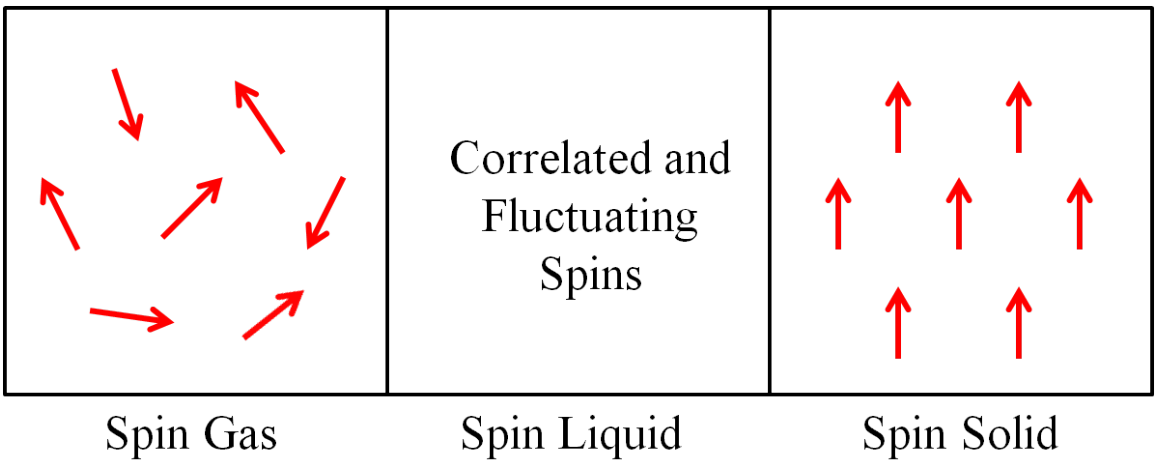

Figure 1.1: The three qualitative types of spin systems. In a spin gas, spin are randomly oriented and uncorrelated, behaving paramagnetically. In a spin liquid, spins are correlated, but fluctuate and form no static order. In a spin solid, spins align in a fixed pattern.

and Θ_{CW} is the Curie-Weiss temperature. In ferromagnetic systems, Θ_{CW} is positive, and therefore the magnetic susceptibility diverges at $T = \Theta_{CW}$, resulting in a phase transition to a ferromagnetically ordered state. In antiferromagnetic systems, Θ_{CW} is negative, and a phase transition to an antiferromagnetically ordered state is expected at temperatures comparable to $|\Theta_{CW}|$. At intermediate temperatures, the spins behave as a Classical Spin Liquid (Figure 1.1), in which strong spin-spin correlations exist, but no long-range spin order is present, resulting in a failure of the Curie-Weiss behavior at temperatures below around $2|\Theta_{CW}|$ [9]. Later in this chapter, we will discuss a state called a Quantum Spin Liquid (QSL), where quantum fluctuations result in a highly degenerate, fluctuating magnetic ground state with strong correlations, even at zero temperature.

1.3 Frustrated magnetism

A frustrated magnetic system is defined to be a magnetic system in which no spin configuration can simultaneously satisfy all magnetic interactions [10]. Magnetic frustration can arise from many different sources. First, competition between ferro-

magnetic nearest-neighbor interactions and antiferromagnetic next-nearest-neighbor interactions can lead to unusual magnetically ordered states, such as helical or screw-type magnetic states [11, 12]. Lattice disorder can also lead to magnetic frustration, such as in spin glasses [13, 14]. Finally, magnetic frustration can arise from geometric frustration, in which the geometry of the lattice does not allow all antiferromagnetic interactions to be satisfied. In general, a geometrically frustrated lattice is a lattice in which there exists more than two equidistant nearest neighbors in each lattice plaquette (Figure 1.2). We will focus on geometric frustration for the remainder of this chapter.

1.3.1 Geometric frustration

Figure 1.2 shows examples of unfrustrated and frustrated lattices in two dimensions. In the case of a simple square lattice with antiferromagnetic interactions (Figure 1.2a), all spins can align opposite to their nearest neighbors, resulting in a minimized energy of $-JS^2$ per bond. In this case, the lattice is unfrustrated. The simplest frustrated lattice in two dimensions is the triangular lattice, shown in Figure 1.2b,c. In the case of antiferromagnetically interacting Ising spins on the triangular lattice (Figure 1.2b), the lowest energy configuration is that in which two pairs of spins satisfy the antiferromagnetic condition, while the remaining pair of spins violates it [15]. This results in an average binding energy of $-\frac{1}{3}JS^2$ per bond, three times lower than for the unfrustrated case. This frustration can be partially lifted, however, by allowing the spins to point in any direction (Heisenberg or XY model), in which case the energy is minimized by each spin forming a 120° angle with its nearest neighbors (Figure 1.2c). This configuration results in an average binding energy of $-\frac{1}{2}JS^2$ per bond.

It is evident from Figure 1.2 that the antiferromagnetic Ising model on frustrated lattices leads to an extremely large ground state degeneracy. On the triangular lattice (Figure 2.3a), there are three choices of bonds where the antiferromagnetic condition is broken for each triangular plaquette, with each case having the same energy. Therefore, there is not a single ground state with a single arrangement of spins, but rather

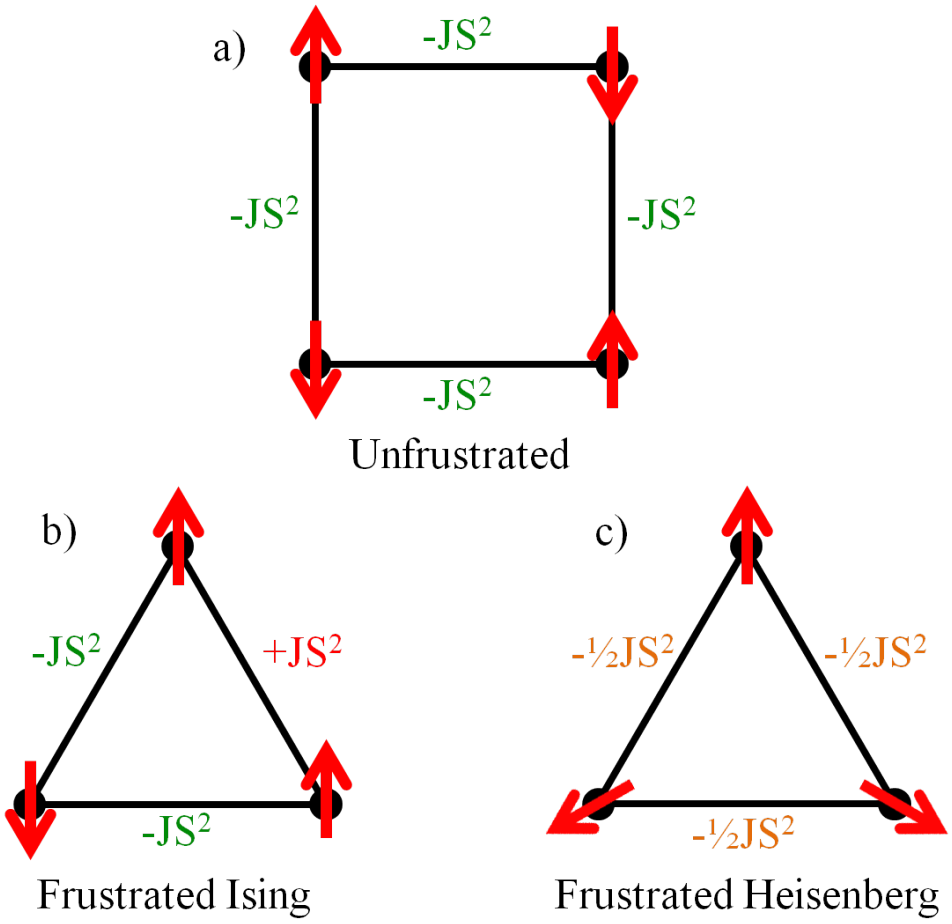

Figure 1.2: Geometric frustration on a crystal lattice. a) On a square lattice, all spins can satisfy the antiferromagnetic condition, minimizing the energy. b) On a triangular Ising lattice, only two of three pairs of spins can satisfy the antiferromagnetic condition. c) Allowing the spins to rotate freely (Heisenberg model) partially relieves the geometric frustration.

a massive number of degenerate ground states, whose number scales exponentially with the system size. Such a system was studied by Wannier in 1950 [16], in which he found there to be a ground state entropy of 0.323 k_B per spin, where k_B is the Boltzmann constant. Indeed such a macroscopic ground state degeneracy is a hallmark of geometrically frustrated systems. On the Ising kagome lattice (Figure 2.3b), which is composed of corner sharing triangles, numerical studies found the ground state entropy to be 0.5 k_B per spin [17].

Another property of geometrically frustrated antiferromagnetic systems is a re-

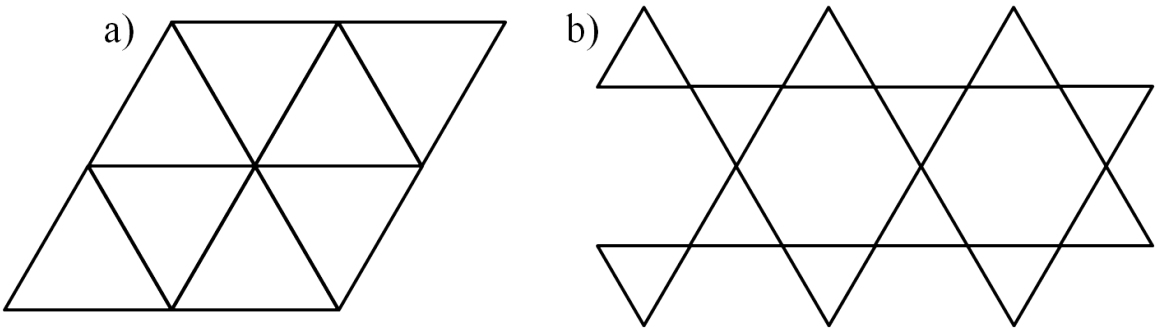

Figure 1.3: Examples of frustrated lattices in two dimensions. a) The Ising triangular lattice has ground state entropy $0.323\mathrm{Nk}_B$. b) The Ising kagome lattice (corner-sharing triangles) is more frustrated with a ground state entropy of $0.5\mathrm{Nk}_B$.

duction in their ordering temperature (Néel temperature). While in unfrustrated magnets it is expected that magnetic ordering will occur at temperatures comparable to $|\Theta_{CW}|$, geometric frustration can significantly lower this ordering temperature. Because of this, Ramirez suggested to use a measure (f) of this reduced ordering temperature as a measure of frustration itself [10].

$$f \equiv \frac{|\Theta_{CW}|}{T_N}, \tag{1.5}$$

where T_N is the Néel temperature. By convention, a material is considered highly frustrated if $f > 10$, but for some materials, f can exceed a value of hundreds or even thousands [18]. Furthermore, geometric frustration can result in paramagnetic behavior persisting to much lower temperatures. In unfrustrated magnets, paramagnetic behavior ($^1/_{\chi_m} \propto T$) fails at around $2|\Theta_{CW}|$ when the magnetic correlation length becomes comparable to the spin separation distance and spin-spin interactions become significant. In frustrated systems, however, paramagnetic behavior can persist down to fractions of $|\Theta_{CW}|$. This shows that, despite the presence of interactions with energy scale much larger than the temperature, spins in frustrated systems can act as effectively free spins.

1.3.2 The effects of dimensionality

We have so far only discussed classical magnetic order, in which spins behave as well-defined vectors. An alternative to classical antiferromagnetism, however, is the formation of singlet dimers, in which pairs of spins form a superposition of $|\uparrow\downarrow>$ and $|\downarrow\uparrow>$, with a spin expectation value of 0 on each site. Consider the simplest unfrustrated lattice in 1, 2 and 3 dimensions, i.e. the linear chain, square, and cubic lattices. In the case of Néel order, the binding energy per pair of spins is given by $-JS^2$ times the number of nearest neighbors per spin. The binding energy per spin is therefore half of this value. The binding energy per spin in these three cases is $-JS^2$, $-2JS^2$ and $-3JS^2$, respectively. The increased binding energy with higher dimensionality can be intuitively understood by considering flipping one spin. In higher dimension, one flipped spin results in more violations of the antiferromagnetic condition than in lower dimension.

Now consider the formation of singlet dimers instead of Néel order. The per-bond binding energy $J\vec{S}_1 \cdot \vec{S}_2$ must be treated as a quantum mechanical operator instead of a classical vector dot product. For a singlet,

$$J\vec{S}_1 \cdot \vec{S}_2 = \frac{1}{2}J((S_1 + S_2)^2 - S_1^2 - S_2^2) = -\frac{1}{2}J(S_1^2 + S_2^2). \tag{1.6}$$

When $|S_1| = |S_2|$, formula 1.6 reduces to $-JS^2$, which has an eigenvalue of $-JS(S+1)$ [19]. The binding energy per spin for a singlet is therefore $-\frac{1}{2}JS(S+1)$. This value is independent of dimensionality, since the expectation value of the spin on each site is 0, and therefore there is no dipolar interaction between neighboring singlets, regardless of how many there are. There is therefore a crossover between Néel order and singlet formation as dimensionality is lowered, when $\frac{1}{2}JS(S+1) > DJS^2$, where D is the dimensionality of the lattice. In the case of $D = 1$ and $S = 1/2$, singlet formation is preferred with a binding energy of $-\frac{3}{8}J$ per spin, compared to $-\frac{1}{4}J$ per spin for Néel order.

The 1D quantum mechanical spin 1/2 chain can be solved exactly and will prove to be a very useful example for understanding Quantum Spin Liquids in two dimensions.

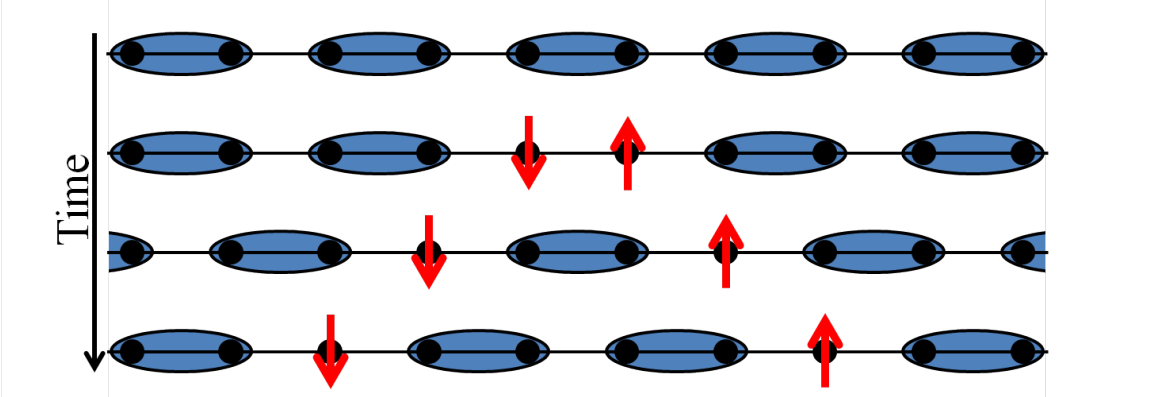

Figure 1.4: Visual representation of spinons in a 1D chain. The system begins as a superposition of singlet dimers (blue ovals) with all spins paired. Only one arrangement of dimers is shown for simplicity. One singlet is excited to form two antialigned spins. These two spins are free to move away from each other due to the fluctuating nature of the singlet dimer pairings. Each of these two spins acts as a spin ½ excitation with no charge.

This system was solved exactly by Hulthén in 1938 using a Bethe ansatz [20]. He found that the ground state had a binding energy of $-0.443J$ per spin, a value lower than both $-\frac{3}{8}J$ for nearest neighbor singlet formation and $-\frac{1}{4}J$ for Néel order. Rather than a fixed arrangment of singlet dimers, the ground state is a macroscopic superposition of singlet pairings, with pairs not being limited to nearest neighbors. This state is known as a one dimensional Quantum Spin Liquid (QSL), and hosts a variety of novel properties. First, it breaks no additional symmetries, unlike Néel order, which breaks the rotational and translational symmetry of the underlying lattice and spin rotation symmetry. Second, it hosts exotic fractional quasiparticle excitations that carry $s = 1/2$ but no charge, called spinons [21]. Figure 1.4 shows a schematic representation of these spinons. They are created in pairs corresponding to the breaking of one singlet into two anti-aligned spins, and are gapless in this case [22]. Each spinon behaves as an independent excitation because they are free to dissociate from each other without costing energy, due to the fluctuating nature of the ground state singlet distribution.

1.4 Quantum Spin Liquids in two dimensions

While the one-dimensional unfrustrated spin 1/2 chain can be solved exactly, the two-dimensional case will be quite different. From our naive estimates on the square lattice, Néel order should be energetically favorable over singlet formation, with a binding energy of $-\frac{1}{2}J$ and $-\frac{3}{8}J$ per spin, respectively. A more rigorous treatment, however, known as the Mermin-Wagner theorem [23], has proven that neither ferromagnetic nor antiferromagnetic order is possible in two dimensions at finite temperature if the spin-spin correlations have finite length. The question remains, therefore, whether two-dimensional systems, especially two-dimensional frustrated systems, can host a 2D analog of the QSL found in 1D.

1.4.1 The Resonating Valence Bond State

While the Mermin-Wagner theorem suggests a ground state involving singlet dimers over Néel order, there are still a large number of possible ground states. The simplest example is called the Valence Bond Crystal (VBC) state [24–30]. In the VBC state, each spin forms a singlet dimer with another spin, forming a static pattern of singlets with periodic long range order, but only short-range spin-spin correlations. Such a state is not a QSL, since the singlet periodicity breaks the underlying crystal translational and rotational symmetries, and it does not host fractional excitations. If you consider the excitation of a singlet to two anti-aligned spins, these spins are not independently free to travel away from each other as in the 1D QSL case. In order for these excited spins to move, more singlets must be broken, which requires energy. Another possible ground state is the Valence Bond Glass (VBG) state [31]. In the VBG state, spins again form a static pattern of singlet dimers with short range correlations, but this pattern has no long range periodicity or order.

An alternative to static dimer order called the Resonating Valence Bond (RVB) state was proposed by Anderson [32, 33]. In the RVB state, rather than forming a single arrangement of singlet dimers, the spins form a superposition of all possible dimer pairings, weighted by the pairing's relative probability depending on the sepa-

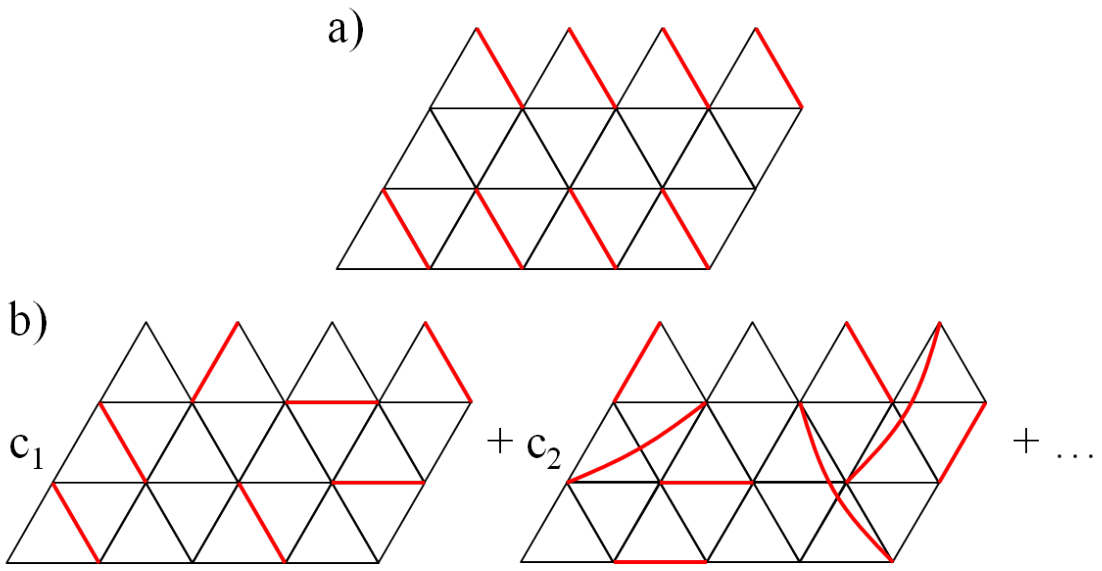

Figure 1.5: a) An example of a Valence Bond Crystal (VBC) state on a triangular lattice. All spins form a fixed arrangment of singlets (red lines). b) An example of a Resonating Valence Bond (RVB) state. The spins form a superposition of all possible singlet pairings. The properties of a specific RVB state depend on the relative weights c_i of the superposition. Singlets formed by spins separated by any distance are in general allowed.

ration distance-dependence of the spin-spin correlations. In all cases, the RVB state supports fractional spinon excitations, since, as in one dimension, two spins formed by a broken singlet are free to move through the fluctuating sea of dimers without energy cost. If realized, the RVB state would be a true manifestation of a QSL in two dimensions, since it breaks no local or global symmetries, has no local or global average magnetization, and hosts fractional excitations. Fractional spinon excitations will be the experimental smoking gun of the RVB state, as will be discussed later in this chapter as it pertains to kagome lattice Herbertsmithite. Since spinons are created in pairs, energy and momentum conservation are satisfied by a continuum of spinon energies and momenta, rather than a single dispersion relation. Deconfined spinon excitations therefore give rise to a scattering continuum in neutron scattering measurements, rather than well-defined peaks [34]. Figure 1.5 shows an example of the RVB state versus the VBC state on the triangular lattice.

1.4.2 Plethora of RVB ground states

The low energy physics of the RVB state sensitively depends on the details of the macroscopic superposition of singlet dimer patterns. The lowest energy excitations of the RVB state are spin 0 excitations where a singlet is excited to form two antialigned spins, and a spin 1 excitation where a singlet is excited to form a triplet. The dispersion of these excitations will depend strongly on how the probability of a specific dimer configuration depends on the dimer separation distance. For instance, in the case where the probability of singlet formation falls off exponentionally with distance, with length scale on the order of the nearest neighbor distance (Type I short-range RVB), the ground state will be dominated by dimer patterns involving only nearest-neighbor singlets. In this case, the singlet and triplet excitation spectra will be gapped, with a gap energy comparable to the energy cost of exciting one nearest-neighbor singlet [9]. In the case where spin correlations decay exponentionally with a length scale that is large compared to the unit cell size (Type II short-range RVB), the ground state will be composed of a greater number of singlet pairings that are far apart. In this case, the singlet excitations will be gapless, but the triplet excitations will be gapped [9]. Additionally, these short-range RVB states are predicted to host certain kinds of topological order [35–38].

RVB spin correlations can have spatial dependence other than exponential, namely algebraic (power law) dependence (long-range RVB). In this case, the ground state can be heavily dominated by singlet dimers where the spins are separated by large distances, and both the singlet and triplet excitations will be gapless [39]. In general, the properties of a given QSL state are governed by the underlying gauge symmetry of the ground state wavefunction. Some of these long-range RVB states, specifically the U(1) Dirac spin liquid state, can host emergent gauge fields that govern the low energy dissipation in the system [40, 41].

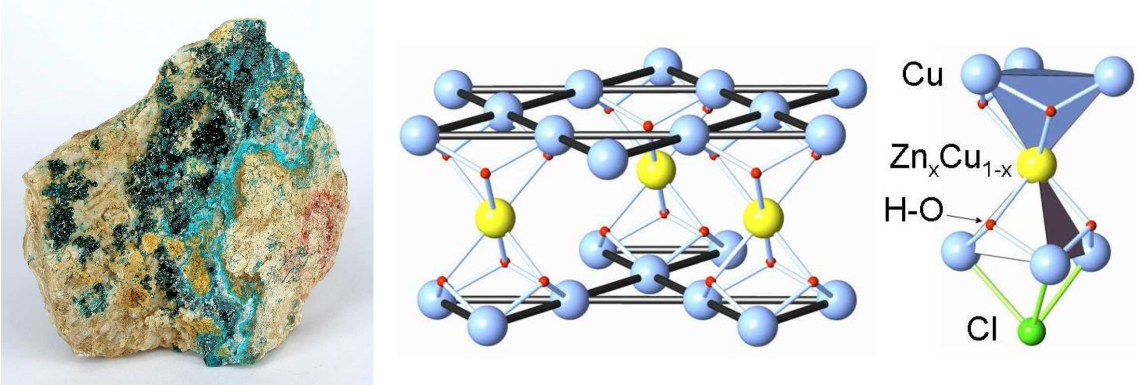

Figure 1.6: The crystal structure of Herbertsmithite. Herbertsmithite ($ZnCu_3(OH)_6Cl_2$) is a naturally occurring mineral, though natural samples are too impure for the purposes of this work. Herbertsmithite has a trigonal structure composed of kagome planes of $S = 1/2$ Cu^{2+} ions separated by nonmagnetic Zn^{2+} ions. Superexchange through the OH chains that link the Cu atoms within the kagome planes is responsible for the antiferromagnetic interactions of the Cu atoms. [56]

1.5 Herbertsmithite

Up to this point, we have discussed the theoretical possibility of a QSL state on 1D or 2D lattices. There are a number of real systems, however, that show promise in the realization of QSL physics. Among these are the triangular-lattice organic salts $EtMe_3Sb[Pd(dmit)_2]_2$ [42, 43] and κ-$(BEDT\text{-}TTF)_2Cu_2(CN)_3$ [44–46], as well as the kagome-lattice mineral $ZnCu_3(OH)_6Cl_2$ (also called Herbertsmithite) [18, 34, 47–55]. In each of these systems, two-dimensional frustrated planes of atoms carrying spin-1/2 are separated by nonmagnetic atoms, resulting in an effectively two-dimensional spin system. The focus of this dissertation will be on kagome-lattice Herbertsmithite.

Herbertsmithite is composed of planes of Cu^{2+} ions carrying spin-1/2 and forming a kagome pattern, separated by nonmagnetic Zn atoms. The Cu atoms are connected by OH chains that sit slightly out of the kagome plane. The crystal structure can be seen in Figure 1.6. The trigonal symmetry of the crystal structure ensures that the in-plane exchange interactions are isotropic, making Herbertsmithite a structurally perfect kagome system [56]. Exchange between the copper atoms occurs via superexchange through the OH chains, resulting in a strong antiferromagnetic interaction with exchange energy $J \approx 17\ meV$, a Curie-Weiss temperature $\Theta_{CW} = -300\ K$, and

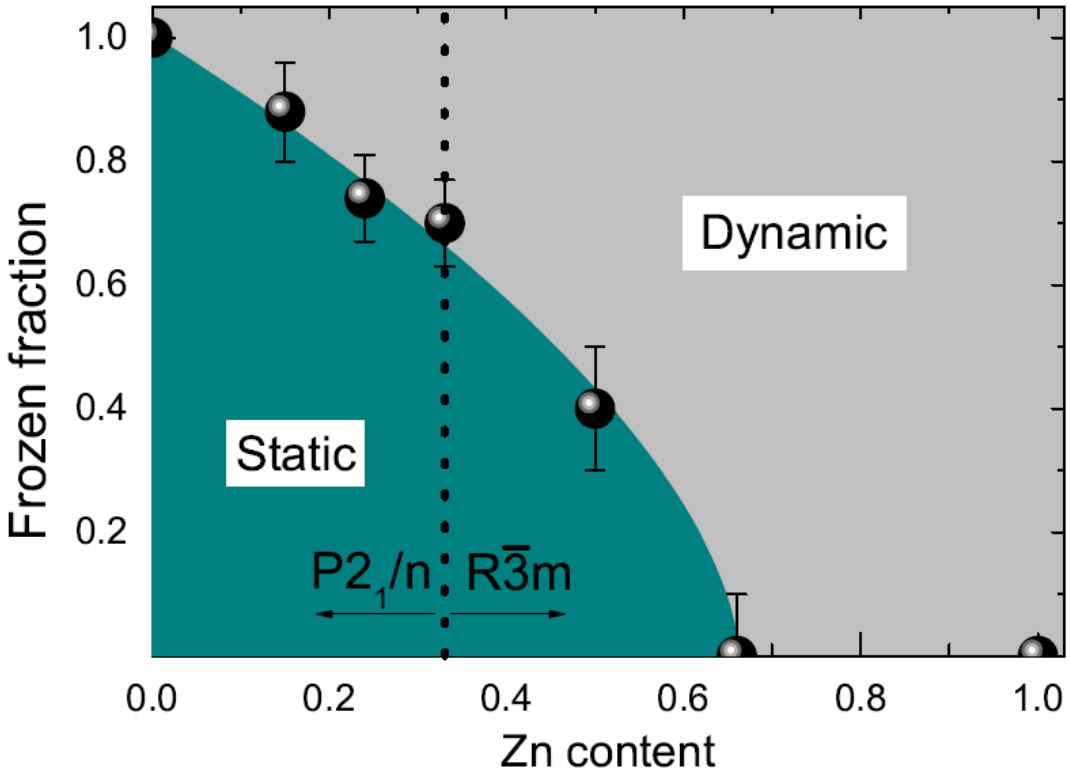

Figure 1.7: μSR phase diagram for the Zn-paratacamite family ($Zn_xCu_{4-x}(OH)_6Cl_2$) taken at 1 K from reference [56]. Magnetic order is not observed for sufficiently high values of x. As x is decreased, the two-dimensionality of the spin system breaks down, resulting in magnetic order below $x = 0.65$. At $x = 0.3$, a structural phase transition occurs due to Jahn-Teller distortion.

a Dzyaloshinskii-Moriya (DM) interaction strength of ~$0.1J$ [18]. Herbertsmithite is also a strong Mott insulator with charge gap ~1 eV.

Herbertsmithite is the end point in the Zn-paratacamite family of materials, given by the chemical formula $Zn_xCu_{4-x}(OH)_6Cl_2$, where x is the percentage of zinc (replacing copper) at the interlayer sites [56]. The presence of magnetic Cu atoms in the Zn sites breaks the two-dimensionality of the spin system, eventually leading to magnetic order for $x <$ ~0.65 and a structural phase transition driven by Jahn-Teller distortion at $x \approx 0.3$. As will be discussed futher in chapter 4, the single-crystal growth of Herbertsmithite results in a deviation from $x = 1$ by ~15% [53], meaning 15% of the Zn sites are replaced by magnetic copper atoms. This will have unfortunate consequences

in thermodynamic and scattering measurements at low temperature and energy, but the deviation is too small to result in magnetic order at low temperature, as can be seen in the phase diagram from μSR data in Figure 1.7.

1.5.1 The ground state of Herbertsmithite

Other than the previously mentioned Cu substitution defects, Herbertsmithite is the perfect system for the realization of a QSL state on the 2D kagome lattice. Thermodynamic measurements (Figure 1.8) show no phase transitions, structural, magnetic, or otherwise, below 30 K, evidenced by the lack of peaks in the specific heat [18]. The magnetic susceptibility shows paramagnetic behavior above 100 K, with deviation from this behavior below 100 K due to the Cu defects, but no antiferromagnetic or ferromagnetic ordering is observed down to at least 50 mK [18]. This lack of magnetic order down to 50 mK corresponds to a frustration factor of $f > 6000$. Furthermore, inelastic neutron scattering measurements on powder samples of Herbertsmithite reveal a spectrum of low-energy spin excitations with no evidence of a spin gap down to 0.1 meV and with seemingly no dependence on the momentum transfer $|\vec{Q}|$, consistent with a scattering continuum resulting from the two-particle spinon creation process [18].

1.5.2 Neutron scattering measurements on single crystal Herbertsmithite

The smoking-gun experiment to confirm the RVB state and hence QSL behavior in Herbertsmithite is the observation of the spinon scattering continuum. Such a scattering continuum is direct evidence for the fluctuating nature of the RVB ground state, as opposed to any form of VBC involving static arrangements of singlets. While the powder neutron scattering measurements are consistent with this scattering continuum, the angle-integrated nature of these measurements makes it difficult to compare with theory in a detailed manner. It was not until a recent breakthrough in the growth of large sample-size single crystal Herbertsmithite [57] that single-crystal

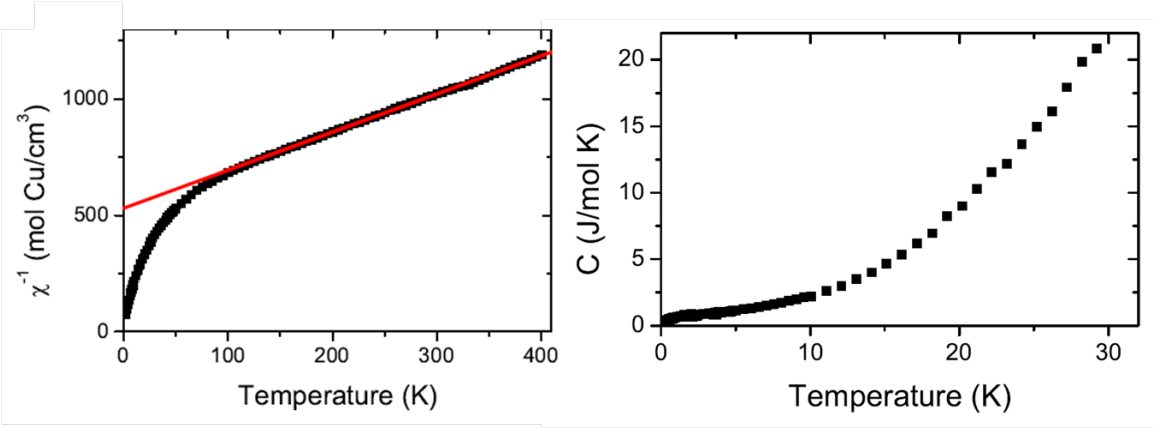

Figure 1.8: The inverse magnetic susceptiblity and heat capacity of Herbertsmithite. The inverse susceptiblity shows paramagnetic behavior down to ~100 K (paramagnetic fit shown as red line), with no sign of magnetic ordering at any temperature. The heat capacity shows no evidence of any type of phase transition below 30 K [9].

neutron scattering was possible.

Figure 1.9 shows the results of the inelastic neutron scattering measurements taken by Han *et al.* [34] on single-crystal Herbertsmithite. They find in the dynamic structure factor a scattering continuum with featureless regions of scattering comparable in size to the entire Brillouin zone. Such a scattering continuum is consistent with magnetic excitations based on the creation of two spinons with a gap no larger than 0.25 meV. Figure 1.9d shows the structure factor integrated from 1 to 9 meV to approximate the equal-time structure factor calculated by theory for a nearest-neighbor-only RVB state (Figure 1.9e). The data and theory qualitatively match extremely well, with both showing a hexagonal ring structure that spans multiple Brillouin zone areas in reciprocal space, with nearly constant scattering amplitude in the ring regions. The data, however, is narrower in reciprocal space than the theory, indicating correlations that extend beyond nearest neighbor spins. Furthermore, the data shows no evidence of a gap down to 0.25 meV where the contribution from the defect Cu spins dominates the signal. This suggests that the ground state of Herbertsmithite is a gapless long-range RVB with fully gapless spin excitatations, though a gap smaller than the 0.1 meV bound set by powder neutron scattering measurements [18] is not ruled out.

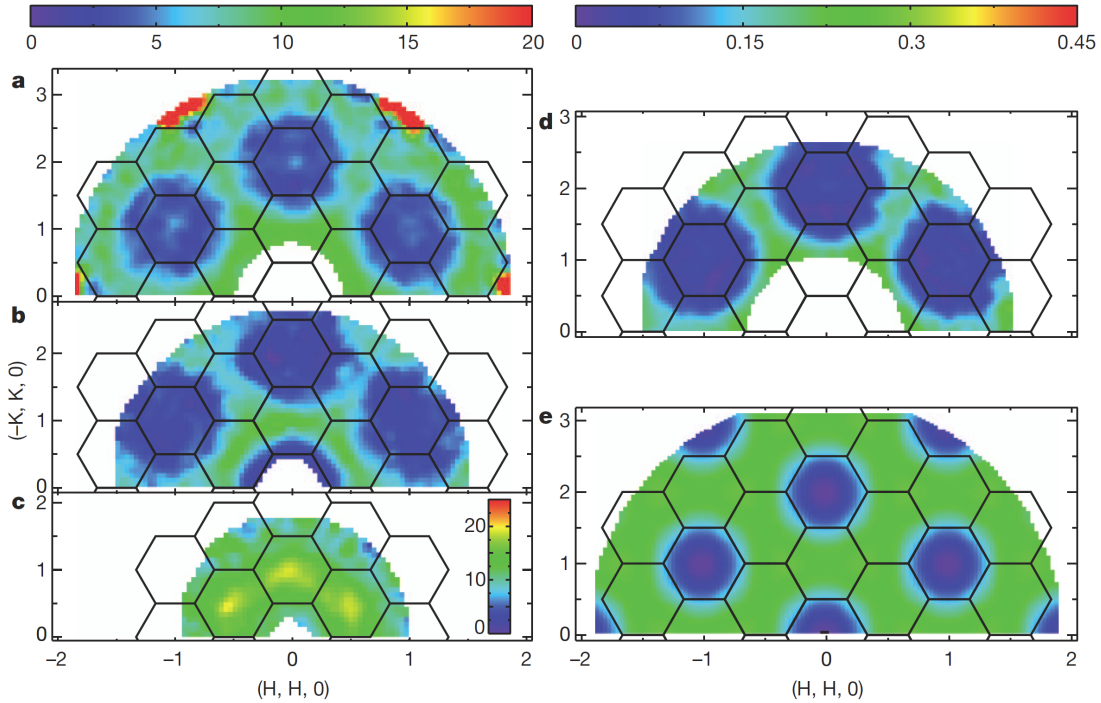

Figure 1.9: Inelastic neutron scattering measurements on single-crystal Herbertsmithite taken from reference [34]. a)-c) Dynamic structure factor for energy transfer $\hbar\omega = 6\ meV$, $2\ meV$, and $0.75\ meV$, respectively. A broad, featureless, scattering continuum is observed. The energy-integrated structure factor (d) is compared to theoretical predictions for nearest-neighbor dimers (Type I short-range RVB) (e). The data are narrower in reciprocal space than the theory, indicating spin-spin correlations that extend beyond nearest-neighbors.

Neutron scattering measurements suggest that a gapless QSL state is realized in Herbertsmithite, specifically the U(1) Dirac spin liquid suggested by theory [18, 58], however there remains much controversy regarding this question. A recent computational study instead suggested that a fully gapped Z_2 spin liquid is realized in Herbertsmithite [59], while other computational work suggests that a honeycomb VBC with a large 36 site unit cell is the true ground state [24, 28]. Attempting to resolve this issue will be the main focus of this dissertation, specifically in chapter 4. Instead of scattering experiments that look directly for spin gaps, we will instead look for signatures of the gauge symmetry of the ground state wavefunction in the dissipation of low-frequency light.

1.6 Optical conductivity of Quantum Spin Liquids

Experimental techniques that specifically probe the spin degrees of freedom seem, at least a priori, to be the ideal choice for studying the physics of the magnetism in Herbertsmithite, however, the large percentage of defect Cu spins on the Zn sites often dominates the signal at low energies, as in the neutron scattering work previously mentioned. In order to determine the nature of the spinon excitations in Herbertsmithite, that is, determine the existence of a spin gap, one must be able to perform accurate measurements in the very low energy limit with these techniques. A more direct probe of these emergent spinon excitations is therefore preferable. Despite Herbertsmithite being a strong Mott insulator, it has been proposed that the low-frequency optical conductivity could be used to determine the existence and nature of emergent gauge fields that are specific to the type of QSL present [40, 41].

1.6.1 Gapless U(1) Dirac spin liquids

Two contributions to the optical conductivity are expected in U(1) Dirac spin liquids due to the coupling of the usually well-insulating charge degree of freedom to the spin degree of freedom through an emergent gapless U(1) gauge field [40, 41]. The first contribution, which we will refer to as the Ioffe-Larkin conductance, arises because the applied electric field of the light produces virtual charge fluctuations which give rise to an emergent gauge electric field. The two fields then couple linearly, leading to a contribution to the optical conductivity. The predicted conductance per kagome layer is proportional to the square of the light frequency, and has the form [41]

$$\sigma_{IL} \approx 48\sqrt{3}\pi \frac{t^2(\hbar\omega)^2}{U^4}\frac{e^2}{h}, \tag{1.7}$$

where t is the hopping parameter estimated to be 0.1 eV and U is the on-site Coulomb repulsion estimated to be 1 eV. The conductance at 1 THz is therefore expected to be $\sim 10^{-5}\ \frac{e^2}{h}$. While this conductance is quite small, this effect exists only in the low frequency limit, where $\omega \ll J \approx 4.5\ THz$, which is well below the Mott gap and well

into the insulating regime. At frequencies below the lowest energy optical phonon, this contribution is expected to be the dominant one.

The second mechanism also relies on the existence of a gapless U(1) gauge field, and involves the modulation of the exchange interaction strength due to a deformation of the crystal lattice by the incident electric field, called magneto-elastic (ME) coupling. This modulation gains a loss mechanism through the emergent U(1) gauge field, resulting in a contribution to the optical conductivity [41]. The conductance per kagome layer also has a power-law form [41]

$$\sigma_{ME} \approx \left(\frac{\hbar\omega}{K_{Cu}a^2}\right)^2 \frac{e^2}{h}, \tag{1.8}$$

where K_{Cu} is the Cu-Cu bond spring constant and a is the Cu-Cu separation distance. $K_{Cu}a^2$ is estimated to be 1 eV, giving a conductance at 1 THz of $\sim 10^{-5}\frac{e^2}{h}$. This is comparable to σ_{IL} due to its large prefactor, but the ME contribution may dominate depending on the detailed values of the t and U.

1.6.2 Gapped Z_2 spin liquids

In a fully gapped Z_2 spin liquid, the applied electric field cannot induce charge fluctuations that lead to optical conductivity because those charge fluctuations are a consequence of a gapless U(1) gauge field that is not present in the Z_2 case [41]. For the same reason, the modulation of the exchange coupling of the spins is not lossy in a Z_2 spin liquid. However, other mechanisms for optical conductivity arising from the spin degree of freedom in Herbertsmithite exist in Z_2 spin liquids as well as in U(1) Dirac spin liquids, which must be considered when interpreting experimental data. The primary contribution is from the modulation of the Dzyaloshinskii-Moriya (DM) interaction by the electric field of the incident light.

Herbertsmithite has a modest DM interaction strength of $\sim J/10$ due to the moderate spin-orbit coupling strength in copper as well as the 120° angle of the Cu-O-Cu

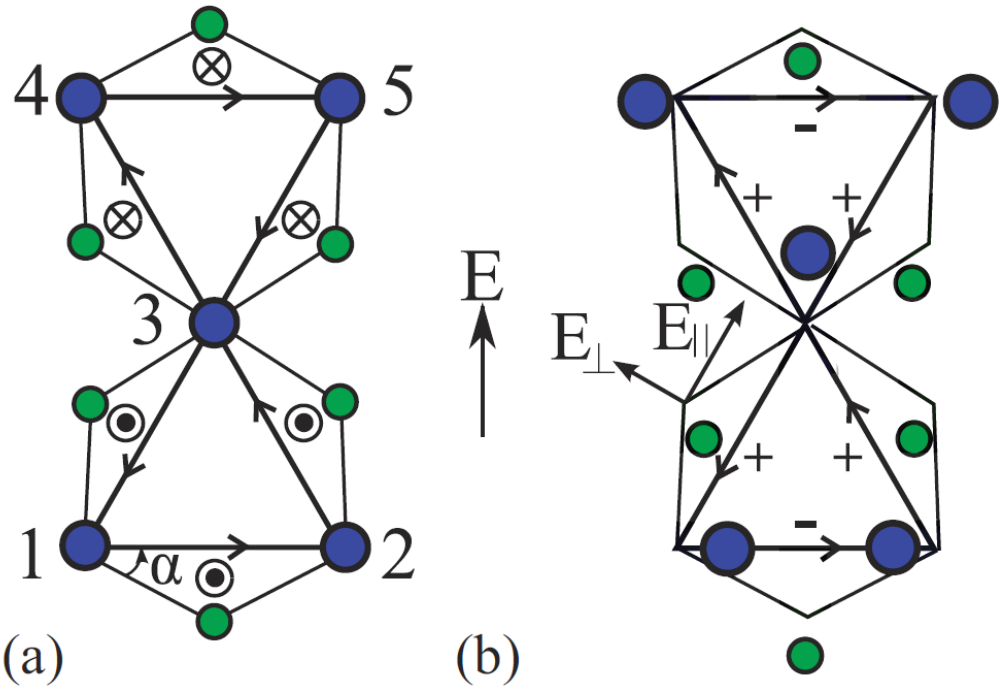

Figure 1.10: A representation of the DM interaction in Herbertsmithite arising from the angled Cu-O-Cu bond, with Cu shown in blue and O in green. a) The unperturbed lattice gives rise to a DM vector whose direction is perpendicular to the kagome planes and is dependent on the specific Cu-O-Cu bond. b) The THz electric field perturbs the lattice, modulating the magnitude of the DM vector in a bond-dependent way, shown as + or -. This perturbation is lossy, resulting in a contribution to the optical conductivity. Figured obtained from reference [41].

bonds [18]. The DM wavevector is defined by the DM contribution to the Hamiltonion

$$H_{DM} = \sum_{<i,j>} \vec{D}_{ij} \cdot (\vec{S}_i \times \vec{S}_j), \tag{1.9}$$

where $\vec{D}_{ij} = \vec{D}$ for the isotropic nearest-neighbor-only case, and is always perpendicular to the kagome planes when the spins lie in the plane. Figure 1.10a shows the structure of $\vec{D}$ within a kagome plaquette, the direction of which depends on the location of the Cu-O-Cu bond in the plaquette. When an incident electric field is applied, the crystal structure is perturbed (Figure 1.10b), resulting in a site-dependent modulation of $\vec{D}$. It was recently shown that this modulation at finite frequencies

leads to energy loss (conductivity) [41]. The conductance takes the form [41]

$$\sigma_{DM} \approx \sigma_s \left(\frac{D}{J}\right)^2 \left(\frac{\hbar\omega}{K_{eff}a^2}\right)^2 \frac{e^2}{h}, \tag{1.10}$$

where $K_{eff} = \left(\frac{1}{K_O cos(\alpha)} - \frac{1}{K_{Cu}}\right)^{-1}$ is the effective spring constant, α is the Cu-O-Cu bond angle, D is the magnitude of the DM vector, J is the magnitude of the exchange coupling, and σ_s is the spin conductivity, which is a constant of order 1 in a Dirac spin liquid. This has a similar form to the ME contribution for a U(1) Dirac spin liquid, except reduced by a factor of $\left(\frac{D}{J}\right)^2$, giving a conductance per layer of $\sim 10^{-7}\frac{e^2}{h}$.

1.6.3 Experimental prospects

We have presented multiple aspects of the spin system in Herbertsmithite that contribute to the low-frequency optical conductivity. All of these mechanisms result in an optical conductivity that scales as ω^2, but the magnitude of the predicted conductivity is ~100 times larger in the case of a U(1) Dirac spin liquid with an emergent gapless U(1) gauge field than in a fully gapped Z_2 spin liquid. In the rest of this dissertation, we will present Terahertz Time-Domain Spectroscopy (THz-TDS), which is an optical technique capable of measuring the complex conductivity of materials in the few meV energy range. We will then present THz-TDS measurements performed on single-crystals of Herbertsmithite, from which we will observe a contribution to the optical conductivity that is consistent with a U(1) Dirac spin liquid state.

Chapter 2

Terahertz Time-Domain Spectroscopy

A large number of spectroscopic techniques have previously been developed to probe the electrodynamic response of materials spanning a wide range of photon energies, from μeV to eV [60, 61]. While many experimental techniques exist for most of this energy range, there is a dearth of emitters, detectors, and optics that operate at Terahertz (THz) frequencies (0.1 to 10 THz), often referred to as the "Terahertz gap" [62, 63]. This energy range is extremely relevant to the physics of a wide variety of materials, including superconducting gaps in BCS and high T_c superconductors [64–67], scattering rates in metals and semiconductors [68–71], the opening of gaps in the surface states of topological insulators [72–74], and, as discussed in chapter 1, the finite-frequency conductivity of spin liquid systems [40, 41, 75, 76]. The development and refinement of spectroscopic techniques in this frequency range is therefore of great importance in the study of these, and many other, material systems.

In this chapter, we will discuss Terahertz Time-Domain Spectroscopy (THz-TDS), a phase-coherent spectroscopic technique that operates in the THz range (0.2-2.5 THz) based on the generation and detection of broadband THz pulses using ultrafast near-infrared lasers. Unlike similar techniques, such as Fourier Transform Infrared Spectroscopy (FTIR), which measure the intensity of transmitted or reflected light, THz-TDS probes the time-dependent electric field of THz pulses, allowing for the measurement of complex material properties without the use of the Kramers-Kronig relations, which require accurate interpolations to frequencies outside the measured

range [77].

2.1 Terahertz generation and detection using non-linear optics

For all of the measurements presented in this dissertation, we utilized non-linear optics to generate and detect broad-band THz pulses. The THz pulses were generated by frequency conversion of ultra-short ($\sim 100fs$) near-infrared laser pulses using a second-order optical effect called optical rectification. The pulses were subsequently detected via free-space electro-optic sampling using the Pockels effect.

2.1.1 Optical Rectification

In linear optics, the polarization P induced in a material by an applied electric field E can be written $P = \epsilon_0 \chi E$, where ϵ_0 is the permittivity of free space, and χ is the electric susceptibility of the material. From Maxwell's equations, a generalized wave equation can be derived [78, 79],

$$\frac{\partial^2 E}{\partial z^2} - \frac{1}{c^2}\frac{\partial^2 E}{\partial t^2} = \frac{1}{\epsilon_0 c^2}\frac{\partial^2 P}{\partial t^2}, \tag{2.1}$$

which reduces to

$$\frac{\partial^2 E}{\partial z^2} - \frac{n^2}{c^2}\frac{\partial^2 E}{\partial t^2} = 0, \tag{2.2}$$

where $n = \sqrt{1+\chi}$ is the index of refraction. This is simply the free-space wave equation with a velocity modified by the index of refraction.

In non-linear optics, the polarization is allowed to depend generally on the electric field, and can be written as $P = \epsilon_0(\chi_1 E + \chi_2 E^2 + \chi_3 E^3 + ...)$, with the higher order terms becoming relevant when a strong electric field is present [80]. For all further discussion on non-linear optics, we will restrict ourselves to the case where only the first- and second-order terms are significant. For the case of a mono-chromatic plane-wave $E = E_0 \cos(\omega t)$ in a non-linear medium, the electric polarization can be

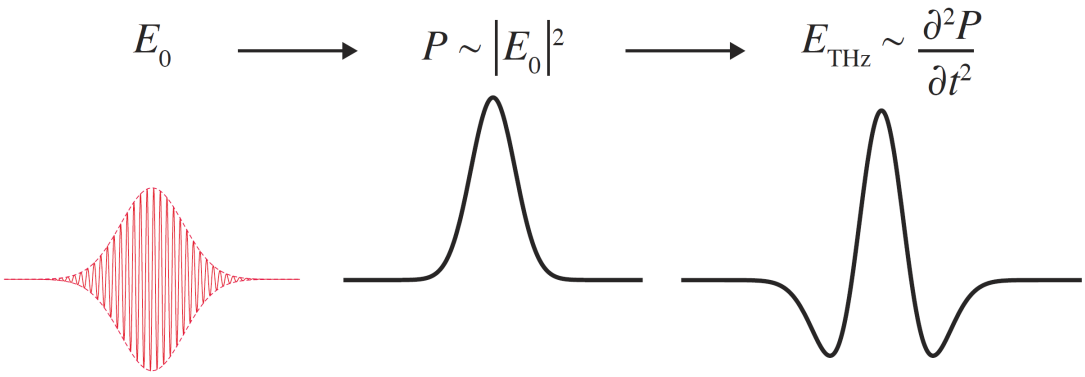

Figure 2.1: Simplified illustration of THz generation via optical rectification. A generation pulse with Gaussian envelope $E_0 \propto exp(\frac{-t^2}{\tau^2})$ induces a slowly-varying nonlinear polarization $P \propto |E_0|^2$. Maxwell's equations dictate that light will be radiated with electric field $E_{THz} \propto \frac{\partial^2 P}{\partial t^2}$. Figure obtained from reference [81]

rewritten as $P = \epsilon_0(\chi_1 E_0 \cos(\omega t) + \chi_2 E_0^2 \cos^2(\omega t))$, where the second order term can be rewritten as $P_{SO} = \frac{1}{2}\epsilon_0 \chi_2 E_0^2(\cos(2\omega t) + 1)$. The first term of P_{SO} will lead to second-harmonic generation (which we will ignore), while the second term yields a static polarization. Plugging this into equation 2.1 yields,

$$\frac{\partial^2 E}{\partial z^2} - \frac{n^2}{c^2}\frac{\partial^2 E}{\partial t^2} = \frac{1}{\epsilon_0 c^2}\frac{\partial^2 P_{SO}}{\partial t^2} = \frac{\chi_2}{2c^2}\frac{\partial^2 (E_0^2)}{\partial t^2}, \tag{2.3}$$

which will result in non-zero radiation if we allow E_0 to vary with time.

Terahertz generation via optical rectification occurs if we instead consider the nonlinear polarization induced by an ultra-short ($\sim 100 fs$) laser pulse with a Gaussian envelope $E_0(t) \propto exp(\frac{-t^2}{\tau^2})$, where τ is the laser pulse width. Equation 2.3 now leads to a radiated electric field $E_{THz}(t) \propto \frac{\partial^2 (E_0^2)}{\partial t^2} \propto \frac{4}{\tau^4}(t^2 - \frac{\tau^2}{2})exp(\frac{-t^2}{\tau^2})$. A schematic of this process can be found in Figure 2.1. Taking the Fourier transform of this radiated electric field gives $E_{THz}(\omega) \propto (\omega^2 \tau) exp(\frac{-\omega^2 \tau^2}{4})$. For a typical value of $\tau = 100\ fs$, we obtain a radiated electric field with bandwidth of about 0-8 THz, with a peak at about 3 THz.

It is important to note that this treatment of optical rectification is extremely simplified, and does not take into account imperfect phase matching conditions, frequency dependence of the nonlinear susceptibilities, or absorption in the nonlinear

crystal, among other complications. These complications limit the generated THz bandwidth to about 0.2-2 THz. Furthermore, The magnitude and polarization of the generated THz pulse depends strongly on the orientation of the nonlinear crystal as well as the relative orientation of the generation beam polarization to the crystal axes [63, 82]. For all of the work on this dissertation, we used zinc telluride (ZnTe) due to its large second-order susceptibility and good index-matching between 800 nm and the THz range [63]. The ZnTe crystal was cut along the (110) direction and with the [001] axis oriented at a 54.7° angle relative to the generation beam polarization to achieve maximum THz generation with polarization parallel to the generation beam polarization [63].

2.1.2 Free-space electro-optic sampling

The THz pulses are detected using a technique called free-space electro-optic sampling [63]. This technique uses the Pockels effect (linear electro-optic effect) to rotate the polarization of an 800 nm detection pulse by an angle proportional to the THz electric field. Similar to optical rectification, the Pockels effect is a second-order nonlinear effect that arises from the same second-order electric susceptibility of a nonlinear crystal, in this case ZnTe. To understand the Pockels effect, it is useful to consider the second-order polarization in tensor form.

$$P_i^{SO,(\omega_1-\omega_2)} = \chi_{ijk}^{(\omega_1-\omega_2)} E_j^{(\omega_1)} E_k^{(\omega_2)} \tag{2.4}$$

We now treat the THz electric field as a DC electric field, and obtain

$$P_i^{SO,(\omega_1)} = \chi_{ijk}^{(\omega_1)} E_j^{(\omega_1)} E_{THz,k}. \tag{2.5}$$

This polarization has the same form as a the linear polarization $P_i = \chi_{ij} E_j$, so we now obtain a modified linear electric susceptibility given by

$$\chi_{ij}^*(\omega) = \chi_{ij}(\omega) + \chi_{ijk}(\omega) E_{THz,k}. \tag{2.6}$$

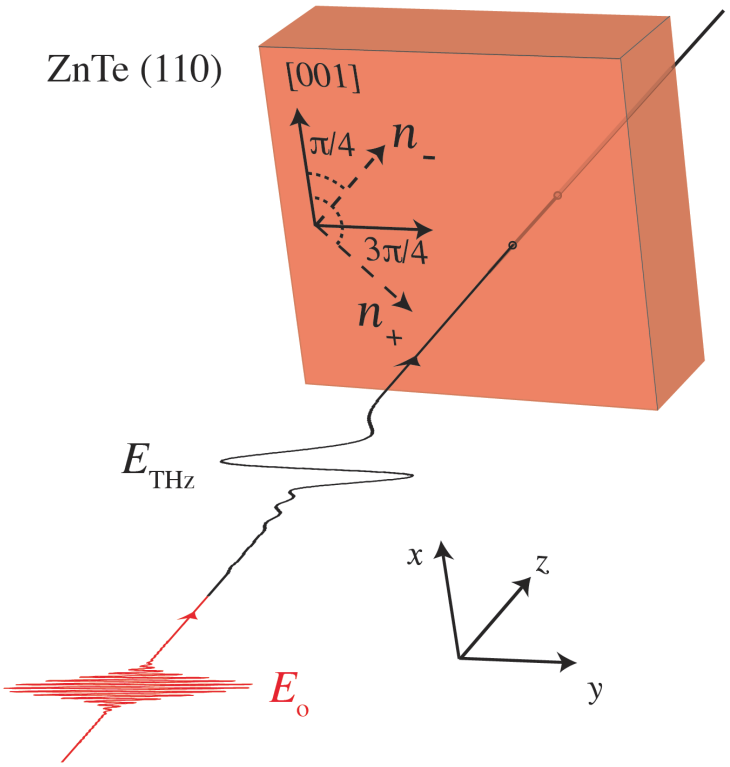

Figure 2.2: A schematic of the electro-optic sampling setup. A ZnTe detection crystal cut in to (110) direction is aligned such that the [001] crystal axis is along the $\hat{x}$ direction. The THz and detection polarizations E_{THz} and E_0, respectively, are aligned in the $\hat{y}$ direction, and are incident upon the detection crystal at normal incidence. The THz electric field induces a birefringence along the n_+ and n_- directions via the Pockels effect, resulting in a phase shift of the detection polarization $\phi \propto E_{THz}$. Figured obtained from reference [81].

The result is a THz electric field-induced birefringence that depends on the point-group symmetry and orientation of the electro-optic crystal, the polarization of the THz pulses, and the polarization of the detection pulses.

In our experiments, we used a ZnTe crystal cut in the (110) direction, with $\vec{E}_{THz} \| \vec{E}_{detection}$ and perpendicular to the [001] crystal axis, which is parallel to the $\hat{x}$-axis of the lab frame. Figure 2.2 shows a schematic for this electro-optic sampling geometry. In this geometry, a birefringence is induced with principal axes $\hat{x}+\hat{y}$ and $\hat{x}-\hat{y}$ in the lab frame [83]. For small THz electric fields, the index of refraction for detection pulse polarization parallel to $\hat{x}+\hat{y}$ becomes $n_- = n_0 - (1/2)n_0^3 r_{41} E_{THz}$, and

for detection pulse polarization parallel to $\hat{x}-\hat{y}$ becomes $n_+ = n_0 + (1/2)n_0^3 r_{41} E_{THz}$, where n_0 is the isotropic index of refraction in the absence of THz, and r_{41} is the electro-optic coefficient for the ZnTe crystal [83]. We consider an initial detection pulse polarization $\vec{E}_{det} = E_0\hat{y}$. It is convenient to rotate our frame of reference by $\pi/4$ to be aligned with the principal axes. In this frame, the polarization can be written as,

$$\vec{E}'_{det} = \frac{E_0}{\sqrt{2}}(\hat{x}+\hat{y}) = \frac{E_0}{\sqrt{2}}\begin{pmatrix}1\\1\end{pmatrix}. \tag{2.7}$$

Using the Jones matrix for propagation through a birefringent medium [84],

$$P = \begin{pmatrix} e^{in_-\omega d/c} & 0 \\ 0 & e^{in_+\omega d/c} \end{pmatrix}, \tag{2.8}$$

where ω is the detection pulse frequency and d is the electro-optic crystal thickness, we can obtain the polarization after the crystal by taking $\vec{E}'_{det} \rightarrow P\vec{E}'_{det}$, giving

$$\vec{E}'_{det} = e^{in_-\omega d/c}\frac{E_0}{\sqrt{2}}\begin{pmatrix}1\\e^{i(n_+-n_-)\omega d/c}\end{pmatrix}, \tag{2.9}$$

where $n_+ - n_- = n_0^3 r_{41} E_{THz}$. Progagating through the crystal, therefore, introduces a phase shift $\phi = (n_+ - n_-)\omega d/c \propto E_{THz}$ between the components of the detection polarization along the principle axes of the crystal.

In order to measure this phase shift, and hence the THz electric field, the detection pulse is then sent through a ¼-wave plate and a Wollaston prism before being detected by a pair of photodiodes. The ¼-wave plate introduces an additional phase shift of $\pi/2$, giving

$$\vec{E}'_{det} = e^{in_-\omega d/c}\frac{E_0}{\sqrt{2}}\begin{pmatrix}1\\e^{i(\phi+\pi/2)}\end{pmatrix}. \tag{2.10}$$

After rotating back to the lab frame we obtain

$$\vec{E}_{det} = e^{in_-\omega d/c}\frac{E_0}{2}\begin{pmatrix}1+e^{i(\phi+\pi/2)}\\1-e^{i(\phi+\pi/2)}\end{pmatrix}. \tag{2.11}$$

The Wollaston prism splits the x-polarized and y-polarized components of the de-

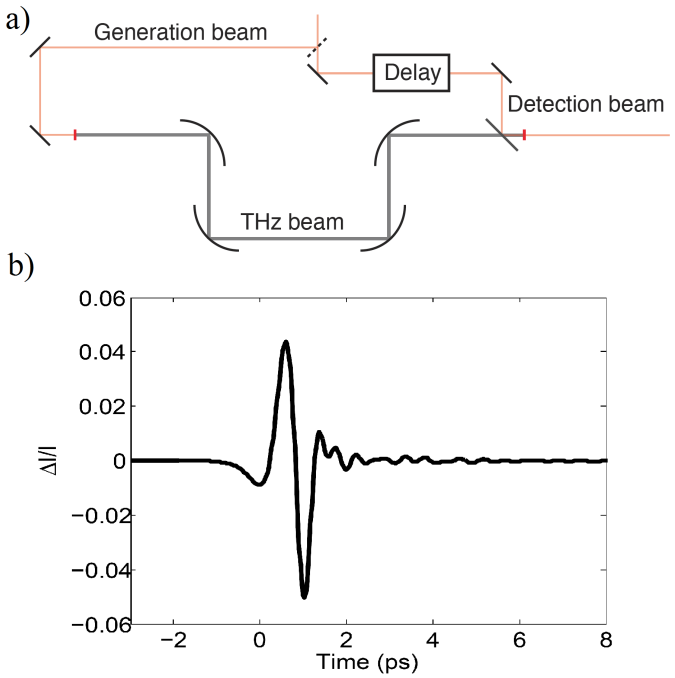

Figure 2.3: a) A schematic of the THz generation and detection optics. The detection beam is coupled collinearly with the THz beam using a pellicle beam splitter. b) An example THz waveform measured by changing the time delay between the arrival of the THz and detection pulses at the ZnTe detection crystal.

tection pulse, which are detected by a pair of photodiodes. The photodiode signal is proportional to the magnitude of the Poynting vector $S = \frac{1}{2}\sqrt{\frac{\epsilon_0}{\mu_0}}(\vec{E}\cdot\vec{E}^*)$ [78, 79]. Plugging in equation 2.11 gives the measured photodiode signal

$$I = I_0(1 \pm \sin\phi) \approx I_0(1 \pm \phi), \tag{2.12}$$

where I_0 is the photodiode signal when the THz pulses are absent. Taking the difference between the diode signals and normalizing by I_0 gives

$$\frac{1}{2}\frac{\Delta I}{I_0} = \phi = \frac{\omega d}{c} n_0^3 r_{41} E_{THz} \propto E_{THz}. \tag{2.13}$$

We have now described an optical technique to measure the electric field of a THz pulse that is temporally overlapped with a detection pulse in the ZnTe detection crystal, under the assumption that the THz electric behaves as a static field over the duration of the detection pulse. Since the detection and THz pulses have pulse widths

100 fs and ~2 ps, respectively, this is a good approximation. In order to measure the THz electric field waveform as a function of time, a mechanical delay stage is used to change the path length of the detection beam relative to the generation beam. When the detection beam path length is shorter than that of the generation beam, no THz electric field is measured, corresponding to a measurement at a time prior to the arrival of the THz pulse. Lengthening the detection beam path length by a distance d advances the measurement time by $t = \frac{d}{c}$, corresponding to a time change of ~3.33 ps/mm. This allows us to sample the THz electric field at any point along the THz pulse time axis. Figure 2.3 shows a schematic of this process along with an example of a THz waveform measured as a function of delay stage time delay.

2.2 Extraction of material properties using Thz-TDS

In THz-TDS, one measures the time-dependent THz electric field waveform $E(t)$ in order to extract the complex optical properties of a material. Since the recorded signal is proportional to the electric field, as opposed to the intensity, it contains magnitude and phase information about the transmission coefficient of the material through which the THz field is transmitted. The time-dependent signal is Fourier transformed to obtain $\tilde{E}(\omega) \equiv |E(\omega)|exp(i\phi(\omega))$. In order to extract meaningful properties of the material through which the THz was transmitted, $\tilde{E}(\omega)$ must be compared to the electric field incident upon the sample, $\tilde{E}_i(\omega)$. To do this, one must measure the THz waveform after it is transmitted through the sample, $\tilde{E}_s(\omega)$, and the THz waveform after it is transmitted instead through a reference material, $\tilde{E}_r(\omega)$, which is often a bare reference substrate or even vacuum.

2.2.1 Jones Matrix formalism

The Jones matrix formulation is a useful tool for analyzing the propagation of electromagnetic waves through multiple interfaces [84]. In this formalism, the electric field of the light is represented as a two-component vector $\vec{E} = (E_x, E_y)$. The electric field evolves as it propagates through each optical interface until it is detected, resulting

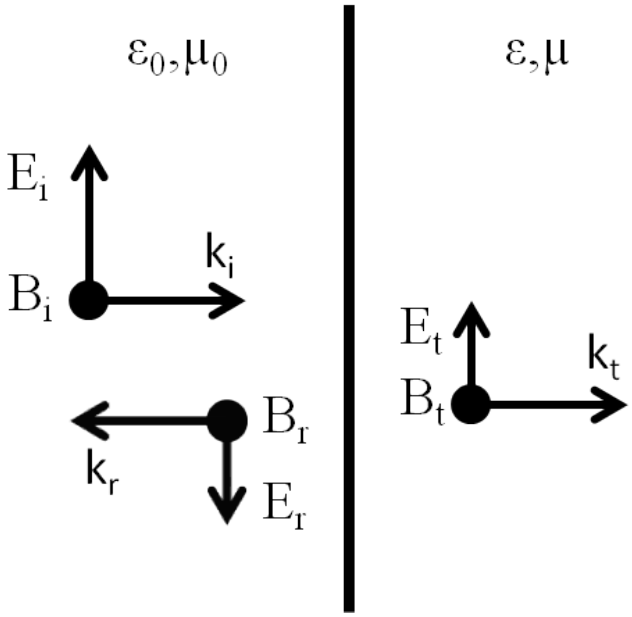

Figure 2.4: Transmission and reflection of light at an interface between vacuum and a material with relative permittivity and permeability ϵ and μ, respectively. Light is incident upon the interface from the left with electric and magnetic fields E_i and B_i, respectively, and wavevector k_i. Some of the light is reflected (E_r, B_r, k_r) and some is transmitted (E_t, B_t, k_t). The relationship between these fields is governed by boundary conditions at the interface determined by Maxwell's equations.

in a final electric field vector $\vec{E}_f$. A 2×2 matrix M is associated with each interface. The detected electric field can then be written as $\vec{E}_f = M_N \cdot M_{N-1}...M_2 \cdot M_1 \vec{E}_i$. In the case where all optics and materials preserve the polarization of the THz, an intial THz polarization can bet set, say $\vec{E}_i = E_i \hat{x}$, and all the matrices M_N can be treated as numbers. Since all the Jones matrices (which will now be treated as numbers) for the two measured waveforms $\tilde{E}_s(\omega)$ and $\tilde{E}_r(\omega)$ are identical except for the matrices describing the transmission through the sample or reference, M_s and M_r respectively, the ratio $\frac{\tilde{E}_s(\omega)}{\tilde{E}_r(\omega)}$ divides out all but these two matrices, resulting in $\frac{\tilde{E}_s(\omega)}{\tilde{E}_r(\omega)} = \frac{M_s}{M_r} \equiv T$.

2.2.2 Fresnel equations and boundary conditions

The Jones matrices M_s and M_r (which we will now refer to as transmission coefficients) can be calculated using the Fresnel equations [78, 79], which consider the propagation of plane-waves through a material interface under the constraints dictated by Maxwell's equations. Figure 2.4 shows a schematic for the transmission

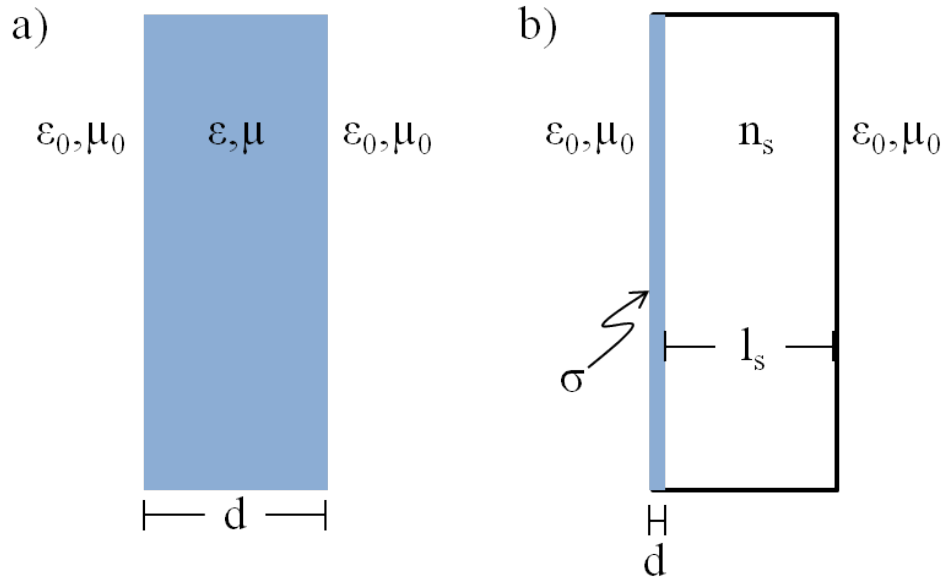

Figure 2.5: Example sample geometries. a) A flat, thick sample with permittivity and permeability ϵ and μ, respectively, and thickness $d \gg \lambda_{THz}$. This geometry is ideal for transmission geometry experiments when the material conductivity σ is small. b) A thin film sample with thickness $d \ll \lambda_{THz}$ and conductivity σ on a thick substrate with thickness $l_s \gg \lambda_{THz}$ and index of refraction n_s. This geometry is ideal when $Z_0 \sigma d > n_s$

of light through a material interface at normal incidence, with incident, reflected, and transmitted electric and magnetic fields $E_i, B_i, E_r, B_r, E_t, B_t$, respectively. The boundary conditions at this interface are

$$\begin{aligned} E_i + E_r &= E_t \\ B_i + B_r &= B_t + \mu_0 j_s, \end{aligned} \tag{2.14}$$

where j_s is the surface current density at the interface [78, 79].

We will consider two common sample geometries. The first is a smooth, flat sample with uniform thickness $d \gg \lambda_{THz}$. Figure 2.5a shows a schematic of this geometry. The transmission coefficient in this case is the product of three transmission coefficients: transmission through the first interface, propagation through the bulk of the sample, and transmission through the second interface. At both interfaces, the surface current density j_s is zero. Assuming a plane-wave form where $B =$

$\sqrt{\epsilon(\omega)\epsilon_0\mu(\omega)\mu_0}E$,where $\epsilon(\omega)$ and $\mu(\omega)$ are the relative permittivity and permeability of the material, respectively, we obtain a transmission coefficient of

$$T_s = \frac{4\tilde{n}(\omega)}{(\tilde{n}(\omega)+1)^2} exp(i\tilde{n}(\omega)\omega d/c), \tag{2.15}$$

where $\tilde{n}(\omega) = \sqrt{\epsilon(\omega)\mu(\omega)}$ is the complex index of refraction of the material, ω is the frequency of the light, and d is the sample thickness. For samples of this geometry, a common reference is vacuum, with transmission coefficient

$$T_r = exp(i\omega d/c). \tag{2.16}$$

We can now obtain a formula relating the ratio of measured electric field waveforms to the material optical properties.

$$\frac{\tilde{E}_s(\omega)}{\tilde{E}_r(\omega)} = T = \frac{4\tilde{n}(\omega)}{(\tilde{n}(\omega)+1)^2} exp(i(\tilde{n}(\omega)-1)\omega d/c)). \tag{2.17}$$

This equation can be numerically inverted using the method of Duvillaret et al. [85] to obtain both the real and imaginary components of $\tilde{n}(\omega)$ from the measured THz waveforms. Additionally, this technique can be used to extract the sample thickness d by including the first etalon of the THz signal in the scanned region [86].

The second sample geometry we will consider is a thin film sample (thickness $d \ll \lambda_{THz}$) on a thick substrate (thickness $l_s \gg \lambda_{THz}$) with known optical properties. Figure 2.5b shows a schematic of this geometry. Since the film is much thinner than the THz wavelengths, it can be treated as a surface with surface current density $j_s = \sigma dE$ induced by the electric field at the interface, where σ is the conductivity of the film material [78,79]. The transmission coefficient in this case is again a product of three transmission coefficients. After making the same plane-wave assumptions as before, but taking into account j_s according to formula 2.14, we obtain the transmission coefficient

$$T_s = \frac{4n_s(\omega)exp(in_s(\omega)\omega l_s/c)}{(n_s(\omega)+1)(n_s(\omega)+1+Z_0\sigma(\omega)d)}, \tag{2.18}$$

where $n_s(\omega)$ is the known substrate index of refraction and $Z_0 = \sqrt{\frac{\mu_0}{\epsilon_0}}$ is the impedance of free space. For samples of this geometry, a common reference is a bare substrate, preferably identical to the sample substrate. Since substrate thicknesses can vary by a few μm, we will consider the reference substrate to have thickness $l_r = l_s + \delta l$. The reference transmission coefficient is then given by

$$T_r = \frac{4n_s(\omega)}{(n_s(\omega)+1)^2} exp(in_s(\omega)(l_s + \delta l)/c), \tag{2.19}$$

and the ratio $\frac{\tilde{E}_s(\omega)}{\tilde{E}_r(\omega)}$ is given by

$$\frac{\tilde{E}_s(\omega)}{\tilde{E}_r(\omega)} = T = \frac{n_s(\omega)+1}{n_s(\omega)+1+Z_0\sigma(\omega)d} exp(-in_s(\omega)\delta l/c). \tag{2.20}$$

Equation 2.20 can be directly inverted to solve for $\sigma(\omega)$.

$$\sigma(\omega) = \frac{n_s+1}{Z_0 d}(\frac{exp(-in_s(\omega)\delta l/c)}{T} - 1) \tag{2.21}$$

We have therefore shown that is possible to directly measure the complex index of refraction (for thick samples) and the complex conductivity (for thin films) of materials using THz-TDS.

2.3 Implementation of THz-TDS in the Gedik lab

2.3.1 Laser source

Our experiments were performed using a Spectra-Physics Spitfire Pro titanium-doped sapphire (Ti:sapph) amplified laser system, pumped by an Empower 30 Q-switched Nd:YLF laser operating at 527 nm, and seeded by a Tsunami Ti:sapph oscillator with 80 MHz repetition rate and 100 fs pulse duration with a center wavelength of 800 nm. The amplifier produced pulses at 5 kHz repetition rate with 100 fs pulse duration, 800 nm center wavelength (1.55 eV photon energy), and ~4 W average power (800 μJ per pulse). The pulses were first split by an 80:20 beam splitter,

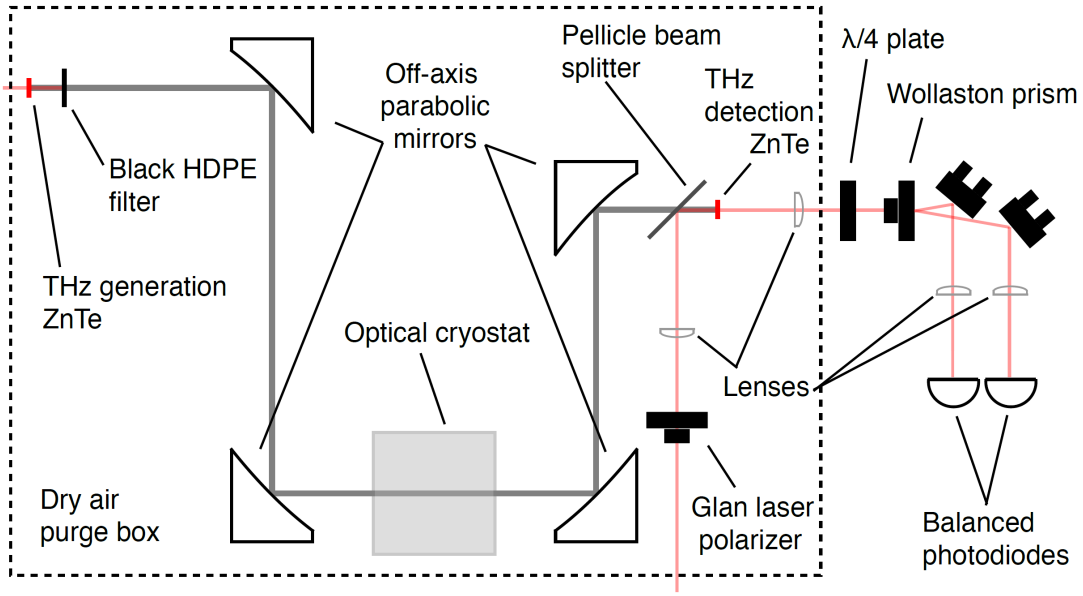

Figure 2.6: Schematic of the THz optics in the Gedik lab. The 800 nm generation and detection beams are shown in red, while the THz beam is shown in grey. The entire THz path is enclosed in a box that is purged with dry air to minimize absorption of the THz by water.

with 80% being used as an excitation source for pump-probe experiments, which are outside of the scope of this dissertation. The remaining 20% was subsequently split by a pellicle beam splitter, with 92% being used for THz generation (the generation beam), and the remaining ~8% being used for THz detection (the probe beam). A schematic of the optical setup can be seen in Figure 2.6.

2.3.2 Terahertz generation and propagation

The THz pulses were generated via optical rectification of the 1.55 eV generation beam in a 1 mm thick ZnTe crystal ((110) crystal orientation). A thin piece of black HDPE (high density polyethylene) was used to block the subsequently transmitted generation beam while transmitting most of the THz pulse [63]. We used four 90° off-axis parabolic mirrors (OAPMs) with 2 inch diameter in a confocal geometry to collimate the THz beam, focus it through a sample, collimate the beam again, and

finally focus it onto a ZnTe used for detection (more information on THz detection is presented in the next section). A diagram of this optical setup can be seen in Figure 2.6. We chose OAPMs with focal lengths of 6 inches, 4 inches, 4 inches, and 3 inches, respectively, resulting in the imaging of the initial THz spot size onto the sample with a magnification ratio of 2/3. The shorter focal length of the last OAPM was chosen in order to minimize the THz spot size on the detection crystal which increased the dynamic range of THz detection.

The generation beam size and intensity were also chosen carefully to optimize the propagation of the THz pulses through the setup, maximize the THz signal size, and to minimize the THz peak noise. A small generation beam spot size corresponded to a smaller THz spot size on the sample, but also resulted in greater loss on the first OAPM due to the greater divergence of the THz pulses. A generation beam spot size of $\sim 2mm$ full-width at half maximum (FWHM) on the generation crystal was found to be optimum for this setup. The average power of the generation beam was controlled by a thin-film polarizer and half-wave plate combination, and was chosen to be $\sim 220mW$ (pulse energy $u = 44\ \mu J$), which maximized the generated THz power while avoiding white light generation in the ZnTe generation crystal, which we found to cause long term damage to the crystal.

We enclosed the entire THz optical path in a custom-built enclosure that was purged with dry air to reduce the resonant absorption of parts of the THz bandwidth due to water vapor [87]. Not only did it prevent the complete loss of THz signal at certain frequencies, it also removed ringing in the time domain, effectively shortening the THz pulses, which helped improve certain Fourier transform artifacts that would otherwise appear (more detailed discussion on this can be found in the next section). We used a commercial regenerative air dryer (DelTech WM-13N), which filtered and dehumidified the compressed building air supply, providing an effectively unlimited air supply with negligible humidity. The regenerative nature of this air drier made this solution much more convenient and cost-effective than purging with nitrogen gas. In our experiments, the dry air flow rate was minimized, to reduce noise in the THz detection, while still maintaining a measured relative humidity of 0.1%.

Additionally, we enclosed the entire optical setup in an enclosure built from black anodized aluminum extrusions with black HDPE walls, and removable clear acrylic lids (80-20, Inc.). The enclosure reduced noise in the detected THz signal by reducing air currents in the optical path, which helped stabilize the laser power, pointing, and mode at the THz generation and detection crystals.

2.3.3 Terahertz detection system

The THz pulses were measured using electro-optic sampling of 800 nm detection pulses in a 1 mm thick ZnTe crystal. As discussed in previous sections, the 800 nm detection pulses were coupled collinearly with the THz pulses using a pellicle beam splitter before undergoing the Pockels effect in a ZnTe detection crystal. The detection pulses were focused onto the detection crystal using a 2:1 telescope, which ensured that the THz electric field experienced by the entire detection pulse was both maximized and constant. The focusing of the detection pulses also made the THz field measurements more stable to pointing fluctuations. After the detection crystal, the detection pulses passed through a ¼-wave plate before being split by a Wollaston prism and finally were focused onto a pair of balanced photodiodes (Thorlabs DET36A). The photodiode currents were then sent to a pair of current pre-amplifiers (Stanford Research Systems SR570), whose outputs were then set to a data acquisition (DAQ) card (National Instruments PCI-6143) to digitally record the photodiode signals.

To measure the THz electric field using the DAQ card, we used the method described by Werley et al. [88]. Using a mechanical chopper (New Focus 3501), we chopped the generation beam at half the laser repetition rate, $f/2 = 2500\ Hz$, such that every other pulse was completely blocked. As a result, the THz pulses were only present in the detection crystal for every other detection pulse, with the pulse repetition phase locked to the chopper phase. To perform the measurement of the THz electric field, four pulses were measured: A1, A2, B1, and B2, corresponding to two consecutive pulses measured in photodiodes A and B, respectively. For pulses A1 and B1, the THz pulses were present, resulting in a photodiode intensity of $I + \Delta I$

and $I - \Delta I$, respectively, where I is the photodiode signal intensity in the absence of a THz pulse, and ΔI is the change in the photodiode signal due to the presence of a THz pulse. The following mathematical operation was then performed to extract a value proportional to the THz electric field:

$$\frac{1}{2}\left(\frac{A_1}{A_2} - \frac{B_1}{B_2}\right) = \frac{1}{2}\left(\frac{I + \Delta I}{I} - \frac{I - \Delta I}{I}\right) = \frac{\Delta I}{I} \propto E_{THz}. \tag{2.22}$$

This operation was averaged over 250 consecutive pairs of pulses for each measurement in the THz electric field in time. The path length of the detection pulses was then varied using a delay stage (Newport ILS100PP) to change the timing of the overlap of the detection pulses and the THz pulses, allowing for a measurement of the THz electric field with time varying over the whole pulse duration.

In order to perform this operation with the DAQ card, the chopper was triggered using a reference trigger from the laser, delayed in time by a digital delay generator (DDG, Stanford Research Systems DG535). The chopper phase relative to the laser trigger was set such that every pulse was either completely blocked or allowed to completely pass through the chopper blades (60 slot wheel). To achieve this, the chopper phase was changed until a dark line appeared in the generation beam profile, resulting from the interference of the clipped edge of the generation beam on the chopper wheel. After finding phase value where this line appeared in the center of the beam profile, we changed the phase by 90°, ensuring a phase value furthest away from clipping. The DDG delay time was then set such that the 5 kHz laser trigger corresponded in time with the peak of the photodiode signal measured by the DAQ card. Both the chopper trigger and delayed laser trigger were sent to the DAQ card. The chopper trigger was used as a trigger to begin the collection of data points, which were each taken at the time corresponding to each subsequent laser trigger, with values equal to the peak of each diode signal due to the DDG timing. Starting the data collection after the chopper trigger ensured that the first diode signal measured always corresponded to a pulse where the THz generation beam was not blocked, allowing formula 2.22 to be accurately used to measure the THz electric

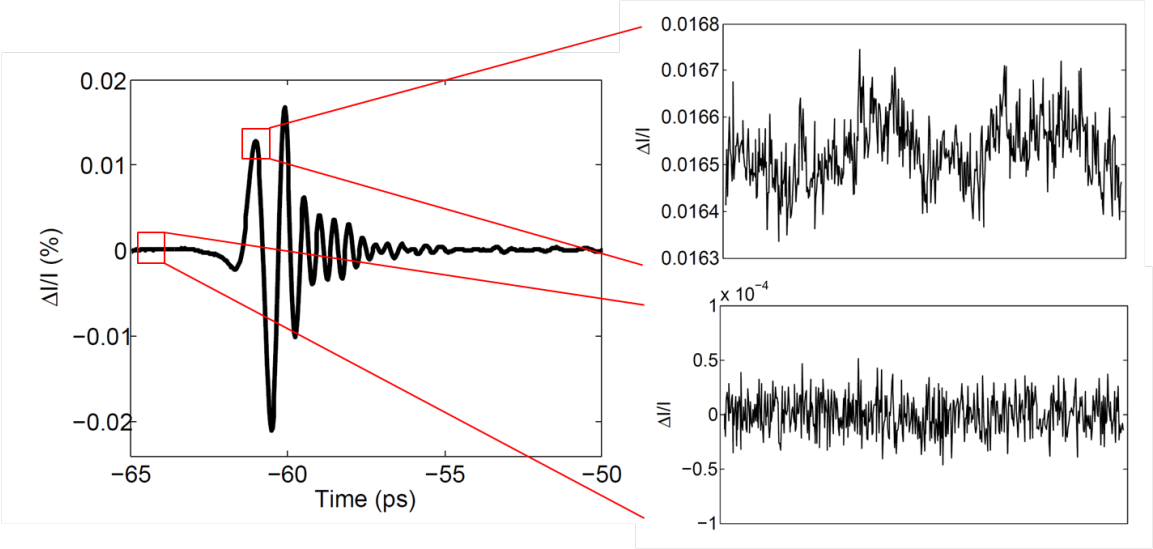

Figure 2.7: The types of noise in a sample THz waveform. The peak noise (top) is dominated by fluctuations of the laser power and pointing stability. The pre-noise (bottom) depends primarily on the presence of any polarization non-conserving optics and air currents in the detection beam path.

field for each pair of even and odd pulses after the chopper trigger.

2.3.4 Noise and artifact reduction

It was important to characterize and reduce multiple sources and types of noise and artifacts in the measurement of the THz waveforms in order to obtain precise and accurate measurements of the extracted material properties. Two metrics were used to characterize signal quality: The noise at time delays prior to the THz signal (pre-noise), and the ratio of the THz peak size and the noise at the THz peak time delay (signal-to-noise ratio or SNR). An example of these two types of noise can be seen in Figure 2.7.

The pre-noise corresponded to the noise of the detection system, and was independent of the generated THz pulses. We employed a number of techniques to reduce this noise down to a typical value of 1×10^{-5} of the photodiode signal peak. First, we employed a balanced and chopped photodiode detection system, as shown in formula 2.22. Other possible detection schemes include balanced (unchopped) detection and

chopped (unbalanced) detection.

$$\frac{1}{2}(A_1 - B_1) = \frac{1}{2}((I + \Delta I) - (I - \Delta I)) = \Delta I \propto I * E_{THz} \tag{2.23}$$

$$\frac{A_1}{A_2} - 1 = \frac{I + \Delta I}{I} - 1 = \frac{\Delta I}{I} \propto E_{THz} \tag{2.24}$$

The detection scheme for balanced detection can be seen in formula 2.23. While the result is proportional to the THz electric field, it is also proportional to the laser power, which can add significant noise to the measurement. Chopped detection (formula 2.24) solves this problem by providing a measurement of the THz electric field independent of laser power, except for power fluctuations at frequencies comparable to the laser repetition rate, which were typically very small. Combining these two detection schemes (formula 2.22) provided the best noise, as it provided two simultaneous measurements of the THz electric field for each pair of detected laser pulses.

A careful alignment of the detection beam through the detection optics was required to reach the desired pre-noise. Since our detection scheme was independent of laser power, we found that the pre-noise was independent of the detection beam alignment prior to the Glan laser polarizer (Figure 2.6), but depended strongly on alignment after the polarizer. Depolarizing effects of beam clipping, or for example a misaligned lens, were found to increase the pre-noise by up to an order of magnitude. To solve this problem, we used a 2:1 telescope to reduce the detection beam size (while also focusing onto the detection crystal) to avoid clipping (or near clipping) on the $1/4$-wave plate and Wollaston prism. We also mounted the detection crystal on a height-adjustable post (Thorlabs TRT2) and a dual-axis translation stage, because a fine adjustment of the crystal position relative to the detection beam was found to improve the pre-noise by a factor of 5 or more.

The THz peak SNR corresponded largely to noise associated with the generation and propagation of the THz pulses. While the pre-noise also contributed to the noise on the THz peak, the THz peak noise was typically 10-100 times larger than the pre-noise. The primary source of this noise was found to be the stability of the laser. While the pre-noise did not depend on the power of each laser pulse, the measured

THz signal depended strongly on the power of the generation pulses, and therefore fluctuated strongly with any generation beam power fluctuations. We were able to reduce this noise in a number of ways to achieve an average SNR of about 500. First, we increased the generation beam intensity to a value just below the long-term damage threshold. While the peak THz electric field should normally scale with the power of the generation beam, this behavior saturated at high generation beam power, such that the THz peak electric field depended weakly on generation beam power, and thus the THz peak value fluctuated weakly with generation beam power fluctuations. Second, we prioritized ideal propagation of the THz pulses through the OAPM setup over the collinearity of the THz and detection pulses in the detection ZnTe crystal. This minimized the amount of clipping of the THz on the OAPMs, which we found decreased the THz peak noise. To achieve this, we first aligned the generation beam to the OAPM alignment irises, and then maximized the THz signal by adjusting the fourth OAPM alignment to optimize the THz and detection beam overlap, rather than optimizing the THz signal by adjusting the alignment of the generation beam into the OAPM system. Finally, we minimized the effects of long term drifts of the THz signal size by alternating between measurements of the sample and reference between scans. This allowed us to normalize each sample scan by the reference scan taken immediately after, eliminating the effects of laser power drifts that occurred over time scales longer than ~1 minute.

Other than statistical noise, it was important to reduce the effects of artifacts that introduced systematic errors to the measurement of material properties. The two largest sources of systematic errors were found to be insufficient isolation of the sample and reference materials and the inclusion of etalons in the scanned region. The sample and reference materials were typically mounted over identical holes separated by some distance drilled into a copper sample holder. Because the clipping on the OAPMs became severe at the lowest frequencies, the THz spot size on the sample became large ($\gg$1.5 mm) for the low-frequency end of the THz spectrum. If the sample and reference were placed too closely together, there was inevitably some leakage of THz through the reference hole, for instance, when the sample was being

measured. This caused systematic issues at low frequency that depended strongly on the precise sample alignment, and therefore did not divide out. To solve this issue, we mounted the sample and reference materials at least 6 mm apart, which was found to be a sufficient distance.

Ordinarily, the THz signal we measured was the direct transmission of the THz through the sample material. However, there also existed higher order internal reflections of the THz, called etalons, that appeared delayed in time. The first etalon, for instance, resulted from the transmission through the front sample interface, the reflection off the back interface, the reflection off the front interface, and finally the transmission through the back interface. Other etalons were also present due to the internal reflections of transmissive optics in the generation beam (appearing after the THz pulse in time) and the detection beam (appearing before the THz pulse in time). Including an etalon in the scanned region resulted in an oscillation in frequency space that would be incorrectly associated with the sample material response. A simple way to see this is to consider an etalon from the sample, which introduces a signal delayed in time by Δt and reduced in size by a factor α on top of the desired signal $E(t)$.

$$\begin{aligned} \mathscr{F}(E(t) + \alpha E(t - \Delta t)) &= \int_{-\infty}^{\infty} e^{2\pi i\omega t}(E(t) + \alpha E(t - \Delta t))dt \\ &= E(\omega)(1 + \alpha e^{-2\pi i\omega \Delta t}) \end{aligned} \tag{2.25}$$

As can be seen in equation 2.25, the inclusion of an etalon separated by the main THz signal by time Δt introduces an oscillation in the frequency domain with period $1/\Delta t$. To eliminate this problem, we ensured that all transmissive optics, including the sample, were thick enough (Δt large enough) to be able to entirely separate the desired THz waveform from the etalons. This allowed us to eliminate the etalons from the scanned region while still measuring the entirety of the THz waveform.

2.4 Conclusions

We have presented an optical technique called Terahertz Time-Domain Spectroscopy that enables the measurement of optical properties of materials at the meV energy scale, which is typically inaccessible due to the dearth of emitters, optics, and detectors in the THz energy range. THz-TDS uses second-order nonlinear processes to generate and detect pulses of THz in a phase-coherent way, allowing for the measurement of complex optical properties without the use of the Kramers-Kronig relations. THz-TDS is therefore ideal for studying systems with meV energy scales, such as superconductors, metals, gapped topological insulators, and spin liquid systems, as well as for studying the quasi-DC properties of systems on which it is difficult or impossible to make electrical contact. In chapter 4, we will apply THz-TDS to spin liquid candidate Herbertsmithite and find a signature for the nature of the spin liquid ground state in the THz conductivity.

Chapter 3

Terahertz Polarization Modulation Spectroscopy

In the previous chapter, we discussed THz TDS, with which polarization-preserving processes in materials can be probed. In general, however, a material's effect on incident light can change its polarization. For example, a material can exhibit linear dichroism (birefringence [79,89]), where different linear polarizations experience different index of refraction, or circular dichroism (usually the Hall effect [79,89]), in which different circular polarizations experience different index of refraction. In both these cases, the input THz polarization is not preserved, allowing the transmitted THz pulse to be, in general, elliptically polarized. Many systems of current scientific interest display this behavior, including systems displaying the Hall effect [90–93], quantum Hall effect [94–96], and topological systems displaying the classical and quantum anomalous Hall effect, such as topological insulators [97–99] and Weyl semimetals [100–102]. In order to study such systems, it is necessary to measure the time-resolved waveform of both linear components of the transmitted THz polarization.

In this chapter, we will present a technique called Terahertz Polarization Modulation Spectroscopy (TPMS), which will enable the measurement of both linear THz components simultaneously. Unlike similar techniques, such as magneto-optical Kerr measurements, which measure polarization angle by measuring the intensity of light after passing through a polarizer [103, 104], this technique is sensitive to both mag-

nitude and phase of the THz electric field, allowing for direct measurements of the frequency-dependent complex polarization. The simultaneous nature of the measurement allows for faster data collection with common-mode noise subtraction.

3.1 Optics at an interface with a Hall effect

In the previous chapter, we restricted ourselves to cases where the THz polarization is preserved when the THz transmits through a material. In the case of thin films, this restriction required the assumption that the surface current density $\vec{j}_s$ is proportional to the electric field driving it. In general, however, the conductivity can act as a tensor, giving

$$\vec{j}_s = \begin{pmatrix} \sigma_{xx} & \sigma_{yx} \\ \sigma_{xy} & \sigma_{yy} \end{pmatrix} \begin{pmatrix} E_x \\ E_y \end{pmatrix}, \tag{3.1}$$

where σ_{xx} is the longitudinal conductivity and σ_{xy} is the transverse conductivity, usually called the Hall conductivity [78, 79]. Since the polarization is not conserved, the Jones matrix for the material is in general a matrix, giving

$$\vec{E}_t = \begin{pmatrix} T_{xx} & T_{yx} \\ T_{xy} & T_{yy} \end{pmatrix} \vec{E}_i. \tag{3.2}$$

As in the previous chapter, one must model the transmission matrix T as a function of the physical material properties, and then perform sufficient measurements of the THz waveforms through a sample and reference material to obtain a measurement of these properties.

We will first discuss how to model the transmission coefficient. We will restrict ourselves to the case of a thin film on a thick substrate with index of refraction n_s and thickness l_s, as in Figure 2.5b, and assume that the film and substrate are isotropic, such that $\sigma_{xx} = \sigma_{yy}$ and $\sigma_{xy} = -\sigma_{yx}$. We must consider the full vector form of the

boundary conditions at the first interface:

$$\begin{aligned}\vec{E}_i + \vec{E}_r &= \vec{E}_t \\ \vec{B}_i + \vec{B}_r &= \vec{B}_t + \mu_0(\hat{n} \times \vec{j}_s),\end{aligned} \tag{3.3}$$

where $\hat{n}$ is the thin film surface normal vector, which we will take to be $-\hat{z}$. Assuming a plane wave form where $\hat{k} \times \vec{B} = \frac{n}{c}\vec{E}$, and plugging formula 3.1 into formula 3.3 gives

$$\begin{aligned}\vec{E}_i + \vec{E}_r =& \vec{E}_t \\ \vec{E}_i - \vec{E}_r =& n_s\vec{E}_t + Z_0 d(\sigma_{xx}E_{tx} + \sigma_{yx}E_{ty})\hat{x} + \\ & Z_0 d(-\sigma_{yx}E_{tx} + \sigma_{xx}E_{ty})\hat{y}.\end{aligned} \tag{3.4}$$

Taking the sum of these equations and assuming an incident polarization $\vec{E}_i = E_i\hat{x}$, we get

$$\begin{aligned}0 &= (1 + n_s + Z_0 d\sigma_{xx})E_{ty} - Z_0 d\sigma_{yx}E_{tx} \\ 2E_i &= (1 + n_s + Z_0 d\sigma_{xx})E_{tx} + Z_0 d\sigma_{yx}E_{ty}.\end{aligned} \tag{3.5}$$

The first formula gives the output polarization angle $\Theta(\omega)$:

$$tan(\Theta(\omega)) \equiv \frac{E_{ty}}{E_{tx}} = \frac{Z_0 d\sigma_{yx}}{1 + n_s + Z_0 d\sigma_{xx}}, \tag{3.6}$$

while the second formula, after plugging in the first formula and accounting for the propagation through the substrate and transmission through the back interface, gives the transmission coefficients

$$\begin{aligned}T_{xx,s} = \frac{E_{tx}}{E_i} &= \frac{4n_s exp(in_s\omega l_s/c)}{n_s + 1}\frac{(1 + n_s + Z_0 d\sigma_{xx})}{(1 + n_s + Z_0 d\sigma_{xx})^2 + (Z_0 d\sigma_{yx})^2} \\ T_{yx,s} =& T_{xx,s}tan(\Theta(\omega)).\end{aligned} \tag{3.7}$$

As in the previous chapter, we must normalize the transmission coefficient by a reference transmission coefficient to be able to equate the calculated coefficient to the ratio of measured THz waveforms. In this case, we will use a bare substrate with thickness

$l_r = l_s + \delta l$, which preserves the THz polarization. The transmission coefficient for the reference is given by formula 2.19. We then arrive at the final result:

$$\begin{aligned} T_{xx} = \frac{E_{s,x}(\omega)}{E_r(\omega)} = \frac{T_{xx,s}}{T_r} &= \frac{n_s + 1}{exp(in_s\omega\delta l_s/c)} \frac{(1 + n_s + Z_0 d\sigma_{xx})}{(1 + n_s + Z_0 d\sigma_{xx})^2 + (Z_0 d\sigma_{yx})^2} \\ T_{yx} &= \frac{E_{s,y}(\omega)}{E_r(\omega)} = T_{xx} tan(\Theta(\omega)), \end{aligned} \tag{3.8}$$

where $E_{s,x}(\omega)$, $E_{s,y}(\omega)$, and $E_r(\omega)$ are the Fourier transforms of the measured THz waveforms through the sample in the $\hat{x}$ and $\hat{y}$ directions and through the reference, respectively. We have therefore shown that the measurement of both polarization components of the THz waveform after transmission through a thin film sample, along with the measurement of the THz waveform after transmission through a polarization conserving reference, provides a direct measurement of both the longitudinal conductivity σ_{xx} and the transverse (Hall) conductivity σ_{yx} at THz frequencies.

3.2 Polarization measurements using a fast-rotating polarizer

There are a number of techniques that could be used to measure both linear polarization components of the THz pulses after transmission through a sample. The simplest method is to polarize the THz in, say, the $\hat{x}$ direction before the sample, and then to perform two experiments: polarize the THz again in the $\hat{x}$ direction after the sample to measure T_{xx}, then polarize the THz in the $\hat{y}$ direction after the sample to measure T_{yx}. We will use the Jones matrix formalism to understand this setup. The Jones matrix for a polarizer aligned at angle θ relative to the x-axis is [84]

$$P(\theta) = \begin{pmatrix} cos^2(\theta) & cos(\theta)sin(\theta) \\ cos(\theta)sin(\theta) & sin^2(\theta) \end{pmatrix}. \tag{3.9}$$

For a sample transmission coefficient T given by formula 3.2, the final THz polarization is given by

$$\begin{pmatrix} E_{fx}(\omega) \\ E_{fy}(\omega) \end{pmatrix} = P(0) \cdot T \cdot P(0) \cdot \begin{pmatrix} E_{ix}(\omega) \\ E_{iy}(\omega) \end{pmatrix} = \begin{pmatrix} T_{xx}E_{ix}(\omega) \\ 0 \end{pmatrix} \tag{3.10}$$

or

$$\begin{pmatrix} E_{fx}(\omega) \\ E_{fy}(\omega) \end{pmatrix} = P(\pi/2) \cdot T \cdot P(0) \cdot \begin{pmatrix} E_{ix}(\omega) \\ E_{iy}(\omega) \end{pmatrix} = \begin{pmatrix} 0 \\ T_{yx}E_{ix}(\omega) \end{pmatrix}. \tag{3.11}$$

While this method is sufficient to obtain the desired quantities, it has several down sides. First, each measurement must be taken separately, allowing for errors due to the drift of the THz signal with time. Additionally, common-mode noise subtraction techniques cannot be utilized. Second, this technique relies on polarizers that have a perfect extinction ratio. While commercially available wire-grid polarizers can achieve extinction ratios of around 10^{-2} in the THz range, systematic errors become severe when attempting to measure polarization angles around 10 *mrad*. Finally, the measured THz polarization differs by $\pi/2$ between the two measurements. As discussed in the previous chapter, the THz detection efficiency depends on the relative angle between the THz polarization, the detection pulse polarization, and the detection crystal orientation. In order to compare the results of these two measurements, a constant detection efficiency must be maintained. To achieve this, both the detection polarization and detection crystal must be rotated by $\pi/2$ when switching between the two measurements. This invites further opportunity for error if the relative angles are not repoduced exactly.

To resolve these issues, we have utilized the technique of C. M. Morris *et al.* [105], in which a fast-rotating polarizer is placed directly after the sample (Figure 3.1). We will refer to this technique as Terahertz Polarization Modulation Spectroscopy (TPMS). The Jones matrix for a polarizer rotating at angular frequency Ω is

$$P_{\Omega}(t_r) = \begin{pmatrix} cos^2(\Omega t_r) & cos(\Omega t_r)sin(\Omega t_r) \\ cos(\Omega t_r)sin(\Omega t_r) & sin^2(\Omega t_r) \end{pmatrix}, \tag{3.12}$$

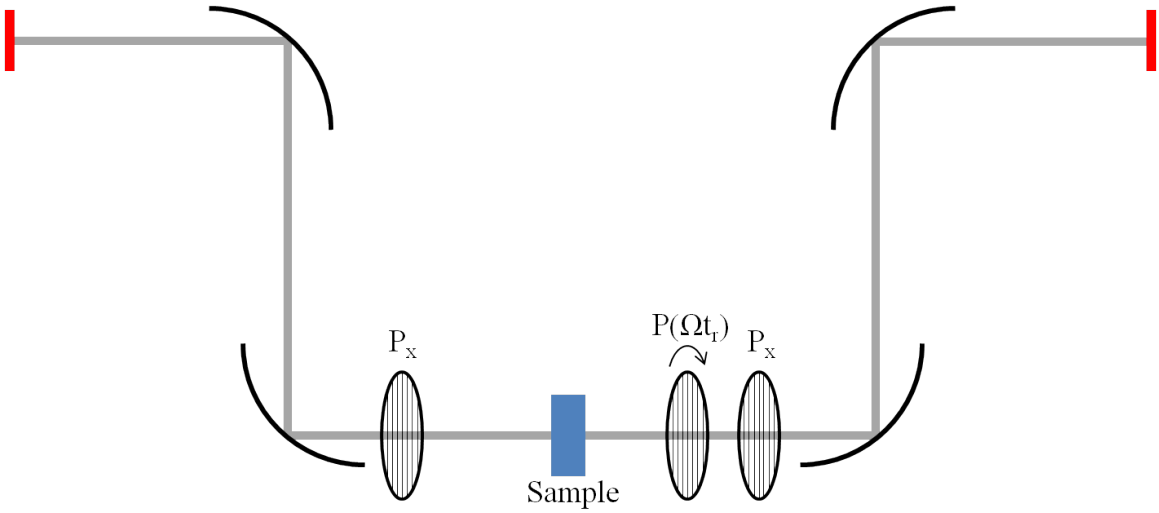

Figure 3.1: Desired optical setup for measuring T_{xx} and T_{yx} simultaneously. The THz is polarized in the $\hat{x}$ direction before transmitting through the sample. It then passes through a polarizer rotating at angular frequency Ω before being polarized again in the $\hat{x}$ direction.

where t_r is the time that determines the instantaneous phase of the rotating polarizer. In this technique, we will fix both static polarizers in the $\hat{x}$ direction, giving the final THz polarization:

$$\begin{aligned}\begin{pmatrix} E_{fx}(t_r,\omega) \\ E_{fy}(t_r,t) \end{pmatrix} &= P(0)\cdot P_\Omega(t_r)\cdot T\cdot P(0)\cdot \begin{pmatrix} E_{ix}(\omega) \\ E_{iy}(\omega) \end{pmatrix} \\ &= \begin{pmatrix} E_{ix}(\omega)(cos^2(\Omega t_r)T_{xx} + sin(\Omega t_r)cos(\Omega t_r)T_{yx}) \\ 0 \end{pmatrix} \\ &= \begin{pmatrix} \frac{E_{ix}(\omega)}{2}((cos(2\Omega t_r)+1)T_{xx} + sin(2\Omega t_r)T_{yx}) \\ 0 \end{pmatrix}.\end{aligned} \tag{3.13}$$

We have now obtained a final THz electric field that is modulated at frequency 2Ω with two completely out-of-phase components that are proportional to T_{xx} and T_{yx}, respectively. To separate these two signals, the measured THz signal is typically sent to a lock-in amplifier with a reference signal at 2Ω phase locked with the rotation of the polarizer. In the next section, we will present a different way to separate the two signals using a DAQ card. The x and y channels of the lock-in amplifier measure,

respectively:

$$S_x(t) \propto \frac{1}{\tau}\int_0^\tau E_{fx}(t_r,t)cos(2\Omega t_r)dt_r \tag{3.14}$$

$$S_y(t) \propto \frac{1}{\tau}\int_0^\tau E_{fx}(t_r,t)sin(2\Omega t_r)dt_r, \tag{3.15}$$

where τ is the time constant of the lock-in, which is preferably chosen to be an integer multiple of the period of the rotating polarizer. The proportionality takes into account the proportionality of the detector response to the THz electric field, which is the same for each channel. The Fourier transform of formula 3.14 gives:

$$S_x(\omega) \propto \frac{1}{\tau}\int_0^\tau E_{fx}(t_r,\omega)cos(2\Omega t_r)dt_r. \tag{3.16}$$

Plugging formula 3.13 into formula 3.16 gives

$$S_x(\omega) \propto \frac{1}{\tau}\int_0^\tau \frac{E_{ix}(\omega)}{2}((cos^2(2\Omega t_r)+cos(2\Omega t_r))T_{xx}+sin(2\Omega t_r)cos(2\Omega t_r)T_{yx})dt_r. \tag{3.17}$$

If τ is a multiple of π/Ω, most of these terms integrate out, giving

$$S_x(\omega) = \frac{R(\omega)}{4}E_{ix}(\omega)T_{xx}(\omega), \tag{3.18}$$

where $R(\omega)$ takes into account the detector response to the THz electric field. The same treatment applied to formula 3.15 gives the y channel response:

$$S_y(\omega) = \frac{R(\omega)}{4}E_{ix}(\omega)T_{yx}(\omega). \tag{3.19}$$

When measuring these signals using a hardware lock-in amplifier, τ typically can only be set to certain predefined values, which in general are not multiples of the rotating polarizer period. In this case, the sinusoidal terms in formula 3.17 do not exactly integrate out. They instead integrate to a term proportional to $1/(\Omega\tau)$ that oscillates in time. This necessitates a large value of τ to reduce this unwanted signal, making data collection slow. In the next section of this chapter, we will describe a method using a DAQ card with software integration in place of a lock-in amplifier, allowing

us to choose the precise value of τ to be a multiple of the polarizer period.

We have now shown that with a fast rotating polarizer, it is possible to measure a signal proportional to T_{xx} and T_{yx} simultaneously, with a fixed detected THz polarization direction. The THz polarization angle $tan(\Theta(\omega)) = S_y(\omega)/S_x(\omega)$ can therefore be obtained with a single measurement, with the common noise of the two signals being directly cancelled by the division. Additionally, this technique further improves upon the previously mentioned geometry in that the extinction ratio of the spinning polarizer has no effect on the measured polarization angle. To see this, we consider the Jones matrix for a polarizer with extinction ratio ϵ, defined to be the ratio of transmitted electric field when the polarizer is parallel to, and perpendicular to, the linear THz polarization [84].

$$P_\epsilon(\theta) = \begin{pmatrix} cos^2(\theta) + \epsilon sin^2(\theta) & (1-\epsilon)cos(\theta)sin(\theta) \\ (1-\epsilon)cos(\theta)sin(\theta) & \epsilon cos^2(\theta) + sin^2(\theta) \end{pmatrix} \tag{3.20}$$

Using this matrix for the spinning polarizer and following the same procedure as before gives:

$$\begin{aligned} S_x(\omega) &= \frac{R(\omega)}{4}(1-\epsilon)E_{ix}(\omega)T_{xx}(\omega) \\ S_y(\omega) &= \frac{R(\omega)}{4}(1-\epsilon)E_{ix}(\omega)T_{yx}(\omega). \end{aligned} \tag{3.21}$$

The measured lock-in signal is simply reduced by a factor of $1-\epsilon$ in both channels, so the measured polarization angle $tan(\Theta(\omega)) = S_y(\omega)/S_x(\omega)$ is preserved. Unfortunately, imperfections in the fixed polarizers do indeed mix the T_{xx} and T_{yx} components, resulting in a systematic error in the measured polarization angle, but as we will show later in this chapter, this background signal can be subtracted out with a reference polarization angle subtraction as long as the background angle is small.

3.3 Implementation of TPMS in the Gedik lab

In this section, we will present details on the implementation of TPMS in the Gedik lab. The primary challenges were the design and construction of the fast-rotating polarizer, and the development of data acquisition and processing tools to enable the implementation of a DAQ card-based measurement scheme. Our DAQ card implementation provided a number of advantages over the lock-in amplifier-based implementation of reference [105], including the precise control of the integration time constant τ, as mentioned in the previous section, and the ability to easily extend the technique to pump-probe experiments, allowing for the simultaneous measurement of unpumped polarization angle and the change in the polarization angle due to an optical excitation of a material. This will allow for the study of pump-induced linear and circular dichroism.

3.3.1 Fast-rotating polarizer

The creation of a rotating polarizer that met the desired speed and stability requirements posed a significant engineering challenge. We required a hollow spindle capable of holding a 2 inch diameter wire-grid polarizer, with rotation frequency $2\Omega = 50\ Hz$ and frequency stability such that the instantaneous angle of the polarizer at no point deviated from the desired instantaneous angle by more than 0.5 $mrad$, as will be discussed later in this section. We also required that the mechanical motion of the spindle did not introduce too much noise into the THz generation and detection system, and that the centripetal forces on the wire-grid polarizer did not cause damage. Furthermore, the spindle had to be constructed of sufficiently non-magnetic materials, due to its proximity to a superconducting magnet used for Faraday effect measurements. More information on the magnetic cryostat will be presented in the next subsection. Finally, we required the spindle to have a compact size in order to fit in our pre-existing THz optical setups.

The physical construction of such a spindle fell well outside the expertise of our group. Instead, we worked with HPT Precision Spindles and Drives, Inc., to design

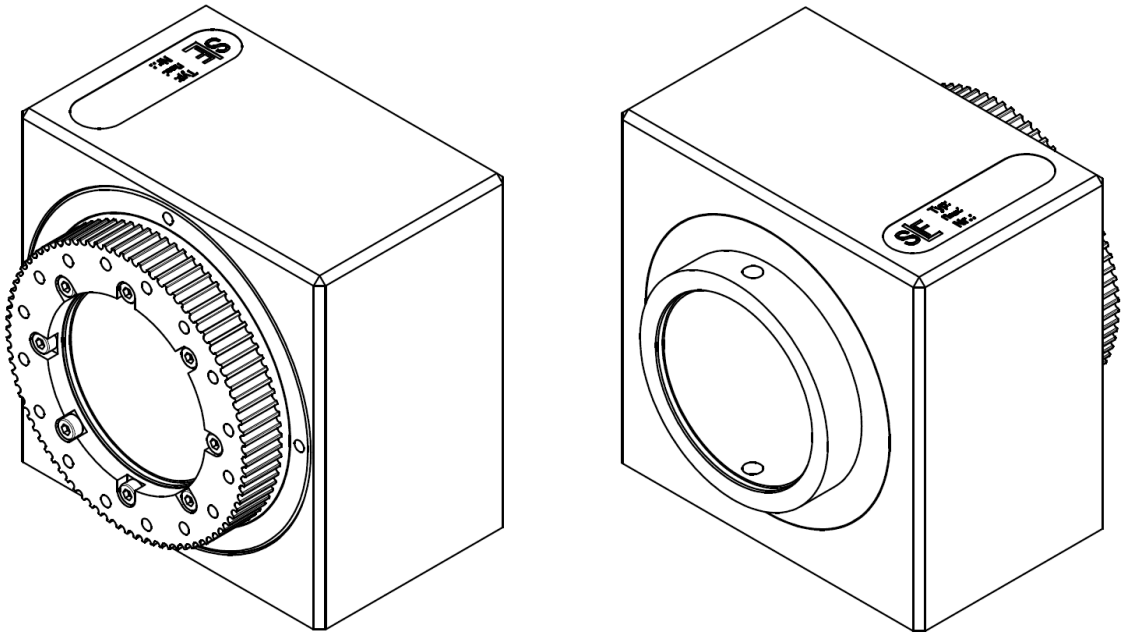

Figure 3.2: A drawing of the final spindle design. A 2 inch inner diameter SM2 threaded tube was used to hold a 2 inch diameter wire-grid polarizer. One end featured a no-slip gear to couple the spindle to a programmable motor via a toothed kevlar belt. The other end featured a radial through-hole. A CW laser was passed through the through-hole and measured with a photodiode to directly obtain a measurement of twice the spindle rotational frequency.

and build the spindle. A drawing of the final spindle design can be seen in Figure 3.2. The spindle was constructed entirely out of aluminum, wiht the exception of the bearings, which were constructed out of weakly-magnetic steel. The central axis of the spindle featured a 2 inch diameter SM2 threaded hole within which a 2 inch diameter wire-grid polarizer could be mounted using two retaining rings. One end of the spindle featured a ~3 inch diameter no-slip gear, allowing the spindle to be attached to a programmable motor via a toothed kevlar belt and an identical motor gear. Since precise measurements of the spindle rotational frequency were required, we devised a method for directly measuring twice the rotational frequency 2Ω, as discussed in the previous section. A radial through-hole was drilled in other end of the spindle. A CW laser was sent through this through-hole and measured with a photodiode. While the spindle was spinning, the photodiode measured a signal twice

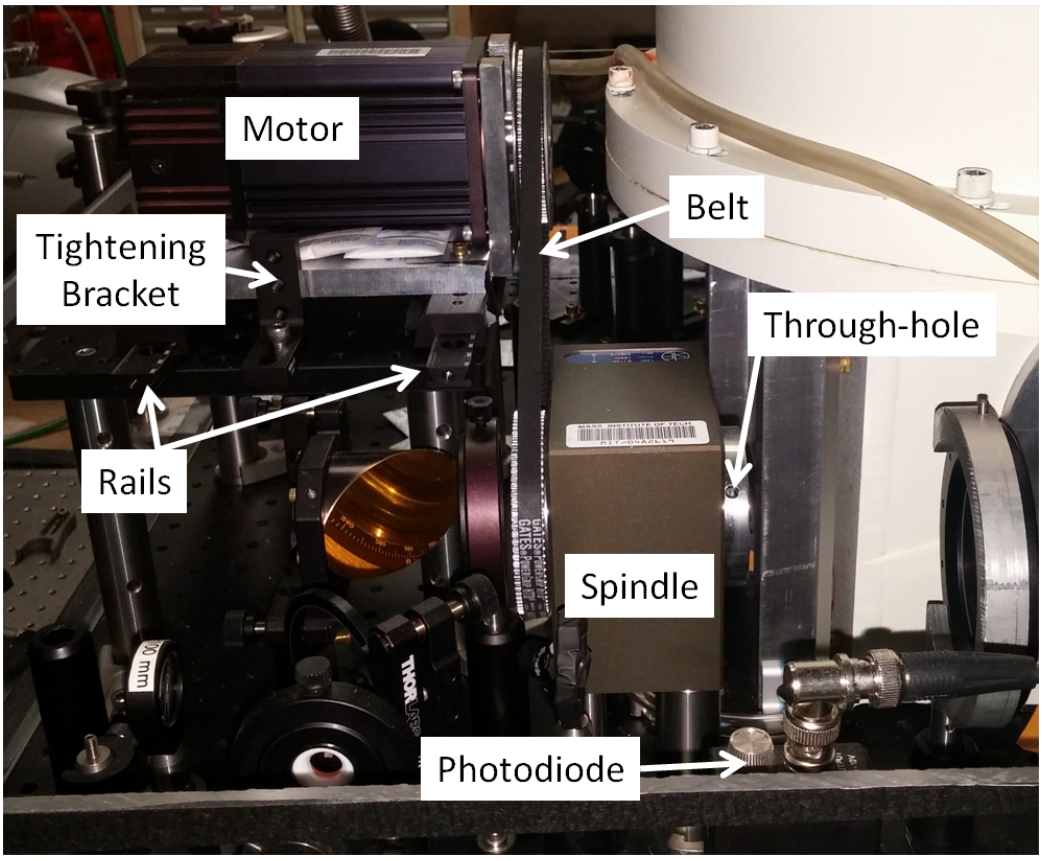

Figure 3.3: A photograph of the rotating spindle setup next to the superconducting magnetic cryostat. The spindle belt was tightened by turning a screw in the tightening bracket, allowing the motor to slide along the parallel rails. The spindle rotational frequency was measured by sending a CW laser through the radial through-holes on the spindle and onto a photodiode.

per rotation of the spindle, allowing us to obtain a phase-sensitive measurement of 2Ω directly.

To drive the spindle, we used a Moog Animatics SM34505D smartmotor. This motor was capable of providing 261 *oz-in* of continuous torque, and 711 *oz-in* of peak torque, which proved to be sufficient for operating the spindle at $2\Omega = 50\ Hz$. We machined a custom bracket to hold the motor and rigidly connect it to a pair of parallel aluminum rails. The kevlar belt was attached to the spindle and motor gears, and then the belt was tightened by sliding the motor along the parallel rails by tightening a screw in a bracket next to the motor bracket. Sufficient tightening of the spindle belt was found to be crucial in stabilizing the spindle frequency. If the belt

was too loose, vibrations were launched in the belt, resulting in rotational frequency noise that could not be stabilized with a PID loop. A photograph of the spindle and motor in the THz setup can be seen in Figure 3.3.

The motor included its own hardware PID controls, with user customizable settings to maximize the stability. We operated the motor in "velocity mode", which compared the absolute position of the motor to the expected position assuming a constant preset velocity and adjusted the instantaneous velocity appropriately to correct any measured position errors. We calibrated the velocity-to-frequency ratio by comparing the motor read velocity to the frequency measured by the CW laser that passed through the radial through-hole on the spindle. We then divided the 5 kHz amplifier reference signal by a factor of 100 using a frequency divider circuit to obtain a 50 Hz signal that was phase-locked to the laser trigger. We adjusted the velocity set point until the measured spindle frequency and 50 Hz laser reference were identical. In this way, we were able to passively phase-lock the spindle rotation to the amplifier repetition rate, the importance of which will be explained later in this section. This passive phase-locking technique was required because there was no way to actively trigger the spindle motor off of the laser trigger. The passive technique proved to be sufficient, however, because the extreme stability of the spindle frequency allowed for a constant phase difference between the spindle frequency signal and the 50 Hz laser reference for many hours.

3.3.2 Experimental setup and alignment

We have primarily developed our TPMS setup around a superconducting magnet cryostat in order to enable Hall or even quantum Hall measurements. While we can also perform TPMS measurements in the THz setup described in the previous chapter, such measurements are limited to probing static linear dichroism and pump-induced dichroism. In this section, we will focus on the magnet setup. A diagram of the THz setup built around the magnet can be seen in Figure 3.4. While this setup is similar to the one described in the previous chapter, the large size of the magnet required longer focal length OAPMs, specifically 9.5", 7.5", 7.5", and 7", respectively. Due to space

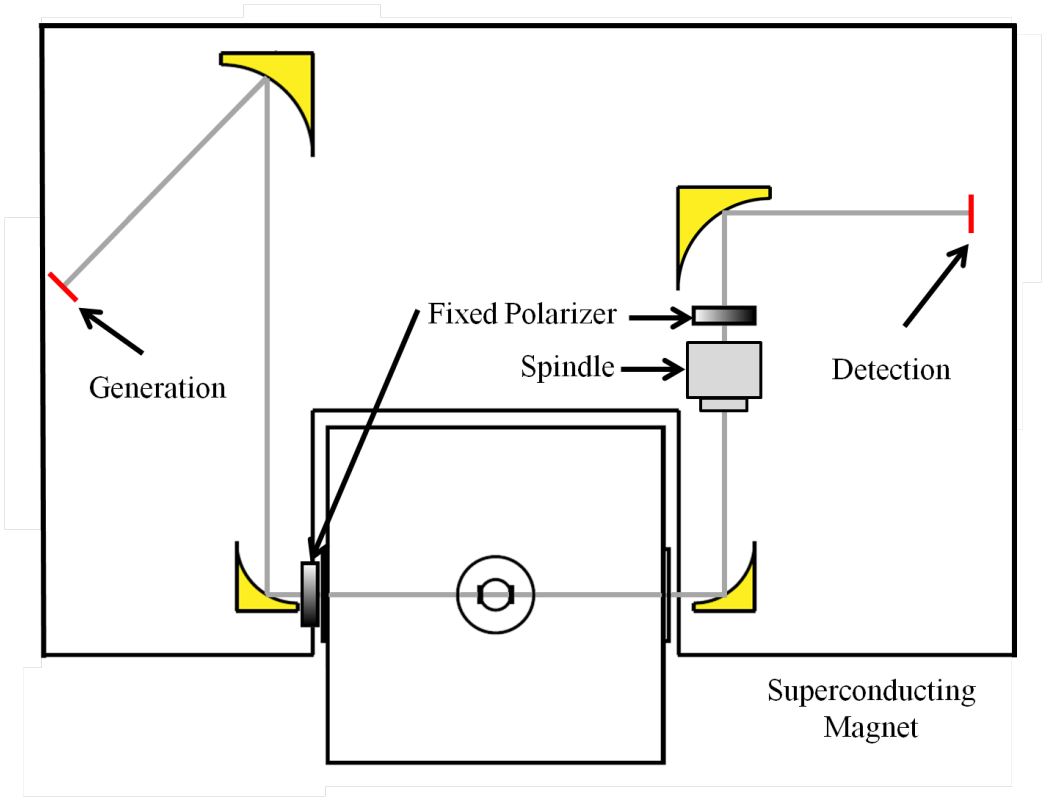

Figure 3.4: A schematic of the TPMS setup built around a superconducting magnetic cryostat. The spindle and 2nd fixed polarizer had to be placed after the 3rd OAPM, which contributed a systematic polarization error.

constraints, we used a 45° OAPM for the first mirror. Unlike the ideal case shown in Figure 3.1, the spindle and second fixed polarizer had to be placed in between the 3rd and 4th OAPM due to space constraints, which introduced systematic errors in the measured THz polarization due to depolarizing effects of the 3rd OAPM, which will be further discussed later in this section.

The THz setup was aligned on a breadboard which was mounted on a home-built platform constructed from 2 inch black anodized aluminum extrusions (80-20, Inc.). The platform height was designed such that the THz beam height matched the height of the magnetic cryostat windows. The sturdy construction combined with the ability to bolt the platform to the table in multiple places helped reduce the mechanical noise introduced by the rotating spindle. Additionally, the platform made contact with the breadboard along its entire perimeter, ensuring that the breadboard did not sag over time. The entire THz beam path was enclosed in a box similar to the one described

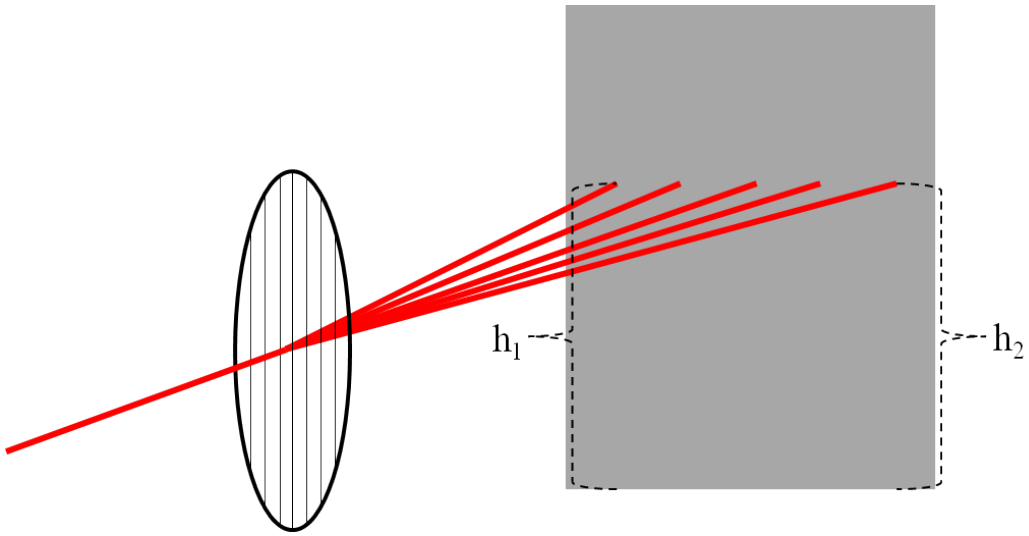

Figure 3.5: Alignment of the fixed wire-grid polarizers. A red CW laser is aligned parallel to the optics table and is diffracted off the polarizer. The diffracted spots form a line perpendicular to the polarizer wires. The polarizer is rotated until the left- and right-most diffracted spot are the same height from the optics table. When this is the case, the polarizer is aligned to transmit x-polarized THz, as desired.

in the previous chapter, which was purged with dry air to a relative humidity of 0.5% to reduce water absorption effects.

It was crucial for the proper interpretation of data to align the two fixed wire-grid polarizers such that their wires were precisely vertically aligned. Any relative angle between the two fixed polarizers would result in an error in the measured THz polarization. Furthermore, an error in their absolute angle increased the depolarization effects of the 3rd OAPM, because the two linear polarization components would no longer be parallel or perpendicular to the optical plane. In order to achieve precise alignment of the polarizers, we diffracted a red CW laser off of each polarizer, as shown in Figure 3.5. The many diffraction orders coming from the polarizer spread out in a direction perpendicular to the polarizer wires, regardless of the alignment of the laser into the polarizer. We then rotated the polarizer until the line of diffracted spots was parallel with the optical table, which we ensured by checking the height of each diffracted spot with an iris. With this technique, we were able to align the polarizers with sub *mrad* resolution.

A wire-grid polarizer was mounted in the spindle with a pair of SM2 retaining

rings, and the spindle was placed in the THz path between the 3rd and 4th OAPM such that it did not clip the THz beam. A CW laser beam from a red laser diode was aligned through the spindle through-holes and detected via a photodiode. The laser passed through the holes twice per rotation of the spindle, resulting in a photodiode signal at frequency 2Ω. The photodiode signal was then set to a lock-in amplifier to convert the signal to a sinusoid that was phase locked to the input signal. This sinusoidal signal, along with the 5 kHz laser trigger, was then sent to the computer via the DAQ card.

3.3.3 Data acquisition

Earlier in this chapter, we showed that it was possible to measure both THz polarization components simultaneously using a rotating spindle and lock-in amplifier. The use of the lock-in amplifier came with a few disadvantages, including the requirement of a long time constant τ and the inability to perform chopped experiments as in formula 2.22. To solve these issues, we used a DAQ card for data collection, similar to the technique described in the previous chapter, with the ultimate goal of reproducing the lock-in output given by formulas 3.14 and 3.15 using software discrete math techniques.

In the previous chapter, we recorded the peak of each detection photodiode signal, starting after the trigger from a synchronized optical chopper operating at half the laser repetition rate. We were then able to record a signal proportional to the THz electric field by using formula 2.22. Similarly in this technique, we recorded a series of 500 detection diode signal peaks after the triggering of a 50 Hz reference signal obtained by dividing the laser trigger frequency by a factor of 100 using a frequency divider chip. In order to synchronize the spindle frequency with the 50 Hz laser trigger, we recorded the signal from the spindle diode mentioned in the previous subsection along with the THz detection diode signals, and adjusted the spindle motor set velocity until the relative phase of the spindle diode signal and the 50 Hz laser trigger signal remained constant for many hours. We were able to achieve this level of spindle frequency stability by operating the motor in "velocity mode"

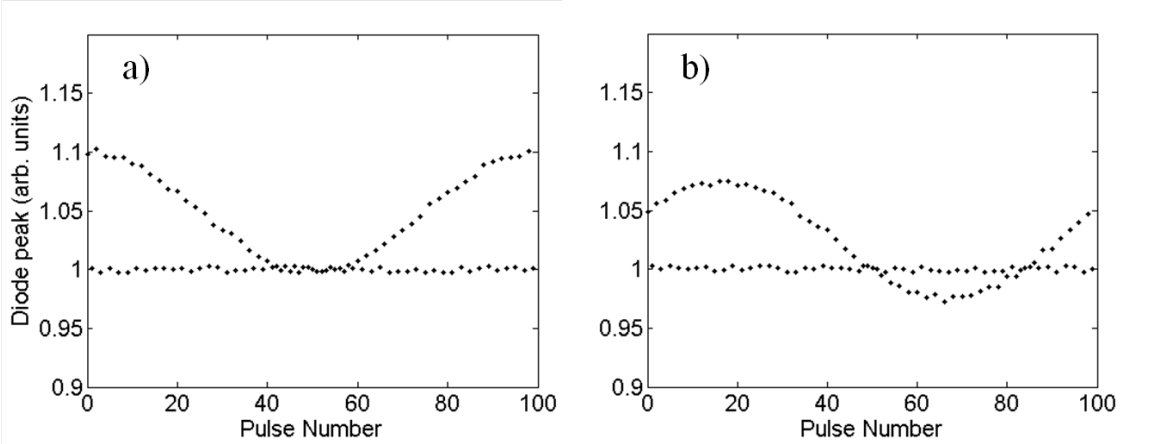

Figure 3.6: Simulated TPMS data taken over 1 period of the spindle rotation on one of the detection photodiodes at a specific detection beam time delay. Each diode peak signal was measured, with THz being present for every odd pulse. Subsequent even and odd pulses were divided to divide out long term drift in the photodiode signal. a) Example data for a THz pulse with instantaneous electric field in the $\hat{x}$ direction. b) Example data for a THz pulse with instantaneous electric field at an angle of $\pi/3$ relative to the $\hat{x}$ direction.

and adjusting the motor PID settings to maximize velocity stability. Since "velocity mode" compared the absolute position of the motor with the predicted position given by the velocity set point and then adjusted the instantaneous velocity accordingly, any noise in the instantaneous phase of the spindle was averaged out, rather than compounded. In this way, as long as the velocity set point was optimized sufficiently, the instantaneous spindle phase error did not grow with time. The THz generation beam was also chopped at 2.5 kHz, synchronized with the 5 kHz laser trigger.

After the trigger from the 50 Hz laser trigger, we recorded both detection photodiode signals as well as the spindle photodiode signal at times corresponding to the next 500 trigger events from the 5 kHz laser trigger, delayed by the DDG to correspond with the peaks of the THz detection photodiodes. These 500 pulses corresponded to 5 periods of the spindle rotation. Since the spindle and chopper rotations were locked with the laser repetition rate, the first pulse measured always corresponded to a pulse where the generation beam was blocked, or unblocked. We then obtained the

modulated THz signal by using a balanced and chopped scheme given by

$$\frac{1}{2}\left(\frac{A_1}{A_2}-\frac{B_1}{B_2}\right)=\frac{1}{2}\left(\frac{I+\Delta I(t_r)}{I}-\frac{I-\Delta I(t_r)}{I}\right)=\frac{\Delta I(t_r)}{I}\propto E_{THz}(t_r), \tag{3.22}$$

where A_1, A_2, B_1, and B_2 correspond to the first and second pulses in each pair of even and odd pulses measured by diode A and B, respectively, and t_r is the time corresponding to the rotation of the spindle. We therefore obtained a measurement proportional to the component of the THz electric field along the spindle polarizer orientation at time t_r over 5 periods of the rotation of the spindle, with a starting point corresponding to a specific orientation of the spindle polarizer. Figure 3.6 shows a schematic of this measurement process. The synchronization of the spindle to the 50 Hz laser trigger was crucial for this step, since, due to the discrete nature of the measured diode signals, there was no absolute time axis. If the first measured diode peak did not occur the same amount of time after the 50 Hz laser trigger for each set of 500 pulses measured, there would be a time uncertainty of up to 200 μs in the discrete time axis, corresponding to the period of the 5 kHz laser repetition rate. This error corresponded to a spindle phase uncertainty of 10 $mrad$, and hence an uncertainty in the THz polarization angle by 10 $mrad$. By synchronizing the spindle to the laser, however, this uncertainty was eliminated.

Once we had obtained the modulated THz electric field measurements, we had to separate the two polarization components by performing the lock-in integration given by formulas 3.14 and 3.15. To perform this integral using discrete math techniques, we took the Fourier transform of the modulated THz signal.

$$\begin{aligned} S_x(t,\omega_r)+iS_y(t,\omega_r) &\propto \frac{1}{\tau}\int_0^{\tau} E_{THz}(t_r,t)(cos(\omega_r t_r)+isin(\omega_r t_r))dt_r \\ &\propto \mathscr{F}_{\omega_r}(E_{THz}(t_r,t)) \end{aligned} \tag{3.23}$$

We then set ω_r equal to the spindle modulation frequency 2Ω by finding the value of formula 3.23 at the frequency corresponding to the peak of the magnitude of the Fourier transform of the spindle reference signal. Finally, the phase of the measured signal was set relative to the spindle reference phase by subtracting the spindle refer-

ence phase from the THz Fourier transform phase, and then adding a phase constant that accounted for the orientation of the spindle polarizer relative to the through-holes. Setting the phase this way ensured that any small change in the spindle starting phase relative to the 50 Hz laser trigger would not result in a change in the measured THz polarization. The real component of this signal was therefore equivalent to the x-channel of a lock-in measurement, and the imaginary part was equivalent to the y-channel. To calibrate this phase correction, we temporarily placed a fixed wire-grid polarizer aligned to transmit x-polarized THz directly before the spindle, ensuring that we were measuring a linearly polarized THz pulse. We then adjusted the phase correction until the signal fell entirely in the x-channel. After this calibration, THz signal measured in the x-channel corresponded to the component of the THz electric field along the $\hat{x}$ direction, while signal in the y-channel corresponded to the component of the THz electric field along the $\hat{y}$ direction.

As in the previous chapter, the THz pulses were mapped out in time by varying the relative time delay of the THz and detection pulses in the ZnTe crystal. The pulses measured in the two simulated lock-in channels were then Fourier transformed to obtain $S_x(\omega)$ and $S_y(\omega)$, giving the frequency-dependent polarization angle $tan(\Theta(\omega)) = \frac{S_y(\omega)}{S_x(\omega)}$. In general, real values of Θ corresponded to rotations of the principle axis of the elliptical polarization relative to the x-axis, while imaginary values corresponded to a relative phase shift between the two linear components. For example, if $\Theta = \pi/2 + 0 * i$, the polarization is linear along the y-axis. If $tan(\Theta) = i$, the polarization is right-handed circular.

3.3.4 Noise and systematic errors

There were several sources of noise and systematic error that needed to be addressed in order to properly understand the TPMS data. Typical measurements involved the measurement of a small polarization rotation angle, making the dynamic range of the $S_x(t)$ signal the limiting noise factor. For a small angle Θ and a dynamic range of D in the S_x channel, the dynamic range of the S_y channel is $Dsin(\Theta) \approx D\Theta$. Our goal was to achieve accurate measurements of angles as small as 0.5 $mrad$, which reduced

the S_y dynamic range by a factor of 2000 relative to S_x. It was critical, therefore, to maximize the size of the measured THz signal in the S_x channel and minimize the pre-noise. To achieve this, we used the maximum generation beam intensity that would not lead to damage of the ZnTe generation crystal. Additionally, we used a shorter focal length for the 4th OAPM ($f = 7"$), which focused the THz pulse to a tighter spot, resulting in a larger THz electric field at the center of its Gaussian profile. We minimized the pre-noise using the techniques outlined in the previous chapter.

Systematic errors were also significant, especially when measuring small polarization angles. Due to space limitations, we were forced to place the spindle and last fixed polarizer between the 3rd and 4th OAPM, rather than directly after the sample. This introduced a background polarization angle induced by depolarizing effects of the 3rd OAPM. Additionally, when performing experiments on samples in a magnetic field, additional polarization rotation was observed due to the induced Hall effect in the magnetic cryostat windows. Techniques for subtracting out these systematic errors had to be developed in order to be able to attribute any polarization rotation to the sample itself. Since rotations of the THz polarization involve a rotation in the 2 dimensional plane perpendicular to the wavevector $\vec{k}$, all Jones matrices leading to polarization rotation commute, as long as the polarization rotation is independent of initial THz polarization direction. This is a reasonable assumption in most cases, since the dominant background angle was typically due to Faraday rotation in the tranmissive optics, which inherently lead to a rotationally symmetric Jones matrix. In this case, the background polarization angle could simply be subtracted out by subtracting the measured polarization angle after transmitting through a reference material from the angle measured after transmitting through the sample. The depolarizing effects of the 3rd OAPM, however, were in general anisotropic, but this effect was small for small polarization rotations, since the THz polarization stayed nearly x-polarized throughout the whole optical setup. While a reference subtraction is sufficient to subtract out the background angle, it was also beneficial to perform symmetrization techniques when performing magnetic field-dependent measurements.

The polarization angle $\Theta(B)$ was measured at positive and negative field values of the same magnitute. The polarization rotation that depended linearly on B could then be separated from the field-independent response by symmetrizing and antisymmetrizing the data. The field-dependent contribution was given by $\frac{1}{2}(\Theta(B)-\Theta(-B))$ while the field-independent contribution was given by $\frac{1}{2}(\Theta(B)+\Theta(-B))$. For best results, we performed these data symmetrization operations after subtraction of a reference angle.

3.4 Pump-probe polarization rotation measurements

The DAQ card implementation of TPMS provided additional benefits beyond noise subtraction. In pump-probe experiments, it also enabled the possibility of simultaneously measuring the polarization rotation due to the static properties of a material, and the change in the rotation after photoexcitation. This ability could prove quite useful for studying Weyl semimetals, in which a photo-induced anomalous Hall effect is predicted [106], as well as in studying floquet effects in topological insulators and graphene, in which an anomalous Hall effect is predicted to appear upon the opening of a gap at the Dirac point [72, 107–110]. While pump-probe polarization measurements are possible with the use of two lock-in amplifiers, such measurements typically only provide the change in the rotated polarization, requiring the measurement of static properties to be performed separately, which introduces the possibility of errors due to signal drift.

In order to perform pump-probe experiments using our DAQ card technique, the THz generation beam and pump beam must both be chopped synchronously with the laser repetition rate. The THz generation beam is chopped at 2500 Hz using the 5 kHz laser reference as a trigger, as before, and the pump beam is chopped at 1250 Hz using the generation beam chopper reference output as a trigger. The generation beam chopper is phased such that every laser pulse is either completely blocked or unblocked. The pump beam chopper is then phased such that two consecutive pulses are either both blocked or unblocked. To achieve this, we measured the pump

beam using a photodiode after the chopper to ensure that no pulses were clipped by the chopper wheel. The THz detection diode peaks for the duration of 5 spindle rotations are then recorded as previously discussed in this chapter. This chopping scheme results in sets of 4 pulses where the THz is unblocked with the pump blocked, the THz is blocked with the pump blocked, the THz is unblocked with the pump unblocked, and the THz is blocked with the pump unblocked, respectively. These 4 pulses will be referred to as A_1, A_2, A_3, and A_4, for photodiode A, and B_1, B_2, B_3, and B_4, for photodiode B. Since the pump beam has no effect on the measured photodiode signals when the THz is blocked, A_2 and A_4 can be treated as identical reference measurements, with the same holding for diode B.

After measuring all THz detection photodiode peaks for the duration of 5 spindle rotations, the first and second pulses can be separated from the third and fourth pulses using software. These two data sets can then be used as independent measurements of static properties of the sample and the photoexcited properties of the sample, respectively.

$$\frac{1}{2}\left(\frac{A_1}{A_2}-\frac{B_1}{B_2}\right)=\frac{1}{2}\left(\frac{I+\Delta I_T(t_r)}{I}-\frac{I-\Delta I_T(t_r)}{I}\right)=\frac{\Delta I_T(t_r)}{I}\propto E_{THz}(t_r) \tag{3.24}$$

$$\begin{aligned}\frac{1}{2}\left(\frac{A_3}{A_4}-\frac{B_3}{B_4}\right)&=\frac{1}{2}\left(\frac{I+\Delta I_T(t_r-\phi)+\Delta I_P(t_r-\phi,t_p)}{I}\right)-\\ \frac{1}{2}\left(\frac{I-\Delta I_T(t_r-\phi)-\Delta I_P(t_r-\phi,t_p)}{I}\right)&=\frac{\Delta I_T(t_r-\phi)+\Delta I_P(t_r-\phi,t_p)}{I}\\ &\propto E_{THz}(t_r-\phi)+\Delta E_{THz}(t_r-\phi,t_p),\end{aligned} \tag{3.25}$$

where ΔI_T is the change in the photodiode signal due to the THz electric field probing the static properties of the material, ΔI_P is the change in the photodiode signal due to the pump-induced changed in the THz electric field, t_r is the spindle phase time, t_p is the pump-probe time delay, ϕ is the phase error due to the shift of two laser repetition periods between the two measurements, and ΔE_{THz} is the pump-induced change in the THz electric field. These two modulated THz signals can then be analyzed exactly as before, providing the polarization angle Θ due to the unpumped system and the pumped system simultaneously.

3.5 Test experiment: cyclotron resonance in a GaAs 2D electron gas

In order to test the capabilities of the TPMS system, we wished to study a well-understood system with known properties. In this section we will present data on the cyclotron resonance in a GaAs/AlGaAs 2D quantum well system, with a known mass and mobility. It is beneficial, however, to first understand how a cyclotron resonance in a metal leads to a Hall effect, and therefore polarization rotation, in the THz frequency range.

3.5.1 Faraday effect in a 2D metal

The dynamics of a simple two-dimensional metal in the THz frequency range can be well-understood by considering a system of free electrons that are driven by the THz electric field in the x-direction (in-plane) in the presence of an externally applied perpendicular magnetic field in the z-direction (out-of-plane). The electrons are assumed to interact only by scattering, which induces an effective drag force proportional to the electron velocity.

$$m\dot{\vec{v}}(t) = q\vec{E}(t) + q\vec{v} \times \vec{B} - m\gamma\vec{v}, \tag{3.26}$$

where q is the carrier charge, m is the carrier mass, and γ is the electron scattering rate. The current density can be written $\vec{j} = nq\vec{v}$, where n is the carrier density. Plugging this into formula 3.26 and assuming that $\vec{j}$ is oscillatory with frequency equal to that of the THz electric field gives

$$\begin{aligned}(\gamma - i\omega)j_x(\omega) &= \frac{nq^2}{m}E(\omega) + \omega_c j_y(\omega) \\ (\gamma - i\omega)j_y(\omega) &= -\omega_c j_x(\omega),\end{aligned} \tag{3.27}$$

where $\omega_c \equiv \frac{qB}{m}$ is the cyclotron frequency. Using the definition for conductivity $j_x \equiv \sigma_{xx}E_x$ and $j_y \equiv \sigma_{yx}E_x$, we obtain the formula for longitudinal and transverse

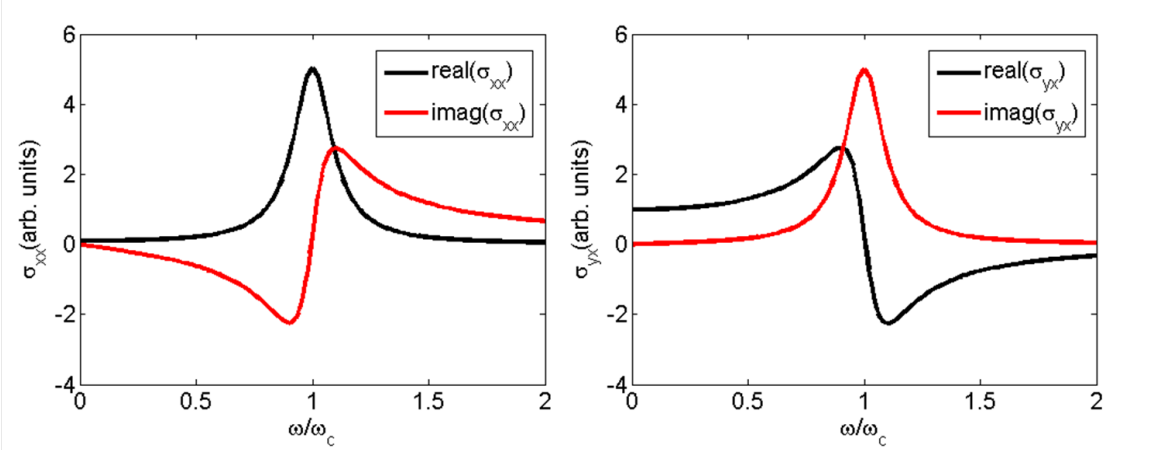

Figure 3.7: Longitudinal and transverse conductivity for a 2D metal. In this example, the carrier charge is negative and the scattering rate $\gamma = 0.1\omega_c$.

conductivity of the 2D metal (Figure 3.7):

$$\begin{aligned} \sigma_{xx} &= \frac{nq^2}{m} \frac{\gamma - i\omega}{(\gamma - i\omega)^2 + \omega_c^2)} \\ \sigma_{yx} &= \frac{nq^2}{m} \frac{-\omega_c}{(\gamma - i\omega)^2 + \omega_c^2)}. \end{aligned} \tag{3.28}$$

In a typical THz-TDS experiment, only the longitudinal conductivity $\sigma_{xx}(\omega)$ is measured, typically in the absence of magnetic field. In this case, two properties can be extracted, the spectral weight $\rho = \frac{nq^2}{m}$ and the scattering rate γ. When a magnetic field is applied, and the carrier mass is sufficiently low such that ω_c falls within the THz range for sufficiently low magnetic fields, $\sigma_{xx}(\omega)$ also provides a measurement of ω_c, and therefore a measurement of the carrier mass m.

When studying materials such as semimetals or semiconductor quantum well systems, it is important to be sensitive to the sign of the charge carriers. Measurements of σ_{xx} alone are insufficient to extract the sign of q, since all quantities depend on q^2. Measurements of σ_{yx}, however, depend on the sign of the cyclotron frequency, and therefore the sign of q. Furthermore, measurements of the Faraday rotation angle given by formula 3.6 also provide a measurement of the sign of q. In the case of a film with thickness d on a substrate with index of refraction n_s, when $Z_0 d\sigma_{xx} \ll 1$,

the polarization rotation angle is given by

$$tan(\Theta) = \frac{Z_0 d\sigma_{yx}}{1 + n_s}, \tag{3.29}$$

and when $Z_0 d\sigma_{xx} \gg 1$, the polarization rotation angle is given by

$$tan(\Theta) = \frac{\sigma_{yx}}{\sigma_{xx}} = \frac{-\omega_c}{\gamma - i\omega}. \tag{3.30}$$

In both limits, the polarization rotation angle depends on the sign of the carrier charge, making Faraday rotation measurements, and hence TPMS measurements, a good probe for studying the properties of charge carriers in semimetals and semiconductors.

3.5.2 TPMS measurements of the cyclotron resonance in a GaAs/AlGaAs quantum well

As a test experiment, we performed Faraday rotation measurements on a GaAs/$Al_{0.3}Ga_{0.7}As$ quantum well system. The samples were obtained from Sandia National Lab [91,92]. This system behaved as a 2D electron gas (2DEG) with electron-like carriers with an effective mass of 0.069 m_e, a density of ~3×10^{11} cm^{-2}, and a mobility of ~250,000 $cm^2/V/s$. This system served as an ideal test material because it displayed a strong and sharp cyclotron resonance in the THz range at reasonable values of magnetic field, due to its low carrier mass and high mobility.

While TPMS was technically capable of measuring σ_{xx} and σ_{yx}, we found it preferable to instead independently measure σ_{xx} and the polarization rotation angle Θ. The reason for this was three-fold. First, measurements of Θ are intrinsic to the material, and do not require division of a reference signal. These measurements, therefore, were immune to instability in the laser power or pointing. Second, background polarizaton errors could be subtracted out using a reference scan, while removal of these errors was difficult when considering $E_x(\omega)$ and $E_y(\omega)$ directly. Finally, σ_{xx} could be measured using standard THz-TDS techniques, which are unaffected by background

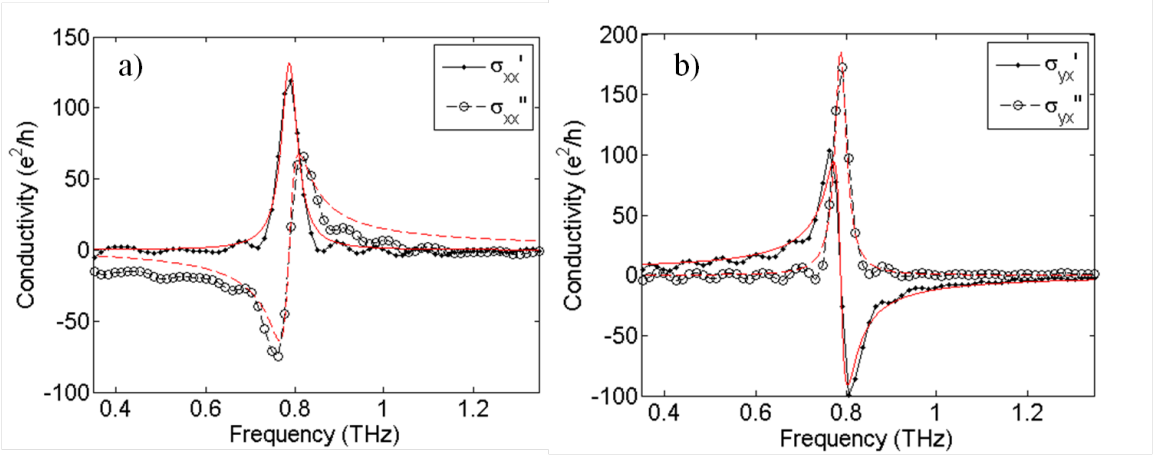

Figure 3.8: a) Logitudinal and b) transverse conductivity in a GaAs 2DEG measured by THz-TDS and TPMS. Dots correspond to the real part of the conductivity, while circles correspond to the imaginary part. The red lines denote fits to the theoretical form for the cyclotron resonance in a 2D metal (formula 3.28).

polarization errors to second order, and provide a measurement of σ_{xx} with less noise. After measuring σ_{xx} and Θ independently, we then extracted σ_{yx} using formula 3.6.

Due to the extremely low scattering rate of the 2DEG, its conductivity in the THz range could not be measured in the absence of magnetic field, since nearly all of the spectral weight fell below 0.2 THz. It was therefore ideal to use the 2DEG sample in the absence of a magnetic field as a reference, but this proved infeasible due to the large amount of time it took to change the magnetic field. Any change in the generated THz pulses during this wait time would have contributed systematic error to the measurement. To solve this problem, we normalized the sample scans by a vacuum reference scan before changing the field, then used these two normalized scans as sample and reference scans, respectively. Mathematically, this did not affect the extraction of σ_{xx}, but it did serve to cancel the aforementioned systematic error. We performed THz-TDS measurements at 2 T and -2 T, normalized by a vacuum reference, then normalized by the same measurements at 0 T, to extract $\sigma_{xx}(\omega, B = 2T)$ (Figure 3.8a).

To measure Θ, we performed TPMS measurements at 2 T and -2 T, using vacuum as a reference. To subtract out any systematic polarization angle errors, we

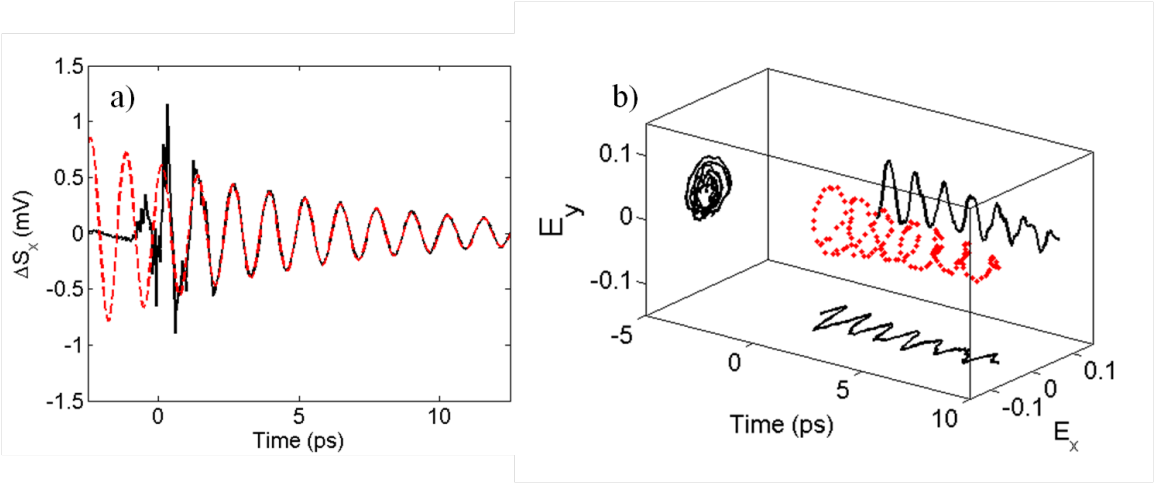

Figure 3.9: a) Subtraction of $E(t, 2T)$ and $E(t, 0T)$ after an appropriate scaling, measured by THz-TDS. The oscillation was fit to a decaying sinusoid $S = e^{-\gamma t} sin(\omega_c t + \delta)$ (red curve), with an extracted scattering rate γ of 134 GHz and a cyclotron frequency ω_c of 0.787 THz. b) Three dimensional plot of the electric field subtraction measured by TPMS. The circularly polarized component induced by the cyclotron resonance can be clearly seen.

subtracted the reference scan polarization angle from the sample scan angle, and then performed the antisymmetrization operation $\Theta_{anti} = \frac{1}{2}(\Theta(2T) - \Theta(-2T))$. The antisymmetrization operation ensured that the measured polarization angle was induced by the magnetic field. The transverse conductivity σ_{yx} was then calculated by plugging the measured Θ into formula 3.6, and can be seen in Figure 3.8b. The data were fit simultaneously using formula 3.28 to extract the charge carrier properties. The fits can also be seen in Figure 3.8. From the fits, we found a carrier density of 3.5×10^{11} cm^{-2}, a carrier charge of $-e$, a carrier mass of 0.071 m_e given by the cyclotron frequency of 0.788 THz, a scattering rate of $97 - 137$ GHz, and hence a mobility of 255,000 cm^2/Vs. The carrier mass agreed well with the accepted value of 0.069 m_e [92], with the discrepancy possibly being explained by a 3% error in the applied magnetic field.

While the frequency-domain results provided very reasonable results, issues in the time-domain led to unavoidable Fourier transform artifacts that could have skewed some of the fit parameters. The sharpness of the cyclotron resonance resulted in a

very long-lived oscillation in the time-domain, with a life-time of about 7 ps. This oscillation made it impossible to fully temporally separate the main THz pulse from the sample and ZnTe etalons, as discussed in the previous chapter. We found that it was instead useful to analyze the data in the time-domain. Since the cyclotron resonance led to a long-lived oscillation in time, while otherwise only altering the main THz peaks by a scale factor to good approximation, we directly subtracted $E(t)$ at 0 T from $E(T)$ at 2 T after rescaling the electric field traces to have equal peak sizes. This subtraction effectively isolated the oscillating component. The result of this subtraction using the THz-TDS data can be seen in Figure 3.9a, along with a fit to a decaying exponential $S = e^{-\gamma t} sin(\omega_c t + \delta)$. From this fit we extracted a scattering rate of 137 GHz and a cyclotron frequency of 0.787 THz. We performed the same subtraction using $E_x(t)$ and $E_y(t)$ measured using TPMS to obtain the circularly polarized component of the THz electric field that was induced by the cyclotron resonance in the 2DEG. This circular component can be clearly seen in Figure 3.9b.

3.6 Conclusions

We have presented a technique called Terahertz Polarization Modulation Spectroscpoy (TPMS), which enabled measurements of the complex THz polarization after transmission through a sample. A fast-rotating polarizer was used to modulate the transmitted THz polarization, and the modulated THz electric field was recording using free-space electro-optic sampling with the DAQ card implementation described in the previous chapter. The modulated THz electric field was compared to the measured polarizer rotation, enabling the measurement of both components of the THz polarization simultaneously with common-noise subtraction. To test this technique, we performed Faraday rotation measurements on a GaAs/AlGaAs 2DEG and found a clear cyclotron resonance in both the longitudinal and transverse conductivities. The sign of the charge carriers, as well as their mass, density, and scattering rate was extracted, matching results from transport measurements. The DAQ card implementation of this technique further enables pump-probe polarization rotation measure-

ments in which the polarization angle and the pump-induced change in the angle are simultaneously measured.

Chapter 4

Spin-Induced Optical Conductivity in the Spin Liquid Candidate Herbertsmithite

A quantum spin liquid (QSL) is a state of matter in which antiferromagnetic spins interact strongly, but quantum fluctuations inhibit long-range magnetic order even at zero temperature. The QSL concept was first conceived of by Anderson in 1973 [32] and later suggested as a possible explanation for high temperature superconductivity in the cuprates [111, 112]. The proposed ground state of a QSL, the so-called Resonating Valence Bond (RVB) state, hosts exotic excitations through spin-charge separation, giving rise to chargeless spin $1/2$ spinons, in contrast to the conventional spin-wave excitations (magnons with spin 1) in ordered Mott insulators [39, 58, 113, 114]. While QSLs have been a theoretical construct for decades, recent experiments provided compelling evidence that the long-sought QSL system can be realized in the kagome-lattice antiferromagnet $ZnCu_3(OH)_6Cl_2$ (also called Herbertsmithite) [18, 34, 47–55] (Figure 4.1), as well as the triangular organic salts $EtMe_3Sb[Pd(dmit)_2]_2$ [42, 43] and κ-$(BEDT\text{-}TTF)_2Cu_2(CN)_3$ [44–46]. In particular, Herbertsmithite exhibits no magnetic order down to T = 50 mK in thermodynamic measurements [18], and exhibits a scattering continuum that is consistent with spinon excitations in the inelastic neutron scattering measurements [34].

4.1 Open question: the existence of a spin excitation gap in Herbertsmithite

Despite these experimental works, there are still a number of open questions on the nature of the ground state in Herbertsmithite, specifically the gauge group of the spin liquid state and the character of the low-energy spin excitations. A recent computational study proposed the existence of a Z_2 spin liquid with a sizable spin gap in Herbertsmithite [59]. Thermodynamic and inelastic neutron scattering results, however, showed no sign of a spin gap down to 0.1 meV [18,34], suggesting the existence of a gapless U(1) spin liquid state in Herbertsmithite. Optical studies have proved difficult due to the chargeless nature of the spinon excitations and the relatively low energy scale in the spin system. Recent theoretical studies have, however, proposed that spin-charge interactions through an emergent gauge field in a U(1) Dirac spin liquid can give rise to a contribution to the real part of the low-frequency optical conductivity [40, 41]. In particular, a power-law dependence of the conductivity (σ) on the photon frequency (ω), i.e. $\sigma \sim \omega^{\beta}$, with an exponent $\beta = 2$, is expected at frequencies far below the charge gap. Direct measurement of such power-law optical conductivity is therefore a great step toward elucidating the nature of the QSL ground state and the structure of the low-energy excitations in Herbertsmithite.

The theory of Ng and Lee [40] has previously been tested in the organic compound κ-(BEDT-TTF)$_2$Cu$_2$(CN)$_3$ using a variety of optical techniques [76]. Power-law behavior is indeed observed in the real part of the in-plane optical conductivity over a wide range of frequencies and temperatures, though the value and temperature dependence of the power-law exponent seem to contradict the theoretical predictions. In addition, the power-law behavior unexpectedly persists at temperatures and frequencies much higher than the exchange coupling J, calling into question whether spinon physics is responsible for the observed behavior. The question still remains, however, whether the theory of Ng and Lee will be realized in Herbertsmithite.

In this chapter, we report a direct observation of the spin-induced low-frequency optical conductivity in Herbertsmithite (all conductivities reported are the real com-

ponent). This experiment is made possible for the first time by the recent successful growth of large-area single crystals of Herbertsmithite [57]. By using Terahertz Time-Domain Spectroscopy (THz-TDS), which was discussed previously in this dissertation, we have measured the optical conductivity of Herbertsmithite as a function of temperature and magnetic field in the spectral range of 0.6 to 2.2 THz. Remarkably, the in-plane conductivity $\sigma_{ab}(\omega)$, which is associated with the spin liquid state in the kagome (ab) planes of Herbertsmithite, was found to depend on frequency as $\sigma_{ab}(\omega) \sim \omega^{\beta}$ with $\beta \approx 1.4$, a result compatible with the theoretical predictions [40, 41]. The observed power-law conductivity also exhibited the opposite temperature dependence expected for an insulator, and was absent in the out-of-plane direction, as expected for a two-dimensional gapless spin liquid state. Our findings are consistent with the predicted low-frequency absorption arising from an emergent gauge field in a gapless U(1) Dirac spin liquid.

4.2 Sample structure and alignment

In our experiment, we investigated a large single-crystal sample of Herbertsmithite with dimensions 3 x 6 x 0.8 mm. The sample was characterized by neutron diffraction, anomalous x-ray diffraction, and thermodynamic measurements, with results compatible with those of powder samples [57]. As shown in Figure 4.1, Herbertsmithite has a layered structure, with planes of spin-$^1/_2$ copper atoms in a kagome pattern separated by nonmagnetic zinc atoms. This material exhibits strong in-plane (ab) antiferromagnetic interactions with Curie-Weiss temperature Θ_{CW} = -300 K, a charge gap of ~2 eV and a spinon gap of less than 0.1 meV, as well as an exchange energy J $\approx$ 17 meV (200 K) as described by a Heisenberg model, with negligible out-of-plane (c) interactions [18]. Despite the strong interactions in this material, geometric frustration prevents the formation of any magnetic order down to T = 50 mK [18].

The sample of Herbertsmithite was grown by the group of Prof. Young Lee at MIT, who developed a technique to grow the first large single-crystals of Herbert-

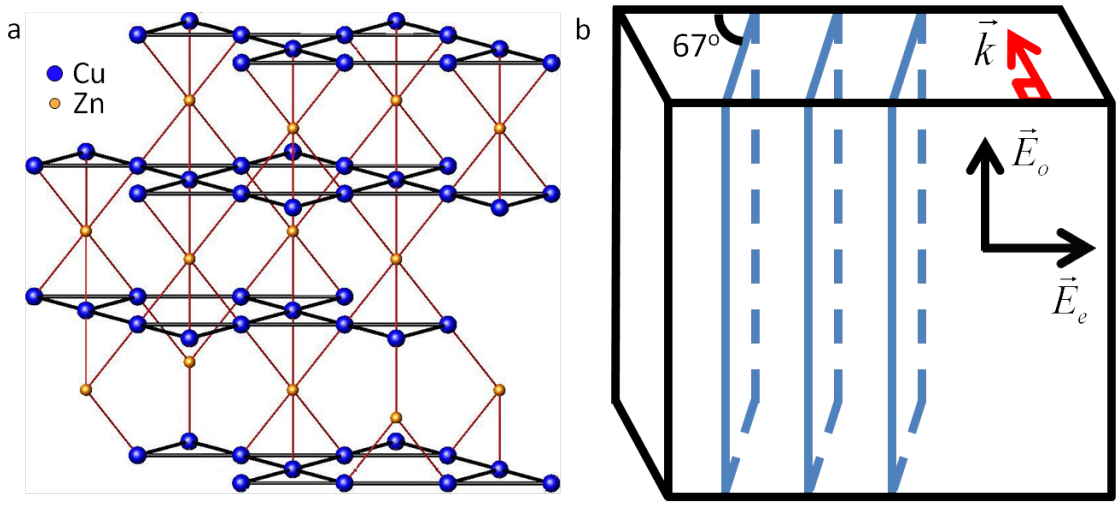

Figure 4.1: a) The crystal structure of Herbertsmithite (with oxygen, chlorine, and hydrogen atoms omitted). The crystal is composed of layers of copper atoms carrying a spin-1/2 moment arranged in a kagome pattern. These layers are separated by nonmagnetic zinc atoms. b) The orientation of the sample used in our experiment. The kagome (ab) planes are aligned vertically and make a 67° angle with the surface. $\vec{E}_o$, $\vec{E}_e$, and $\vec{k}$ denote, respectively, the ordinary and extraordinary optical axes of the crystal and the wave vector of the incident terahertz beam.

smithite [57]. While the sample we obtained was approximately 3 x 6 x 0.8 *mm* in size, polarized microscope images showed the existance of multiple crystallographic orientations within the sample. Figure 4.2a shows a polarized microscope image of the sample. The light-colored regions correspond to regions of different crystallographic orientation, while the darker regions corresponded to the orientation of interest. The 2 *mm* diameter circled region was therefore chosen to minimize the contribution of the other crystal orientation. The chipped edge at the top of the image (denoted by a line) shows the orientation of the kagome planes within the sample. This line was aligned vertically, such that vertically polarized light fell entirely within the kagome planes. The sample was then mounted on a copper sample-holder using conducting silver epoxy, with the circled region on top of a 2 *mm* through hole (Figure 4.2). A second identical hole was used for the reference scans.

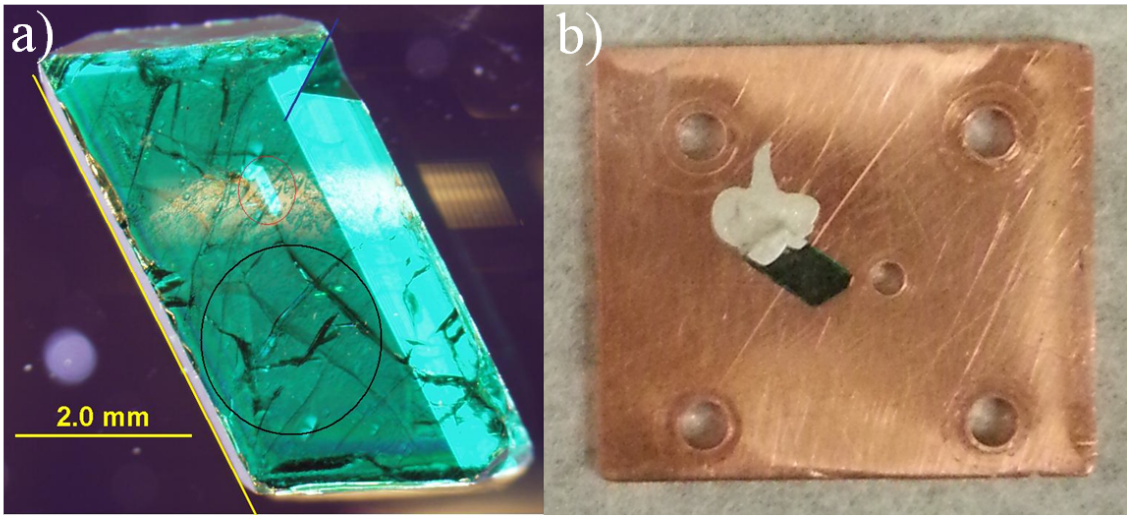

Figure 4.2: a) A polarized microscope image of the Herbertsmithite sample. Light-colored regions correspond to a different crystallographic orientation than the darker regions. The 2 *mm* diameter circled region was chosen to minimize the contribution of the other cyrstal orientations. b) The sample mounted on the copper sample-holder used in the experiment. The sample was aligned such that the vertical direction was parallel to the kagome planes. The sample was then mounted on a copper plate using conducting silver epoxy, with the circled region in a) on top of a 2 *mm* through-hole. An identical through-hole was drilled next to the sample to be used as a reference.

4.3 Extraction of optical properties of a birefringent material

In chapter 2, we discussed how to extract the optical properties of an isotropic thick slab using THz-TDS. In this case, however, the sample is uniaxially anisotropic, with the optical properties in the direction parallel to the kagome planes being different than in the direction perpendicular to the kagome planes. It is important, therefore, to understand how light transmits through such a material in order to make meaningful measurements of its optical properties.

In a uniaxial crystal, the index of refraction experienced by light depends on the angle the polarization of the light makes with the ordinary and extraordinary axes of the crystal [115]. In this case, the kagome planes serve as the ordinary axis, with the extraordinary axis perpendicular to the planes. Let us consider the kagome planes to

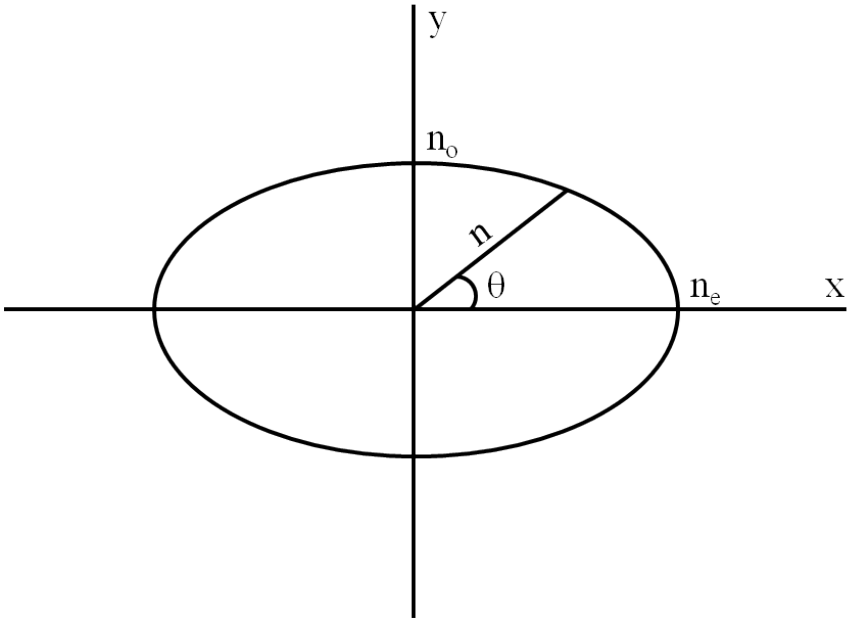

Figure 4.3: The index ellipsoid for a uniaxial crystal. When the polarization of light make an angle θ with the extraordinary axis of a crystal, the index of refraction experienced is equal to the length of the line intersecting the ellipsoid and the origin at angle θ.

be parallel to the y-axis, and perpendicular to the x-axis. The index of refraction is then given by the index ellipsoid [115]

$$\frac{x^2}{n_e^2} + \frac{y^2}{n_o^2} = 1, \tag{4.1}$$

where n_e is the index of refraction along the extraordinary axis, and n_o is the index of refraction along the ordinary axis. The index of refraction at some angle θ relative to the extraordinary axis is given by the length of the line that intersects the origin at angle θ and the ellipsoid. A schematic of this index ellipsoid can be seen in Figure 4.3. For an angle θ that intersects the ellipsoid at point $(x, y) = (ncos(\theta), nsin(\theta)$, formula 4.1 can be rewritten as

$$\frac{1}{n^2} = \frac{cos^2(\theta)}{n_e^2} + \frac{sin^2(\theta)}{n_o^2}. \tag{4.2}$$

For Herbertsmithite, $n_e = n_c$ and $n_o = n_{ab}$, giving the equation

$$\frac{1}{n^2} = \frac{cos^2(\theta)}{n_c^2} + \frac{sin^2(\theta)}{n_{ab}^2}, \tag{4.3}$$

where n is the measured index of refraction when the incident polarization makes an angle θ with the c-axis of the crystal. The index of refraction can be extracted as before using the thick slab trasmission coefficient

$$T = \frac{4ne^{in\omega d/c}}{(n+1)^2} \tag{4.4}$$

where d is the sample thickness, and the conductivity can be extracted using the equation

$$\sigma = 2\epsilon_0 \omega Re(n) Im(n). \tag{4.5}$$

The indices of refraction n_{ab} and n_c can be separately determined by performing two measurements. First, the THz polarization is aligned vertically such that it lies within the kagome planes. In this case, $\theta = 90°$, giving $n = n_{ab}$. Second, the THz polarization is rotated by 90° such that it makes a 23° angle with the c-axis of the crystal. In this case, the transmission coefficient depends on the optical properties in both the in-plane and out-of-plane directions. In order to isolate the contribution from the out-of-plane direction, the previously measured n_{ab} along with the measured n can be inserted into formula 4.3 to solve for n_c and hence σ_c. We also note that in the measurement of the out-of-plane conductivity, the terahertz pulse travels inside the sample with a group velocity slightly deviated from its wave vector due to the anisotropy of the crystal. However, we estimate that the deviation angle is rather small (~3°) and the resultant error in the transmission measurement is negligible (~0.3%)

4.4 THz conductivity measurements in single-crystal Herbertsmithite

We measured the THz in-plane conductivity $\sigma_{ab}(\omega)$ that is associated with the spin liquid state in the Herbertsmithite crystal by THz-TDS (this work was published in PRL in 2013 [75]). The experiment was performed using a mode-locked Ti:Sapphire amplified laser system, which generated pulses with 800 nm central wavelength, 100 fs pulse duration and 5 kHz repetition rate. The THz radiation was generated via optical rectification in a <110>-oriented ZnTe crystal, focused onto the sample using off-axis parabolic mirrors, and subsequently detected via free space electro-optic sampling in a second ZnTe crystal. The THz radiation was polarized along the kagome (ab) planes using wire-grid polarizers. We recorded the THz electric field transmitted through the Herbertsmithite sample, and as a reference, the THz field transmitted through vacuum. From the Fourier transformed frequency-domain fields for the sample and reference, we extracted the frequency-dependent optical conductivity, taking into account the sample geometry.

Figure 4.4a displays the in-plane optical conductivity spectra $\sigma_{ab}(\omega)$ in the frequency range of 0.6 - 2.2 THz at temperatures from 4 K to 150 K. The conductivity spectra can be described by two components. The higher-frequency component, which is significant for frequencies $> 1.4\ THz$, can be attributed to the phonon absorption with a resonance at ~3 THz, as will be discussed later in this chapter. Here we focus on the lower-frequency component, which dominates the absorption at frequencies $<$ 1.4 THz. This component can be described by a power law with a small exponent $\sigma_{ab} \sim \omega^{\beta}$, where $\beta \approx 1.4$. (We note that, due to the limited frequency range in our measurement, an exponent β between 1 and 2 is still compatible with the data. This will be discussed further later in this chapter) Such an absorption behavior is distinct from that expected in ordered Mott insulators, which typically exhibit ω^4 frequency-dependent conductivity at low frequencies arising from the spin-wave excitations [40]. In the following discussion, we will provide evidence that the ω^{β} absorption arises from the spin excitations in Herbertsmithite.

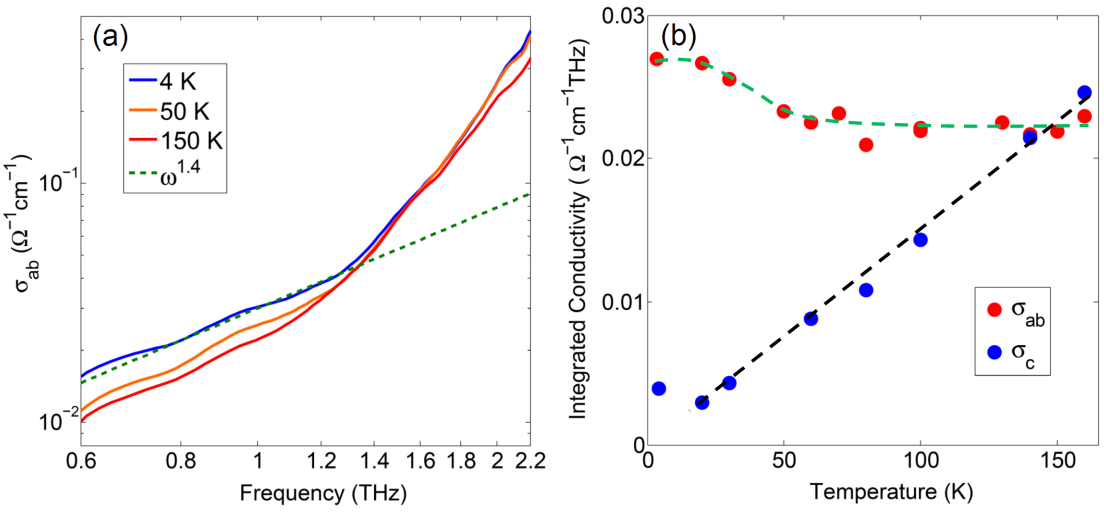

Figure 4.4: a) The in-plane optical conductivity σ_{ab} in the spectral range of 0.6 - 2.2 THz at temperatures T = 4, 50 and 150 K. The spectra consist of a higher-frequency component, arising from a phonon resonance at ~3 THz, and a lower-frequency component that exhibits a power-law dependence on frequency as σ_{ab}~ω^{β} with $\beta \approx 1.4$ (dotted line). The data are plotted in log-log scale to highlight this power-law behavior. b) The integrated values of the in-plane conductivity σ_{ab} from (a) and of the out-of-plane conductivity σ_c from Figure 4.5 from 0.6 to 1.4 THz for temperatures T = 4 - 160 K. σ_{ab} is found to decrease as the temperature increases up to T $\approx$ 60 K, where it remains constant. In contrast, σ_c increases monotonically with temperature. Dashed lines are guides to the eye.

First, we observed a noticeable enhancement of the ω^{β} absorption component as the temperature decreased from 150 K to 4 K (Figure 4.4b). The increase of absorption at lower temperature, we remark, is a rather anomalous phenomenon for insulating materials, where light absorption far below the band gap typically decreases at low temperature due to the freezing of phonons and doped charges. The observed unusual temperature dependence immediately indicates that the underlying absorption mechanism must be of exotic origin. Indeed, the temperature dependence of $\sigma_{ab}(\omega)$ is reminiscent of that of metals, suggesting that $\sigma_{ab}(\omega)$ is associated with a gapless or nearly-gapless spin system in Herbertsmithite. Our results are consistent with a similar phenomenon in the Raman scattering of Herbertsmithite, where a continuum of Raman signal due to spinon excitations is found to increase with decreasing temperature at T $<$ 50 K [52]. From the lower bound of our measured

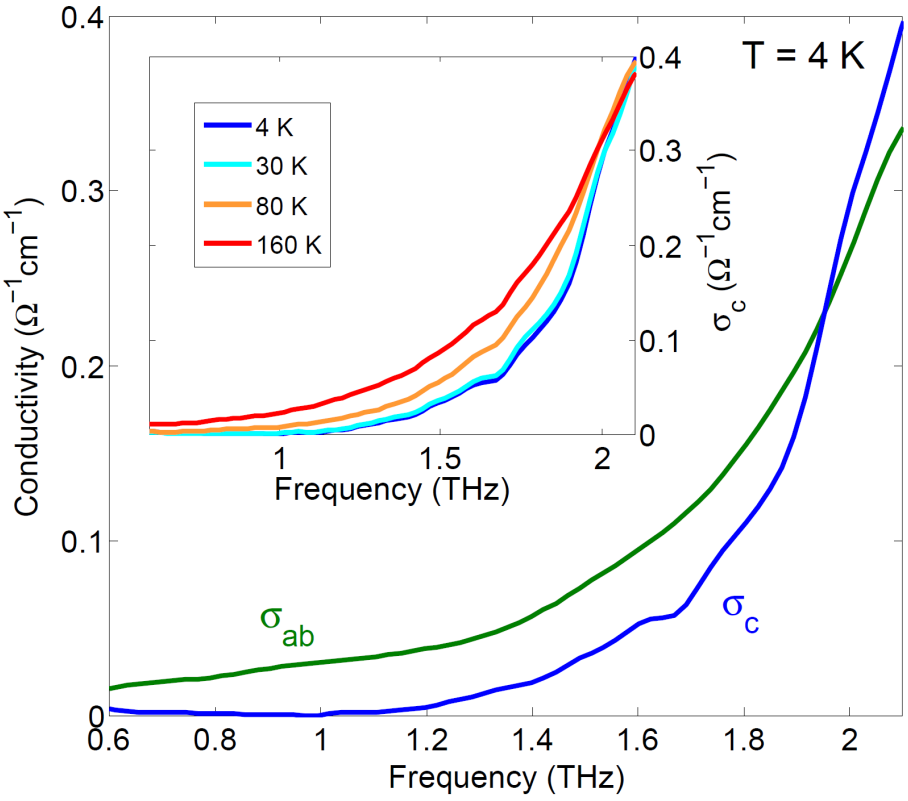

Figure 4.5: Out-of-plane optical conductivity of Herbertsmithite (σ_c) (blue line), measured in the spectral range of 0.6 - 2.2 THz at T = 4 K, in comparison with the in-plane conductivity σ_{ab} (green line). The inset displays the σ_c spectra at T = 4, 30, 80 and 160 K. The magnitude of σ_c is found to increase with the temperature.

frequency range, we estimate that the spin gap in Herbertsmithite, if it exists, should not be larger than 0.6 THz (~2 meV). This value is consistent with the upper bound of the spin gap (~0.1 meV) estimated by other experimental studies [18,34].

Second, we found that the ω^{β} absorption component disappears in the direction perpendicular to the kagome planes. We have measured the out-of-plane conductivity $\sigma_c(\omega)$ along the c-axis of the Herbertsmithite crystal at different temperatures. The $\sigma_c(\omega)$ spectra resemble the tail of a phonon resonance at >3 THz (Figure 4.5). In particular, $\sigma_c(\omega)$ at T = 4 K is found to drop rapidly to zero at frequencies lower than 1 THz, in contrast to the ω^{β} behavior observed in the in-plane conductivity $\sigma_{ab}(\omega)$. In addition, the magnitude of $\sigma_c(\omega)$ is found to drop as the temperature decreases (Figures 4.4b and 4.5), a typical behavior of phonon absorption. The absence of the

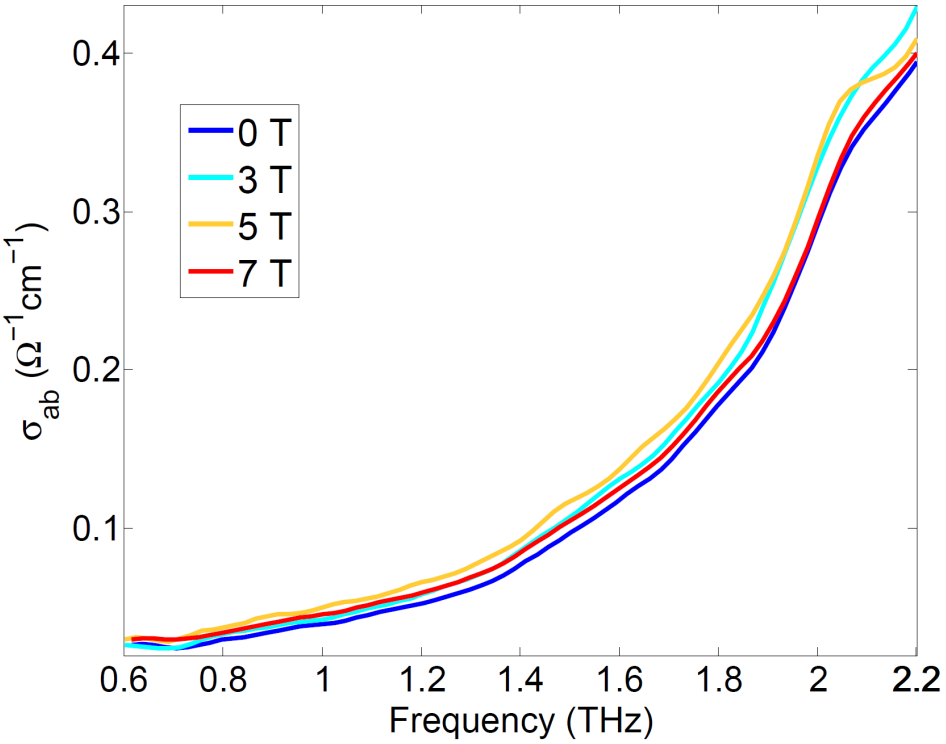

Figure 4.6: In-plane conductivity of Herbertsmithite (σ_{ab}) measured in the spectral range of 0.6 - 2.2 THz at magnetic fields of 0, 3, 5, and 7 T and T = 6 K. No systematic magnetic-field dependence is observed. The small variation between measurements is attributed to experimental nonrepeatability due to the difficulty of the measurements in the magnetic cryostat.

ω^{β} absorption component in the out-of-plane direction indicates that it is adherent to the in-plane properties of the sample. Due to the quasi-two-dimensional nature of the spin system in Herbertsmithite, where the spin excitations are confined to move only in the kagome planes, our result strongly suggests that the ω^{β} absorption found only within the planes is associated with the spin degree of freedom in Herbertsmithite.

Third, the ω^{β} absorption is unaffected by the presence of a strong magnetic field. According to previous x-ray scattering studies [53], a 5% excess of copper atoms were found between the kagome planes in our Herbertsmithite sample. Although these additional copper atoms leave the geometric frustration intact, they can act as random paramagnetic spins to induce a Curie tail in magnetic susceptibility [18, 51]. In respect to our experiment, these spin impurities may contribute to the optical

conductivity in the low frequency range, and hence obscure the interpretation of our experimental data. An investigation of the magnetic field dependence should be able to rule out their effect. In the presence of magnetic field, the conductivity due to the excess copper atoms is expected to disappear at low frequency due to the Pauli Exclusion Principle as the defect spins are aligned to the magnetic field. In contrast, the spin liquid state cannot be magnetically aligned except at fields greater than 12 T or at temperatures below 1 K, where a phase transition from spin liquid to spin solid may occur [116, 117]. In our experiment, we have measured the in-plane conductivity $\sigma_{ab}(\omega)$ in the spectral range of 0.6 - 2.2 THz under magnetic fields from 0 T to 7 T at T = 6 K (Figure 4.6). We did not observe any systematic dependence of the absorption on the magnetic field. In particular, the exponent of the power-law fit to the data is essentially unchanged with the magnetic field. The slight change of the absorption magnitude is within our experimental errors, including the possible clipping of the incident beam on the sample holder and the imperfect alignment of the optics within the chamber of the superconducting magnet. Indeed, the result is consistent with the expected behavior of the spinon excitations in a QSL, which generally exhibits a field-independent energy spectrum except in extreme conditions (such as in B $>$ 12 T or T $<$ 0.5 K, where a phase transition may occur.) [116, 117]. From this result, we can safely exclude magnetic disorder as a source of the low-frequency optical conductivity in our experiment.

Finally, the observed frequency dependence and magnitude of σ_{ab} agree well with those predicted for the spin-induced absorption in a QSL. In particular, recent theory showed that in a gapless U(1) Dirac spin liquid a power-law optical conductivity $\sigma \sim \omega^{\beta}$ with $\beta = 2$ can arise from the spin-charge interactions through an internal gauge field, and the calculated absorption magnitude is compatible with our experimental data [40, 41]. Similar power-law absorption is also suggested for a gapped Z_2 spin liquid [41] due to modulation of the Dzyaloshinkii-Moriya (DM) interaction, but the predicted absorption magnitude is three orders of magnitude too small to match our data. Our results therefore favor the existence of a U(1) spin liquid state with an emergent gauge field in Herbertsmithite.

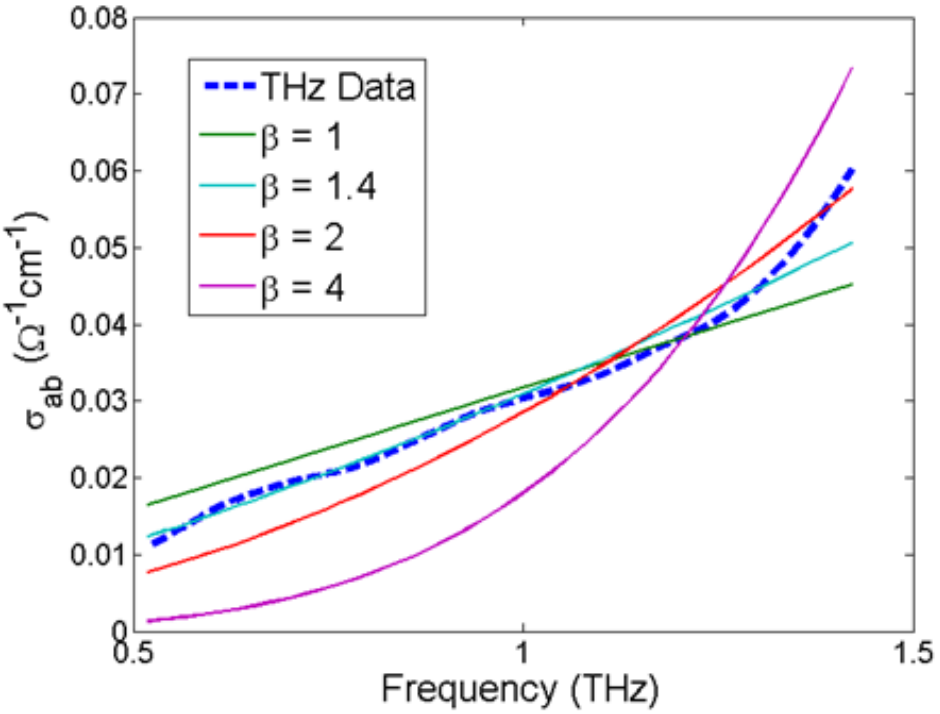

Figure 4.7: In-plane THz conductivity σ_{ab} plotted against power-law fits ω^{β} for various values of β. The fit corresponding to $\beta = 4$ results in errors too large to be explained by systematic experimental errors. Fits with $\beta = 1 - 2$ provide reasonable fits within the estimated systematic error of 3%.

4.4.1 Power-law exponent errors

The measured in-plane optical conductivity exhibits a power-law behavior at low frequency. Power-law fits to the data reveal an exponent of 1.4 ± 0.06, however, the limited available frequency range must also be taken into account. Small systematic errors or artifacts in the data can have a reasonably large effect on the extracted exponent when the frequency range is small. We expect small systematic errors, especially at low frequency, due to the small size of the sample and the difficulty in focusing long-wavelength light to a small diameter. Because of this issue, one can reasonably expect an error of a few percent in the measured transmitted electric field. Figure 4.7 shows the in-plane optical conductivity at 4 K, with power-law fits ω^{β}, where $\beta = 1$, 1.4, 2, and 4, respectively, with $\beta = 1.4$ being the best fit. In the case of $\beta = 1$ or 2, the maximum error is 0.005 $\Omega^{-1}cm^{-1}$, corresponding to an error

in the measured transmitted electric field of 3%. For $\beta = 4$, the maximum error is 0.015 $\Omega^{-1}cm^{-1}$, or an error in the transmitted electric field of 10%. We can conclude that the power-law exponent is less than 4, and can therefore rule out any spin-wave contribution to the conductivity in Herbertsmithite. We claim that a 3% error in the transmitted electric field is reasonable for the constraints of the experimental setup, and therefore a power-law exponent of 1-2 is in agreement with our data.

4.5 Fourier Transform Infrared Spectroscopy measurements on Herbertsmithite

As shown in Figure 4.4a, we observed in the in-plane conductivity spectra $\sigma_{ab}(\omega)$ a higher-frequency component that was distinct from the expected $\sigma_{ab}{\sim}\omega^{\beta}$ behavior, which is significant at frequencies above 1.4 THz. We ascribe this component to phonon absorption, distinct from the spin-induced absorption that dominates at frequencies below 1.4 THz. In order to elucidate the nature of the higher-frequency absorption component, we have investigated the optical response of the Herbertsmithite crystal at frequencies well above 1.4 THz. In particular, we measured the reflectance of the sample in the spectral range of 3 - 16 THz by means of Fourier transform infrared (FTIR) spectroscopy. The measurements were performed at room temperature and ambient conditions in the lab of Prof. Willie Padilla at Boston College, using a THz FTIR microscope, which enabled us to collect reliable reflectivity data over a wide frequency range (3-16 THz) with a focal spot of ~0.5 mm. Such a tight focal spotted ensured that we probed only the single-crystal portion of interest in the sample. The polarization of the incident infrared beam was aligned along either the ordinary or extraordinary axis of the crystal for the measurement of the in-plane and out-of-plane reflectance, respectively, and then the reflected THz power was measured using a liquid helium-cooled bolometer.

Figure 4.8a displays the in-plane reflectance of Herbertsmithite at frequencies above 3 THz. The spectrum exhibits four peaks, which we attribute to four phonon

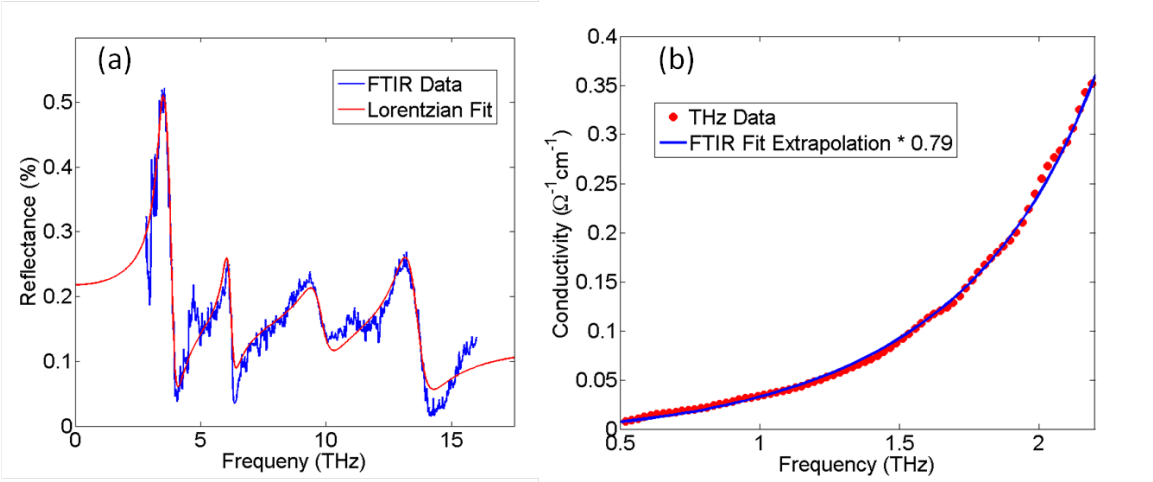

Figure 4.8: a) FTIR reflectance measurements on single-crystal Herbertsmithite at room temperature, with polarization aligned parallel to the kagome planes (blue). The data was fit to four Lorentzians in the electric permittivity (red), providing an extrapolated conductivity in the frequency range of interest (0.5-2.2 THz). b) The extrapolated conductivity from the FTIR fits in the frequency range relevant to THz-TDS (blue), compared with the measured in-plane conductivity σ_{ab} measured by THz-TDS (red). The extrapolation agrees quite well with the THz-TDS data up to a small multiplicative error.

absorption resonances. We can describe the experimental data adequately by considering reflection arising from four Lorentzian oscillators with a small constant reflection background in the electric permittivity ϵ of the sample (red line in Figure 4.8a). The reflectance can then be modeled by calculating the resultant index of refraction $n = \sqrt{\epsilon}$ and the reflection coefficient $R = \left(\frac{1-n}{1+n}\right)^2$ corresponding to these Lorentzian oscillators. While the light source was CW, it was reasonable to assume that etalons did not affect the measured reflectance, due to the extremely low transmission coefficient in this frequency range. The lowest-frequency resonance in the fit was at 3.4 THz. From the reflectance fit, we have extracted the optical conductivity given by $\sigma = \epsilon_0 \omega \times Im(\epsilon)$ and extrapolated it to frequencies below 2 THz in order to make comparison with the conductivity data obtained by terahertz time-domain spectroscopy. As shown in Figure 4.8b, the extrapolated conductivity agrees reasonably well with the terahertz data for both the absorption magnitude and spectral shape, except for a small multiplicative error. This error could easily result from a

slight deviation from Lorentzian behavior, which was assumed to persist to the frequency range measured by THz-TDS. Therefore, our analysis strongly suggests that the higher-frequency component observed in the terahertz in-plane conductivity is a tail of a phonon resonance at ~3 THz. This phonon, however, cannot explain the σ_{ab}~ω^{β} term in the low temperature THz-TDS data due to its anomalous temperature dependence.

4.6 Conclusions

In conclusion, we have performed THz-TDS measurements on a large single crystal of Herbertsmithite and observed a power-law component ω^{β} with $\beta \approx 1-2$ in the low-frequency in-plane THz conductivity. Detailed analysis showed that the absorption arises from spin excitations. Our results agree with theoretical predictions based on the spin-charge coupling through an emergent gauge field in a gapless Dirac spin liquid, and put an upper bound of 2 meV on the size of the spin gap. This discovery hints at the existence of a gauge field in a spin liquid, which is of profound significance in the field of spin liquid research. More generally, our research demonstrated THz-TDS to be an effective probe to study quantum spin liquids. Conductivity measurements have the potential to extend to the GHz and MHz frequency range via electronic methods, which, combined with sub-Kelvin cooling, may allow us to probe the extremely low-energy excitations in the spin liquid and provide a definite answer on the nature of the ground state in Herbertsmithite.

Chapter 5

Afterword

In this dissertation, I have presented Terahertz spectroscopy studies of a novel phase of magnetism in Herbertsmithite called the Quantum Spin Liquid (QSL) state. The QSL state breaks the typical rules that condensed matter physicists use to understand the phases of matter. More specifically, it is a distinct phase of matter that breaks no symmetries, resulting in exotic behavior such as fractionalized spin excitations and macroscopic quantum entanglement. The use of symmetry breaking as a tool to classify and understand phases of matter is nearly ubiquitous, so new tools must be created to understand and classify the phases of matter that break no symmetries. Rather than classifying QSL states by which symmetries are broken, theorists instead classify the types of QSL state by the gauge transformations that preserve the properties of the macroscopically entangled ground state wavefunction. Certain types of gauge transformations can result in the emergence of gauge fields that affect the behavior of low-energy excitations in the system. Such effects can therefore be used to distinguish between the different types of QSL states as they are realized in real systems. In this dissertation, I have presented evidence for the existence of a U(1) Dirac spin liquid state in Herbertsmithite. Specifically, I have observed a power-law contribution to the in-plane THz conductivity resulting from the effects of a gapless U(1) gauge field.

While Herbertsmithite is perhaps the best candidate for QSL physics, many other candidates exist, most notably the triangular organic salts $EtMe_3Sb[Pd(dmit)_2]_2$ and

κ-(BEDT-TTF)$_2$Cu$_2$(CN)$_3$. Power-law conductivity in these systems has also been theoretically predicted [40], with exponent differing from 2. Indeed, power-law behavior has been observed in the optical conductivity of κ-(BEDT-TTF)$_2$Cu$_2$(CN)$_3$ at mid-infrared frequencies [76], however, such frequencies are well above the exchange energy, and it is unclear how well the theoretical predictions hold in this region. Further THz spectroscopy studies on these systems are necessary to reach a conclusion about the properties of their spin liquid ground states.

Despite the work presented in this dissertation, the ground state in Herbertsmithite is still under debate. The presence of a significant fraction of copper defects in single-crystal samples serves to obscure the behavior of low-energy excitations, which may even fundamentally differ from the behavior of excitations in pure Herbertsmithite. It is therefore of significant interest to grow pure single crystals of Herbertsmithite, though this poses a significant materials science challenge. In the mean time, experiments that are insensitive to the copper defects serve as the best tools to study the low-energy behavior of QSL candidates. Recently, a site-specific NMR study found evidence for a spin gap in the intrinsic spin susceptibility of Herbertsmithite, with a zero-field gap value of $\sim$1 meV [118]. This gap value, however, contradicts the upper bound of 0.1 meV placed on the spin gap by neutron powder diffraction, as well as the existence of power-law conductivity as shown in this thesis. Further theoretical and experimental work is therefore required to reconcile these contradictions.

Appendix A

Optical Measurements on Herbertsmithite in the Near-Infrared Through the Ultraviolet

There has been very little work studying the optical properties of Herbertsmithite in the visible spectrum. While the relevant energy scales for spin liquid physics lie in the far-infrared, the Mott gap in Herbertsmithite is expected to be approximately 1 eV. Accurate measurements of this gap are critical in order to obtain accurate theoretical predictions about the THz conductivity in Herbertsmithite, as seen in chapter 4. Furthermore, it is important to know which wavelengths are absorbed by Herbertsmithite to enable future pump-probe measurements.

We have performed ultraviolet-visible spectrophotometry (UV-Vis) measurements on single-crystal Herbertsmithite at the MIT Center for Materials Science and Engineering user facilities. Broad-band incoherent light is produced by a halogen lamp. After selecting the wavelength using various optical filters, the light is split using a 50:50 beam splitter, with each half transmitting through either the sample or a reference. In this way, the transmission coefficient of Herbertsmithite can be measured at wavelengths between 200 nm and 1600 nm.

The measurements were performed at room temperature with the incident light polarization along the kagome planes. Figure A.1 shows the measured transmission

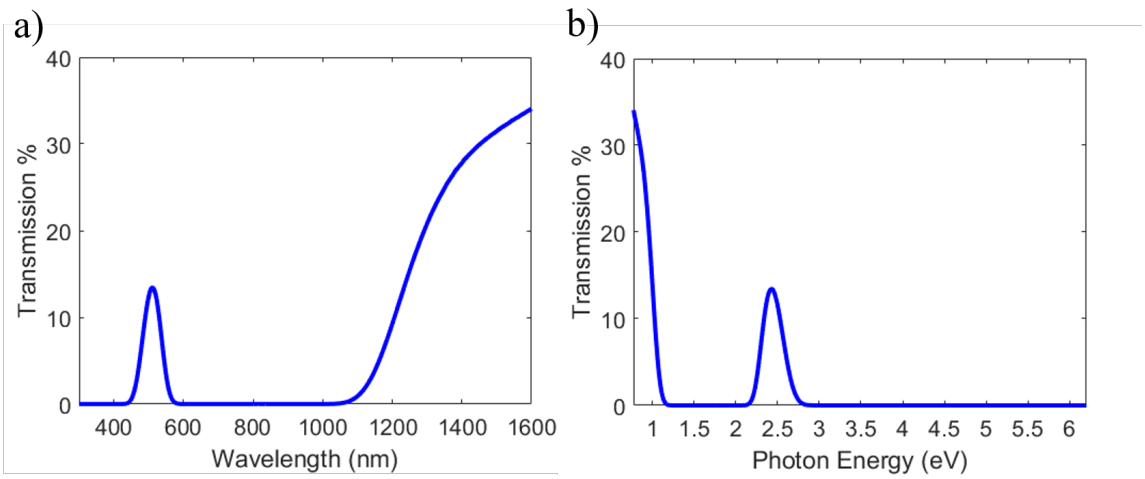

Figure A.1: The transmission coefficient of Herbertsmithite from the near-infrared through the ultraviolet versus wavelength (a) and photon energy (b). A clear optical gap is seen at 1 eV, while a window of transmission appears at around 500 nm, resulting in Herbertsmithite's distinct blue color.

coefficient versus wavelength and photon energy. At photon energies below 1 eV, a significant fraction of the incident light transmitted through the sample, indicating the existance of an optical gap of ~1 eV. A transmission window between 450 nm and 550 nm was also observed, consistent with Herbertsmithite's distinct blue color. Due to the thickness of the sample, very low conductivity was required to allow for the transmission of a measurable amount of light. Because of this, the transmission coefficient at all other measured wavelengths was 0%.

An optical gap of 1 eV was observed, however, the optical gap and Mott gap are not necessarily equal. In Mott insulators whose Hubbard bands are of a single orbital character, direct optical transitions across the Mott gap are forbidden. The optical gap edge in such systems is therefore a result of transitions from the lower Hubbard band into a separate band either between the two Hubbard bands or above the upper Hubbard band. If the Hubbard bands are of mixed orbital character, then direct transitions are allowed and the optical gap edge is a result of direct transitions from the lower Hubbard band to the upper Hubbard band. Since the antiferromagnetism in Herbertsmithite is the result of super-exchange through the Cu-O-Cu bonds, it is likely that the Hubbard bands are the result of hybridization between the oxygen 2p

and copper 3d bands. In this case, the optical and Mott gaps would be the same, making the Mott gap ~1 eV. Further detailed calculations of the band structure of Herbertsmithite are required to verify this claim.

As a final note, these measurements show that the color of Herbertsmithite is not a result of the Mott gap, as is sometimes claimed. While it may seem natural to assume that the blue color of Herbertsmithite is the result of a gap of ~2 eV, this is not the case. A ~0.5 eV wide window of transmission around 2.5 eV is responsible for the color.

Bibliography

[1] Charles Kittel. *Introduction to Solid State Physics*. Wiley, 8th edition, 2004.

[2] Neil W. Ashcroft and N. David Mermin. *Solid State Physics*. Brooks Cole, 1st edition, 1976.

[3] J. Bardeen, L. N. Cooper, and J. R. Schrieffer. Theory of superconductivity. *Phys. Rev.*, 108:1175–1204, Dec 1957.

[4] Ryusuke Matsunaga, Naoto Tsuji, Hiroyuki Fujita, Arata Sugioka, Kazumasa Makise, Yoshinori Uzawa, Hirotaka Terai, Zhen Wang, Hideo Aoki, and Ryo Shimano. Light-induced collective pseudospin precession resonating with higgs mode in a superconductor. *Science*, 345(6201):1145–1149, 2014.

[5] D. C. Tsui, H. L. Stormer, and A. C. Gossard. Two-dimensional magnetotransport in the extreme quantum limit. *Phys. Rev. Lett.*, 48:1559–1562, May 1982.

[6] R. B. Laughlin. Anomalous quantum hall effect: An incompressible quantum fluid with fractionally charged excitations. *Phys. Rev. Lett.*, 50:1395–1398, May 1983.

[7] J. Hubbard. Electron correlations in narrow energy bands. *Proceedings of the Royal Society of London A: Mathematical, Physical and Engineering Sciences*, 276(1365):238–257, 1963.

[8] N F Mott. Discussion of the papers by pohl, and by gurney and mott. *Proceedings of the Physical Society*, 49(4S):36, 1937.

[9] Joel S. Helton. *The Ground State of the Spin-$\frac{1}{2}$ Kagomé Lattice Antiferromagnet: Neutron Scattering Studies of the Zinc-Paratacamite Mineral Family*. PhD thesis, Massachusetts Institute of Technology, Cambridge, MA, 2009.

[10] A P Ramirez. Strongly geometrically frustrated magnets. *Annual Review of Materials Science*, 24(1):453–480, 1994.

[11] T. A. Kaplan. Classical spin-configuration stability in the presence of competing exchange forces. *Phys. Rev.*, 116:888–889, Nov 1959.

[12] Akio Yoshimori. A new type of antiferromagnetic structure in the rutile type crystal. *Journal of the Physical Society of Japan*, 14(6):807–821, 1959.

[13] J Villain. Two-level systems in a spin-glass model. i. general formalism and two-dimensional model. *Journal of Physics C: Solid State Physics*, 10(23):4793, 1977.

[14] J. A. Mydosh. *Spin Glasses: An Experimental Introduction*. CRC Press, 1993.

[15] Rainer Liebmann. *Statistical Mechanics of Periodic Frustrated Ising Systems*. Springer, 1986.

[16] G. H. Wannier. Antiferromagnetism. the triangular ising net. *Phys. Rev.*, 79:357–364, Jul 1950.

[17] Kenzi KanÃť and Shigeo Naya. Antiferromagnetism. the kagomÃĺ ising net. *Progress of Theoretical Physics*, 10(2):158–172, 1953.

[18] J. S. Helton, K. Matan, M. P. Shores, E. A. Nytko, B. M. Bartlett, Y. Yoshida, Y. Takano, A. Suslov, Y. Qiu, J.-H. Chung, D. G. Nocera, and Y. S. Lee. Spin dynamics of the spin-1/2 kagome lattice antiferromagnet zncu$_3$(OH)$_6$cl$_2$. *Phys. Rev. Lett.*, 98:107204, Mar 2007.

[19] David J. Griffiths. *Introduction to Quantum Mechanics*. Pearson Prentice Hall, 2nd edition, 2004.

[20] H. Bethe. Zur theorie der metalle. *Zeitschrift für Physik*, 71(3):205–226.

[21] L.D. Faddeev and L.A. Takhtajan. What is the spin of a spin wave? *Physics Letters A*, 85(6):375 – 377, 1981.

[22] F.D.M. Haldane. Continuum dynamics of the 1-d heisenberg antiferromagnet: Identification with the o(3) nonlinear sigma model. *Physics Letters A*, 93(9):464 – 468, 1983.

[23] N. D. Mermin and H. Wagner. Absence of ferromagnetism or antiferromagnetism in one- or two-dimensional isotropic heisenberg models. *Phys. Rev. Lett.*, 17:1133–1136, Nov 1966.

[24] J. B. Marston and C. Zeng. SpinâĂŘpeierls and spinâĂŘliquid phases of kagomÃĺ quantum antiferromagnets. *Journal of Applied Physics*, 69(8), 1991.

[25] M. B. Hastings. Dirac structure, rvb, and goldstone modes in the *kagomé* antiferromagnet. *Phys. Rev. B*, 63:014413, Dec 2000.

[26] Rajiv R. P. Singh and David A. Huse. Ground state of the spin-1/2 kagome-lattice heisenberg antiferromagnet. *Phys. Rev. B*, 76:180407, Nov 2007.

[27] Rajiv R. P. Singh and David A. Huse. Triplet and singlet excitations in the valence bond crystal phase of the kagome lattice heisenberg model. *Phys. Rev. B*, 77:144415, Apr 2008.

[28] P. Nikolic and T. Senthil. Physics of low-energy singlet states of the kagome lattice quantum heisenberg antiferromagnet. *Phys. Rev. B*, 68:214415, Dec 2003.

[29] K. Matan, T. Ono, Y. Fukumoto, T. J. Sato, J. Yamaura, M. Yano, K. Morita, and H. Tanaka. Pinwheel valence-bond solid and triplet excitations in the two-dimensional deformed kagome lattice. *Nature Physics*, 6:865–869, Sept 2010.

[30] Yasir Iqbal, Federico Becca, and Didier Poilblanc. Valence-bond crystal in the extended kagome spin-$\frac{1}{2}$ quantum heisenberg antiferromagnet: A variational monte carlo approach. *Phys. Rev. B*, 83:100404, Mar 2011.

[31] R. R. P. Singh. Valence bond glass phase in dilute kagome antiferromagnets. *Phys. Rev. Lett.*, 104:177203, Apr 2010.

[32] P.W. Anderson. Resonating valence bonds: A new kind of insulator? *Materials Research Bulletin*, 8(2):153 – 160, 1973.

[33] J. Richter. Resonating valence bond states in square lattice antiferromagnets with disorder and frustration. *Physics Letters A*, 140(1):81 – 83, 1989.

[34] Tian-Heng Han, Joel S. Helton, Shaoyan Chu, Daniel G. Nocera, Jose A. Rodrdiguez-Rivera, Collin Broholm, and Young S. Lee. Fractionalized excitations in the spin-liquid state of a kagome-lattice antiferromagnet. *Nature*, 492:406–410, Dec 2012.

[35] Bill Sutherland. Systems with resonating-valence-bond ground states: Correlations and excitations. *Phys. Rev. B*, 37:3786–3789, Mar 1988.

[36] Daniel S. Rokhsar and Steven A. Kivelson. Superconductivity and the quantum hard-core dimer gas. *Phys. Rev. Lett.*, 61:2376–2379, Nov 1988.

[37] N. Read and B. Chakraborty. Statistics of the excitations of the resonating-valence-bond state. *Phys. Rev. B*, 40:7133–7140, Oct 1989.

[38] X. G. Wen. Mean-field theory of spin-liquid states with finite energy gap and topological orders. *Phys. Rev. B*, 44:2664–2672, Aug 1991.

[39] Sung-Sik Lee and Patrick A. Lee. U(1) gauge theory of the hubbard model: Spin liquid states and possible application to κ-(BEDT-TTF)$_2$cu$_2$(CN)$_3$. *Phys. Rev. Lett.*, 95:036403, Jul 2005.

[40] Tai-Kai Ng and Patrick A. Lee. Power-law conductivity inside the mott gap: Application to κ-(BEDT-TTF)$_2$cu$_2$(CN)$_3$. *Phys. Rev. Lett.*, 99:156402, Oct 2007.

[41] Andrew C. Potter, T. Senthil, and Patrick A. Lee. Mechanisms for sub-gap optical conductivity in herbertsmithite. *Phys. Rev. B*, 87:245106, Jun 2013.

[42] T. Itou, A. Oyamada, S. Maegawa, M. Tamura, and R. Kato. Quantum spin liquid in the spin-12 triangular antiferromagnet $Etme_3Sb[Pd(dmit)_2]_2$. *Phys. Rev. B*, 77:104413, Mar 2008.

[43] Minoru Yamashita, Norihito Nakata, Yoshinori Senshu, Masaki Nagata, Hiroshi M. Yamamoto, Reizo Kato, Takasada Shibauchi, and Yuji Matsuda. Highly mobile gapless excitations in a two-dimensional candidate quantum spin liquid. *Science*, 328(5983):1246–1248, 2010.

[44] Satoshi Yamashita, Yasuhiro Nakazawa, Masaharu Oguni, Yugo Oshima, Hiroyuki Nojiri, Yasuhiro Shimizu, Kazuya Miyagawa, and Kazushi Kanoda. Thermodynamic properties of a spin-1/2 spin-liquid state in a κ-type organic salt. *Nature Physics*, 4:459–462, April 2008.

[45] F. L. Pratt, P. J. Baker, S. J. Blundell, T. Lancaster, S. Ohira-Kawamura, C. Baines, Y. Shimizu, K. Kanoda, I. Watanabe, and G. Saito. Magnetic and non-magnetic phases of a quantum spin liquid. *Nature*, 471:612–616, March 2011.

[46] I. Kézsmárki, Y. Shimizu, G. Mihály, Y. Tokura, K. Kanoda, and G. Saito. Depressed charge gap in the triangular-lattice mott insulator κ-$(ET)_2cu_2(CN)_3$. *Phys. Rev. B*, 74:201101, Nov 2006.

[47] Patrick A. Lee. An end to the drought of quantum spin liquids. *Science*, 321(5894):1306–1307, 2008.

[48] Matthew P. Shores, Emily A. Nytko, Bart M. Bartlett, , and Daniel G. Nocera*. A structurally perfect s = 1/2 kagomÃĺ antiferromagnet. *Journal of the American Chemical Society*, 127(39):13462–13463, 2005. PMID: 16190686.

[49] P. Mendels, F. Bert, M. A. de Vries, A. Olariu, A. Harrison, F. Duc, J. C. Trombe, J. S. Lord, A. Amato, and C. Baines. Quantum magnetism in the paratacamite family: Towards an ideal kagomé lattice. *Phys. Rev. Lett.*, 98:077204, Feb 2007.

[50] T. Imai, E. A. Nytko, B. M. Bartlett, M. P. Shores, and D. G. Nocera. ^{63}Cu, ^{35}Cl, and ^{1}H nmr in the $s = \frac{1}{2}$ kagome lattice $zncu_3(OH)_6cl_2$. *Phys. Rev. Lett.*, 100:077203, Feb 2008.

[51] A. Olariu, P. Mendels, F. Bert, F. Duc, J. C. Trombe, M. A. de Vries, and A. Harrison. ^{17}O nmr study of the intrinsic magnetic susceptibility and spin dynamics of the quantum kagome antiferromagnet $zncu_3(OH)_6cl_2$. *Phys. Rev. Lett.*, 100:087202, Feb 2008.

[52] Dirk Wulferding, Peter Lemmens, Patric Scheib, Jens Röder, Philippe Mendels, Shaoyan Chu, Tianheng Han, and Young S. Lee. Interplay of thermal and quantum spin fluctuations in the kagome lattice compound herbertsmithite. *Phys. Rev. B*, 82:144412, Oct 2010.

[53] Danna E. Freedman, Tianheng H. Han, Andrea Prodi, Peter MÃijller, Qing-Zhen Huang, Yu-Sheng Chen, Samuel M. Webb, Young S. Lee, Tyrel M. McQueen, and Daniel G. Nocera. Site specific x-ray anomalous dispersion of the geometrically frustrated kagome magnet, herbertsmithite, zncu3(oh)6cl2. *Journal of the American Chemical Society*, 132(45):16185–16190, 2010. PMID: 20964423.

[54] V. R. Shaginyan, A. Z. Msezane, and K. G. Popov. Thermodynamic properties of the kagome lattice in herbertsmithite. *Phys. Rev. B*, 84:060401, Aug 2011.

[55] M. A. de Vries, K. V. Kamenev, W. A. Kockelmann, J. Sanchez-Benitez, and A. Harrison. Magnetic ground state of an experimental $s = 1/2$ kagome antiferromagnet. *Phys. Rev. Lett.*, 100:157205, Apr 2008.

[56] F Bert, A Olariu, A Zorko, P Mendels, J C Trombe, F Duc, M A de Vries, A Harrison, A D Hillier, J Lord, A Amato, and C Baines. Frustrated magnetism in the quantum kagome herbertsmithite zncu 3 (oh) 6 cl 2 antiferromagnet. *Journal of Physics: Conference Series*, 145(1):012004, 2009.

[57] T. H. Han, J. S. Helton, S. Chu, A. Prodi, D. K. Singh, C. Mazzoli, P. Müller, D. G. Nocera, and Y. S. Lee. Synthesis and characterization of single crystals of the spin-$\frac{1}{2}$ kagome-lattice antiferromagnets $\mathrm{zn}_x\mathrm{cu}_{4-x}(\mathrm{oh})_6\mathrm{cl}_2$. *Phys. Rev. B*, 83:100402, Mar 2011.

[58] Sung-Sik Lee, Patrick A. Lee, and T. Senthil. Amperean pairing instability in the u(1) spin liquid state with fermi surface and application to κ-$(\mathrm{BEDT\text{-}TTF})_2\mathrm{cu}_2(\mathrm{CN})_3$. *Phys. Rev. Lett.*, 98:067006, Feb 2007.

[59] Simeng Yan, David A. Huse, and Steven R. White. Spin-liquid ground state of the s = 1/2 kagome heisenberg antiferromagnet. *Science*, 332(6034):1173–1176, 2011.

[60] Frederick Wooten. *Optical Properties of Solids*. Academic Press, New York, 1972.

[61] M. Dressel and G. Grüner. *Electrodynamics of Solids: Optical Properties of Electrions in Matter*. Cambridge University Press, Cambridge, 2002.

[62] G. Grüner. *Millimeter and Submillimeter Wave Spectroscopy of Solids*. Springer, 1998.

[63] Y. S. Lee. *Principles of Terahertz Science and Technology*. Springer, 2009.

[64] Y. Lubashevsky, LiDong Pan, T. Kirzhner, G. Koren, and N. P. Armitage. Optical birefringence and dichroism of cuprate superconductors in the thz regime. *Phys. Rev. Lett.*, 112:147001, Apr 2014.

[65] D. Fausti, R. I. Tobey, N. Dean, S. Kaiser, A. Dienst, M. C. Hoffmann, S. Pyon, T. Takayama, H. Takagi, and A. Cavalleri. Light-induced superconductivity in a stripe-ordered cuprate. *Science*, 331(6014):189–191, 2011.

[66] Beth Parks, S. Spielman, J. Orenstein, D. T. Nemeth, Frank Ludwig, John Clarke, Paul Merchant, and D. J. Lew. Phase-sensitive measurements of vortex dynamics in the terahertz domain. *Phys. Rev. Lett.*, 74:3265–3268, Apr 1995.

[67] Ryusuke Matsunaga, Yuki I. Hamada, Kazumasa Makise, Yoshinori Uzawa, Hirotaka Terai, Zhen Wang, and Ryo Shimano. Higgs amplitude mode in the bcs superconductors $\mathrm{nb}_{1\text{-}x}\mathrm{ti}_x\mathbf{N}$ induced by terahertz pulse excitation. *Phys. Rev. Lett.*, 111:057002, Jul 2013.

[68] Matthew C. Beard, Gordon M. Turner, and Charles A. Schmuttenmaer. Transient photoconductivity in gaas as measured by time-resolved terahertz spectroscopy. *Phys. Rev. B*, 62:15764–15777, Dec 2000.

[69] M. Walther, D. G. Cooke, C. Sherstan, M. Hajar, M. R. Freeman, and F. A. Hegmann. Terahertz conductivity of thin gold films at the metal-insulator percolation transition. *Phys. Rev. B*, 76:125408, Sep 2007.

[70] Jason Horng, Chi-Fan Chen, Baisong Geng, Caglar Girit, Yuanbo Zhang, Zhao Hao, Hans A. Bechtel, Michael Martin, Alex Zettl, Michael F. Crommie, Y. Ron Shen, and Feng Wang. Drude conductivity of dirac fermions in graphene. *Phys. Rev. B*, 83:165113, Apr 2011.

[71] Ronald Ulbricht, Euan Hendry, Jie Shan, Tony F. Heinz, and Mischa Bonn. Carrier dynamics in semiconductors studied with time-resolved terahertz spectroscopy. *Rev. Mod. Phys.*, 83:543–586, Jun 2011.

[72] Y. H. Wang, H. Steinberg, P. Jarillo-Herrero, and N. Gedik. Observation of floquet-bloch states on the surface of a topological insulator. *Science*, 342(6157):453–457, 2013.

[73] Y. L. Chen, J.-H. Chu, J. G. Analytis, Z. K. Liu, K. Igarashi, H.-H. Kuo, X. L. Qi, S. K. Mo, R. G. Moore, D. H. Lu, M. Hashimoto, T. Sasagawa, S. C. Zhang, I. R. Fisher, Z. Hussain, and Z. X. Shen. Massive dirac fermion on the surface of a magnetically doped topological insulator. *Science*, 329(5992):659–662, 2010.

[74] Hai-Zhou Lu, Wen-Yu Shan, Wang Yao, Qian Niu, and Shun-Qing Shen. Massive dirac fermions and spin physics in an ultrathin film of topological insulator. *Phys. Rev. B*, 81:115407, Mar 2010.

[75] D. V. Pilon, C. H. Lui, T. H. Han, D. Shrekenhamer, A. J. Frenzel, W. J. Padilla, Y. S. Lee, and N. Gedik. Spin-induced optical conductivity in the spin-liquid candidate herbertsmithite. *Phys. Rev. Lett.*, 111:127401, Sep 2013.

[76] Sebastian Elsässer, Dan Wu, Martin Dressel, and John A. Schlueter. Power-law dependence of the optical conductivity observed in the quantum spin-liquid compound κ-(bedt-ttf)$_2$cu$_2$(cn)$_3$. *Phys. Rev. B*, 86:155150, Oct 2012.

[77] D. B. Tanner. Use of x-ray scattering functions in kramers-kronig analysis of reflectance. *Phys. Rev. B*, 91:035123, Jan 2015.

[78] David J. Griffiths. *Introduction to Electrodynamics*. Prentice Hall, 3rd edition, 1999.

[79] J. D. Jackson. *Classical Electrodynamics*. John Wiley and Sons, 3rd edition, 1999.

[80] Y. R. Shen. *The Principles of Nonlinear Optics*. Wiley-Interscience, 2002.

[81] Alex J. Frenzel. *Terahertz Electrodynamics of Dirac Fermions in Graphene*. PhD thesis, Harvard University, Cambridge, MA, 2015.

[82] Robert W. Boyd. *Nonlinear Optics*. Academic Press, 3rd edition, 2008.

[83] Paul C. M. Planken, Han-Kwang Nienhuys, Huib J. Bakker, and Tom Wenckebach. Measurement and calculation of the orientation dependence of terahertz pulse detection in znte. *J. Opt. Soc. Am. B*, 18(3):313–317, Mar 2001.

[84] Grant R. Fowles. *Introduction to Modern Optics*. Dover Publications, 2nd edition, 1989.

[85] L. Duvillaret, F. Garet, and J. L. Coutaz. A reliable method for extraction of material parameters in terahertz time-domain spectroscopy. *IEEE Journal of Selected Topics in Quantum Electronics*, 2(3):739–746, Sep 1996.

[86] Lionel Duvillaret, Frédéric Garet, and Jean-Louis Coutaz. Highly precise determination of optical constants and sample thickness in terahertz time-domain spectroscopy. *Appl. Opt.*, 38(2):409–415, Jan 1999.

[87] Yihong Yang, Alisha Shutler, and D. Grischkowsky. Measurement of the transmission of the atmosphere from 0.2 to 2 thz. *Opt. Express*, 19(9):8830–8838, Apr 2011.

[88] Christopher A. Werley, Stephanie M. Teo, and Keith A. Nelson. Pulsed laser noise analysis and pump-probe signal detection with a data acquisition card. *Review of Scientific Instruments*, 82(12), 2011.

[89] Bengt Nordén, Alison Rodger, and Tim Dafforn. *Linear Dichroism and Circular Dichroism: A Textbook on Polarized-Light Spectroscopy*. Royal Society of Chemistry, 1st edition, 2010.

[90] X. Wang, D. J. Hilton, J. L. Reno, D. M. Mittleman, and J. Kono. Direct measurement of cyclotron coherence times of high-mobility two-dimensional electron gases. *Opt. Express*, 18(12):12354–12361, Jun 2010.

[91] Xiangfeng Wang, David J. Hilton, Lei Ren, Daniel M. Mittleman, Junichiro Kono, and John L. Reno. Terahertz time-domain magnetospectroscopy of a high-mobility two-dimensional electron gas. *Opt. Lett.*, 32(13):1845–1847, Jul 2007.

[92] Qi Zhang, Takashi Arikawa, Eiji Kato, John L. Reno, Wei Pan, John D. Watson, Michael J. Manfra, Michael A. Zudov, Mikhail Tokman, Maria Erukhimova, Alexey Belyanin, and Junichiro Kono. Superradiant decay of cyclotron resonance of two-dimensional electron gases. *Phys. Rev. Lett.*, 113:047601, Jul 2014.

[93] D. M. Mittleman, J. Cunningham, M. C. Nuss, and M. Geva. Noncontact semiconductor wafer characterization with the terahertz hall effect. *Applied Physics Letters*, 71(1), 1997.

[94] Y. Ikebe, T. Morimoto, R. Masutomi, T. Okamoto, H. Aoki, and R. Shimano. Optical hall effect in the integer quantum hall regime. *Phys. Rev. Lett.*, 104:256802, Jun 2010.

[95] A. M. Shuvaev, G. V. Astakhov, G. Tkachov, C. Brüne, H. Buhmann, L. W. Molenkamp, and A. Pimenov. Terahertz quantum hall effect of dirac fermions in a topological insulator. *Phys. Rev. B*, 87:121104, Mar 2013.

[96] Takahiro Morimoto, Yasuhiro Hatsugai, and Hideo Aoki. Optical hall conductivity in ordinary and graphene quantum hall systems. *Phys. Rev. Lett.*, 103:116803, Sep 2009.

[97] Cui-Zu Change, Weiwei Zhao, Duk Y. Kim, Haijun Zhang, Badih A. Assaf, Don Heiman, Shou-Cheng Zhang, Chaoxing Liu, Moses H. W. Chan, and Jagadeesh S. Moodera. High-precision realization of robust quantum anomalous hall state in a hard ferromagnetic topological insulator. *Nature Materials*, 14:473–477, March 2015.

[98] Rui Yu, Wei Zhang, Hai-Jun Zhang, Shou-Cheng Zhang, Xi Dai, and Zhong Fang. Quantized anomalous hall effect in magnetic topological insulators. *Science*, 329(5987):61–64, 2010.

[99] Cui-Zu Chang, Jinsong Zhang, Xiao Feng, Jie Shen, Zuocheng Zhang, Minghua Guo, Kang Li, Yunbo Ou, Pang Wei, Li-Li Wang, Zhong-Qing Ji, Yang Feng, Shuaihua Ji, Xi Chen, Jinfeng Jia, Xi Dai, Zhong Fang, Shou-Cheng Zhang, Ke He, Yayu Wang, Li Lu, Xu-Cun Ma, and Qi-Kun Xue. Experimental observation of the quantum anomalous hall effect in a magnetic topological insulator. *Science*, 340(6129):167–170, 2013.

[100] Gang Xu, Hongming Weng, Zhijun Wang, Xi Dai, and Zhong Fang. Chern semimetal and the quantized anomalous hall effect in $hgcr_2se_4$. *Phys. Rev. Lett.*, 107:186806, Oct 2011.

[101] A. A. Zyuzin and A. A. Burkov. Topological response in weyl semimetals and the chiral anomaly. *Phys. Rev. B*, 86:115133, Sep 2012.

[102] Xiaochun Huang, Lingxiao Zhao, Yujia Long, Peipei Wang, Dong Chen, Zhanhai Yang, Hui Liang, Mianqi Xue, Hongming Weng, Zhong Fang, Xi Dai, and Genfu Chen. Observation of the chiral-anomaly-induced negative magnetoresistance in 3d weyl semimetal taas. *Phys. Rev. X*, 5:031023, Aug 2015.

[103] G. R. Harp, D. Weller, T. A. Rabedeau, R. F. C. Farrow, and M. F. Toney. Magneto-optical kerr spectroscopy of a new chemically ordered alloy: co_3pt. *Phys. Rev. Lett.*, 71:2493–2496, Oct 1993.

[104] Satoshi Tomita, Takeshi Kato, Shigeru Tsunashima, Satoshi Iwata, Minoru Fujii, and Shinji Hayashi. Magneto-optical kerr effects of yttrium-iron garnet thin films incorporating gold nanoparticles. *Phys. Rev. Lett.*, 96:167402, Apr 2006.

[105] C. M. Morris, R. Valdés Aguilar, A. V. Stier, and N. P. Armitage. Polarization modulation time-domain terahertz polarimetry. *Opt. Express*, 20(11):12303–12317, May 2012.

[106] Ching-Kit Chan, Patrick A. Lee, Kenneth S. Burch, Jung Hoon Han, and Ying Ran. When chiral photons meet chiral fermions: Photoinduced anomalous hall effects in weyl semimetals. *Phys. Rev. Lett.*, 116:026805, Jan 2016.

[107] Zhenghao Gu, H. A. Fertig, Daniel P. Arovas, and Assa Auerbach. Floquet spectrum and transport through an irradiated graphene ribbon. *Phys. Rev. Lett.*, 107:216601, Nov 2011.

[108] P. M. Perez-Piskunow, Gonzalo Usaj, C. A. Balseiro, and L. E. F. Foa Torres. Floquet chiral edge states in graphene. *Phys. Rev. B*, 89:121401, Mar 2014.

[109] Hossein Dehghani, Takashi Oka, and Aditi Mitra. Out-of-equilibrium electrons and the hall conductance of a floquet topological insulator. *Phys. Rev. B*, 91:155422, Apr 2015.

[110] Takuya Kitagawa, Takashi Oka, Arne Brataas, Liang Fu, and Eugene Demler. Transport properties of nonequilibrium systems under the application of light: Photoinduced quantum hall insulators without landau levels. *Phys. Rev. B*, 84:235108, Dec 2011.

[111] P. W. Anderson. The resonating valence bond state in la2cuo4 and superconductivity. *Science*, 235(4793):1196–1198, 1987.

[112] Patrick A. Lee, Naoto Nagaosa, and Xiao-Gang Wen. Doping a mott insulator: Physics of high-temperature superconductivity. *Rev. Mod. Phys.*, 78:17–85, Jan 2006.

[113] Ying Ran, Michael Hermele, Patrick A. Lee, and Xiao-Gang Wen. Projected-wave-function study of the spin-1/2 heisenberg model on the kagomé lattice. *Phys. Rev. Lett.*, 98:117205, Mar 2007.

[114] Leon Balents. Spin liquids in frustrated magnets. *Nature*, 464:199–208, March 2010.

[115] Max Born and Emil Wolf. *Principles of Optics*. Cambridge University Press, 7th edition, 1999.

[116] M. Jeong, F. Bert, P. Mendels, F. Duc, J. C. Trombe, M. A. de Vries, and A. Harrison. Field-induced freezing of a quantum spin liquid on the kagome lattice. *Phys. Rev. Lett.*, 107:237201, Nov 2011.

[117] Ying Ran, Wing-Ho Ko, Patrick A. Lee, and Xiao-Gang Wen. Spontaneous spin ordering of a dirac spin liquid in a magnetic field. *Phys. Rev. Lett.*, 102:047205, Jan 2009.

[118] Mingxuan Fu, Takashi Imai, Tian-Heng Han, and Young S. Lee. Evidence for a gapped spin-liquid ground state in a kagome heisenberg antiferromagnet. *Science*, 350(6261):655–658, 2015.